THE DYNAMICS OF THE MIDLATITUDE MESOSPHERE AND LOWER THERMOSPHERE

A Dissertation

Presented to the Faculty of the Graduate School

of Cornell University

in Partial Fulfillment of the Requirements for the Degree of

Doctor of Philosophy

by

Eliana Nossa

January 2017

THE DYNAMICS OF THE MIDLATITUDE MESOSPHERE AND LOWER THERMOSPHERE

Eliana Nossa, Ph.D.

Cornell University 2017

This is a study of the causes of disrupted ionospheric E layers at middle latitudes. The irregularities described here are organized accordingly to the Richardson (R_i) number, starting from negative, to less than one quarter, to larger than one. Since R_i is a function of the neutral winds, a methodology to estimate the mesosphere and lower thermosphere (MLT) neutral winds between 95 - 130 km altitude is applied for data collected during the incoherent scatter radar (ISR) coordinated "World Day" campaigns at Arecibo. The methodology reflects the physical coupling between the neutral atmosphere and the ionosphere at E-layer heights. The method is compared with previous attempts to calculate the neutral winds at the Arecibo Observatory. The methodology is validated using error analysis and considering possible data contamination due to gravity waves. Temperature profiles, electric fields, and ion composition are also estimated. Using those parameters, the subsequent sections of the dissertation study irregularities observed in the neutral atmosphere in the MLT region during the day. Analysis of temperature variations following convective instability events shows that most of the days have broad unstable regions, where the condition needed to develop this kind of instability is present (buoyancy frequency $N^2 < 0$). During these days, disturbed temperature profiles are observed. Dynamic instability studies show zones with $0 < R_i < 1/4$ where wavy ion layers are observed during the day. Also, a study of planetary-wave activ-

ity is performed to investigate the effects of the imbalance between the Coriolis and the Lorentz forces and manifested in the change of the rotational direction of the neutral wind. These changes are observed in areas where the conditions that shape cyclones in the atmosphere due to baroclinic instability are present ($Ro < 1$ and $R_i > 1$), where Ro is the Rossby number. Finally, studies of nocturnal quasi-periodic (QP) echoes are presented to investigate their dynamic instability origin. The irregularities produced different disruptions in the E layer. Convective instability events can create broken layers. Dynamic instabilities generate billow behavior and bifurcation that can also lead to broken layers. Planetary-wave effects can explain the rotational neutral winds and changes in their rotational direction.

BIOGRAPHICAL SKETCH

The author obtained her B.E. in Electrical Engineering at the Universidad de Los Andes in Colombia. She was an entrepreneur, lecturer, and manager before moving to the US. In 2004, she joined the Astronomy Department at Cornell University, working on projects related to the Atacama radio telescope and the Arecibo Observatory. There, as part of the degree requirements for her Master's in Engineering, she designed a prototype of a focal phased array for the Arecibo radio telescope under the direction of Dr. German Cortes. In the summer of 2007, she joined the Space Plasma Group as a graduate student under the direction of Dr. David Hysell in the Earth and Atmospheric Sciences Department at Cornell University. During her doctorate studies, she participated in various research projects involving coherent and incoherent scatter radars to perform research in areas related to ionospheric modification at high latitudes and mesospheric and lower thermosphere irregularities at mid-latitudes.

She was honored with the Outstanding Student Paper award from AGU in 2011. Also, she was invited, as a young scientist and only student, to the International Space Science Institute (ISSI) Workshop: Coupling between Earth's atmosphere and its plasma environment in Bern, Switzerland, in September 2010. She has served as a reviewer for the Journal of Geophysical Research - Space Sciences and the Journal of Atmospheric and Solar - Terrestrial Physics. She was a member of the Science Advisory Committee on the 13th International Symposium on Equatorial Aeronomy in Perú in 2012. While at Cornell, she was the president of the Colombian Student Association, CUCSA. The author also balances her profession being a mother of a 3-year-old boy.

Dedicated to:

Solomon,

Zilita and Viso,

&

Juan C.

ACKNOWLEDGEMENTS

I wish to express my sincere gratitude to Prof. David Hysell, Chair of my special committee, for his guidance, teachings, and continuous support. I admire his passion and commitment to the advance of ionospheric research, his love to detail and his discipline.

I am also grateful to Prof. Donald Campbell, who opened the doors for me in the Astronomy Department and the Arecibo Observatory when I joined Cornell. I thank Prof. Peter Gierasch for his profound insights about atmospheric sciences, and Prof. Michael Kelley for his teachings and encouragement.

My appreciation goes to Prof. Peter Diamessis for the frequent consultations. I am deeply indebted to Prof. Miguel Larsen from Clemson University for the invaluable suggestions and because his theoretical foundations are a framework of my research. Also, I would like to thank Prof. Christos Haldoupis from the University of Crete for the encouragement and suggestions.

I value the hospitality of people at Arecibo Observatory and HAARP. I appreciate the work made by Dr. Michael Sulzer, Dr. Nestor Aponte, and Dr. Sixto Gonzalez that provide me the ISR data. I thank the effort made by Dr. Shikha Raizada and Dr. Jonathan Friedman to obtain the lidar data. I am indebted to Dr. Raizada for her sincere hospitality and teachings about lidars and optics systems. I thank Mike McCarry for helping me to perform the experiments at HAARP. I am also thankful with Prof. William Bristow, Prof. Robert Moore, Prof. Jade Morton and their research groups for the long and inspirational conversations during HAARP campaigns.

I thank the Arecibo Observatory for providing me the data for this dissertation. The Arecibo Observatory was operated by Cornell University until 2011 and then by a consortium between SRI International, the Universities Space Research Association, and Universidad Metropolitana de Puerto Rico, under cooperative agreements with the National Science Foundation.

I would like to thank Dr. German Cortes and his wife, Pilar, for their friendship, encouragement and motivation that made me pursue the doctoral degree. I also thank Prof. Muawia Barazangi and his wife, Nimat, for their friendship and mentorship. I also thank the women in ionospheric sciences and the ECE woman faculty group for their support, especially Prof. Michael Lipson. Her words were my light during difficult moments.

I am also grateful for having the opportunity of sharing my time at Cornell with inspirational class- and group-mates. I express my gratitude to Savannah Williams, Scott Coldren, Amy Colvin, and Judy Starr at Earth and Atmospheric Sciences and the Electrical and Computer Engineering departments. They helped me navigate with all the practical aspects at Cornell.

I do not have words to thank my husband, my son, my parents and siblings for all the support during my grad school years. They are my motivation for everything I do.

Finally and foremost, I thank God who made everything possible.

TABLE OF CONTENTS

1

INTRODUCTION

"All my life through, the new sights of Nature made me rejoice like a child"

– Marie Curie

Unexplained characteristics in the mesosphere and lower thermosphere (MLT) region motivate this dissertation. At MLT-region heights, neutral, ion and electron species coexist and interact under multiple forces. Charged particles are usually organized in layers but sometimes the layers suddenly break, creating patches of ions or altering the ion density. The movements of the neutrals and ions are perhaps the most critical parameters needed to study these irregularities. This introduction is a brief overview of the neutral and charged atmospheres at MLT region heights to contextualize the nature of the irregularities.

The objective of this dissertation is to evaluate which kind of instabilities are at play in the MLT region and assess if they could be the cause of these disruptions. A diagnosis of the region is performed using observations from the Arecibo Observatory combined with a methodology introduced by *Hysell et al.* [2014] to estimate neutral winds and electric fields. The observations correspond to campaigns of up to 3 continuous days. This dissertation performs the analysis for daytime irregularities. Daytime neutral winds for the whole MLT region are difficult to obtain with other instruments due to technical restrictions, making these data unique.

1.1 The neutral and charged atmosphere

The atmosphere surrounding the earth is subdivided into five layers: the troposphere, the stratosphere, the mesosphere, the thermosphere and the exosphere. This classification is based on the variations of the Earth's vertical temperature profile shown in Figure 1.1. The thermosphere is the hottest atmospheric layer, but the neutral density at thermospheric altitudes is thin.

Solar radiation penetrates the atmosphere. The solar photons ionize the neutral atmosphere and create ions and electrons in the same number, preserving charge neutrality ($n_e \cong n_i$). Radiation at visible and infrared wavelengths reaches the troposphere and the solid earth. However, X-rays and ultraviolet wavelengths are absorbed by the upper layers of the atmosphere. Waves with X-ray wavelengths penetrate the upper thermosphere, reaching stratospheric heights. For heights above the mesopause, the temperature increases due to the absorption of solar UV radiation. This kind of radiation also produces ions (and electrons) at the thermosphere heights, forming the ionosphere. These charged particles are conductive and can be affected by the Earth's magnetic field.

Different forms of solar radiation reach the ionosphere. The ionosphere is subdivided into three regions, in order from low to high altitudes: D, E, and F. Far-ultraviolet radiation (with wavelength between 122-200 nm) reaches upper *E*-region heights whereas extreme-ultraviolet wavelengths (10-121 nm) reach just *F*-region heights. Mid-UV radiation (wavelength between 200-300 nm) penetrates the ionosphere, decreasing until the ionization stops at heights less than $\sim$ 90 km, affecting the *E* and *D* regions. The neutral density decreases with altitude, so there are fewer atoms to be ionized at higher altitudes. The balance

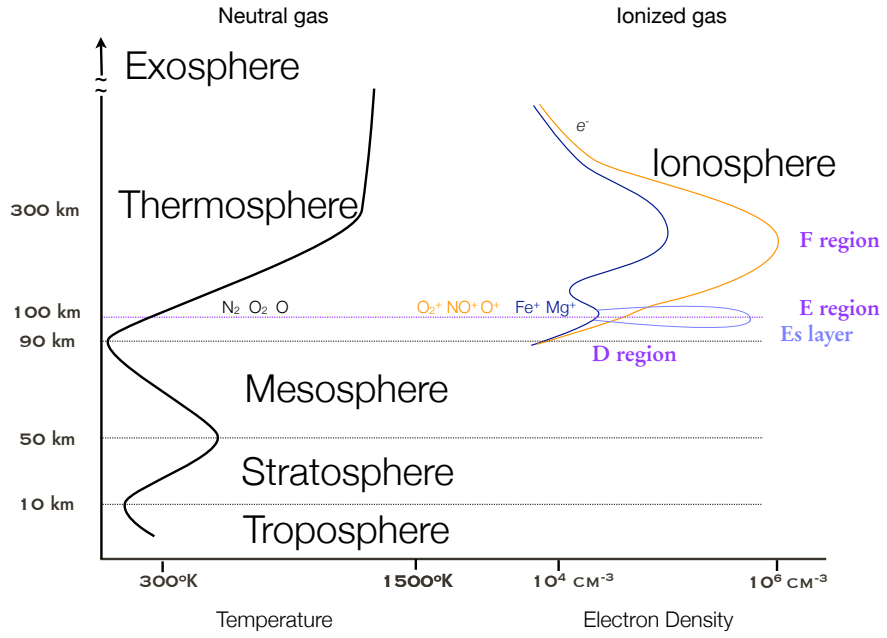

Figure 1.1: Earth's atmosphere. The left temperature profile corresponds to the atmospheric layers. The Mesopause is the place where the temperature reaches the minimum value. From there and up, the layer is known as thermosphere, where the temperature increases at the same time that the neutral density decreases. At these altitudes, the temperature is variable and is highly dependable of the solar activity. However, temperatures above 1000 K are frequently observed. At the same heights, the neutral particles are ionized by the solar radiation and ions and electrons are formed creating the ionosphere (orange) profile of the right. At night (blue profile), the solar ionization is absent but long-lived ions deployed by meteors are present. Occasionally at night, the electron density rapidly increases creating what is known as sporadic E (Es) layer. (See text for description).

of these two actions produces an ionization peak at around 110 km. The region around this ionization peak is known as the *E* region.

1.2 The *E* layer

Marconi established transatlantic radio communications between England and Newfoundland in 1901. It was possible because the transmitted signal was reflected in the ionosphere. Sir Edward V. Appleton in his Nobel Lecture on December 12, 1947, related how he discovered the "electrically" conductive layer, previously suggested by Balfour Stewart in 1882 and formally explained by Kennelly and Heaviside in 1902. He transmitted radio signals and reflected them using the ionosphere at around 100 km. He called this region the *E* layer. He also discovered and named another two layers: the *F* layer (a higher ionized layer at around 230 km), and the *D* layer (a lower and more weakly ionized layer). Since then, radio amateurs have continued to use the *E* layer to establish long-distance radio-wave communications.

The *E*-region is characterized by high temperatures and electron densities, which are in the range that fulfills the criteria for plasma fluids as follows:

$$\begin{aligned} \lambda_D = &\quad 69(T/n)^{1/2} &&\ll L \\ N_D = &\quad n\tfrac{4}{3}\pi\lambda_D^3 &&\gg 1 \\ \Omega\tau = &\quad e\mathbf{B}\tau/m &&> 1 \end{aligned} \tag{1.1}$$

where the *E* region conditions of temperature $T \approx 300$ K and plasma density $n \approx 10^{11}$ m^{-3} imply a Debye length $\lambda_D \approx 3 \times 10^{-3}$ m, which is smaller than the dimensions of the region L of approximately a few kilometers. The number of particles in the Debye sphere is $N_D \approx 2.2 \times 10^4$. The gyro-frequency, Ω, is of the order of few MHz for the electrons at *E*-layer heights. The mean

free time between collisions with neutral atoms, τ, for electrons is about 10^{-4} seconds. These conditions, unlike neutral gasses, make the ionosphere a conductive plasma medium that can be affected by the Earth's magnetic field.

The ionosphere is regulated by plasma physics. However, it coexists with the neutral thermosphere. The daytime E region composition is dominated by neutral (N_2, O_2 and O), molecular ions (O_2^+, NO^+), atomic oxygen (O^+), and electrons. Atomic oxygen is only present above 100 km because it is produced by photodissociation of O_2 due to UV radiation. Atomic oxygen is the main source of ions. Also, meteor ablation deposits long-lived heavy atomic ions (Fe^+ and Mg^+).

The ion dynamics are dominated by collisions with neutrals at heights below 90 km since the collisions deviate the charged particles from the original trajectory around the magnetic field. At higher altitudes (in the collisionless regime), the ions become magnetized and spiral around the Earth's magnetic field lines, and the medium become highly conductive in the direction parallel to the Earth's magnetic field. This feature allows mapping of electric features along the magnetic field lines. At E region heights, conductivities perpendicular to the Earth's magnetic field are also significant and allow current closure between the E and F layers. The factors dependent on the ratio of the gyro- to collision-frequency determine the transition between these domains. The interactions between the charged and the neutral species are essential for understanding the phenomena in the MLT region.

1.3 Sporadic E_s layers

From the earliest observations, the irregular nature of the nocturnal E layer has intrigued many scientists because radio waves are reflected when dense ion patches are present in the E region between $\approx 95 - 130$ km. When this happens, the layer is known as a sporadic E layer (or E_s).

The first scientific observations of the E_s layer seem to have been performed in December 1941, in the Chalmers Ionospheric Observatory in Göteborg, Sweden (*Rydbeck* [1942]). The term sporadic E_s layer has been used widely. However, it should only be used to refer to layers with enhanced ion density. Ionosondes measure the critical frequency which is related to density ($f_{oE} \approx 9 \times 10^3 \sqrt{n_e}$ Hz where n_e is the number of electrons cm^{-3}). Typical nighttime electron densities in the E layer over Arecibo vary but are near to 3×10^4 cm^{-3}. Occasionally, measurements of electron density enhancements reach values similar to the peak F-region daytime ionization ($\approx 10^6$ cm^{-3}).

1.4 Ion layer formation at E region heights

The Arecibo Observatory has been used to measure the ionosphere for more than 50 years. Figure 1.2 shows a power profile obtained with the incoherent scatter radar (ISR). Thin ion descending layers are observed during the day and sometimes at night, with densities sometimes larger than that produced by daytime ionization. The correct alignment of neutral winds generates a convergence of long-lived ions (like metallic ions) in the presence of the Earth's magnetic field to form thin ion layers. This theory was introduced by *Whitehead*

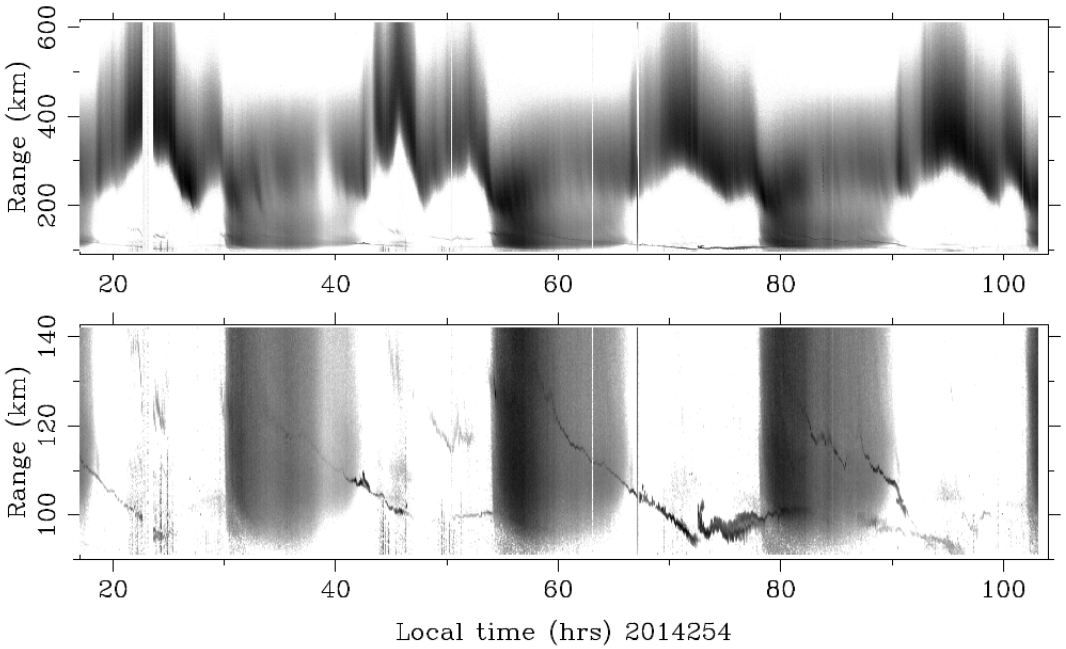

Figure 1.2: Arecibo ISR power profile between $100 - 600$ km altitude for three and a half days starting at sunset on September 11, 2014. Here, the grey scale is proportional to the ion density. The continuous measurements show diurnal ionization as well as diurnal and nocturnal ion layers. Diurnal background ionization is stronger and it is depicted in the dark regions between 30-42 h, 54-66 h and 78-90 h. The second panel is a close up of the E region at altitudes between $95 - 140$ km. For the third night after 70h (LT), the presence of an E_s is seen with some kid of rolls or billow activity.

[1961] and is known as the wind-shear mechanism. The ion descending layers follow the same pattern as the diurnal and semidiurnal tides in the neutral atmosphere as shown by *Kirkwood and Nilsson* [2000] (Figure 6A). The Figure shows a simulation of the behavior of the layer using ion drift equations depending on neutral winds, electrodynamics, and ion production and loss factors for the high-latitude E-region. For that case, a zonal semidiurnal tide with an amplitude of 60 m/s and Fe^+ composition was assumed. The ion production and loss, electric fields and vertical winds are neglected. Also, *Haldoupis* [2011b]

was able to match semidiurnal S(2,6) and a diurnal S(1,1) modes with descending upper and lower ion layers observed by Arecibo. Tidal variability has also been observed (*Li et al.* [2009]). Some of this variability is attributed to gravity waves that may become unstable.

1.5 *E* region irregularities

One of the central questions in the midlatitude *E*-layer research has to do with the cause of patchiness and of the sporadic behavior. Considerable research has been done to explain *E*-layer ionospheric disturbances (see reviews by *Layzer* [1962], *Whitehead* [1972], *Whitehead* [1989], *Mathews* [1998], *Haldoupis* [2011a]). Wind shear and tidal interaction are the causes most frequently ascribed to the general characteristics of *E*-layer irregularities. However, other processes present at those altitudes are not so well understood. For example, Arecibo measurements show unexplained changes in the temperature distribution in the region. Also, other processes should be at play since neutral winds are usually underestimated when calculated using models based only on wind-shear and tidal mechanisms (*Larsen and Fesen* [2009]).

Another example and perhaps the most studied form of midlatitude *E*-layer irregularity are quasi-periodic (QP) echoes. These echoes were detected first by *Riggin et al.* [1986] and *Yamamoto et al.* [1991] using coherent scatter radars when E_s layers were present. The echoes are produced by small-scale field-aligned plasma density irregularities, which generate currents in the sporadic E_s layer. The coherent scatter Doppler shifts for the sporadic E_s layer are dependent on the polarization electric fields, which are also controlled by the conductivity

and background electric field. The structured irregularities are of the order of meter scale and are detected by 30-50 MHz radars looking perpendicular to the magnetic field. Figure 1.3 shows QP irregularities passing over Arecibo as observed with a coherent scatter radar deployed in St. Croix, an island in the Caribbean close to Puerto Rico. Theories that try to explain this phenomena vary from gravity waves (*Woodman et al.* [1991]) to interaction between the *E* and *F* layers (*Cosgrove and Tsunoda* [2001] and references therein). However, multiple studies and observations support the theory that these echoes are the product of large neutral wind shears that produce Kevin-Helmholtz rolls that break up the ion layers, forming patches of ionization distributed at *E*-layer heights (see *Larsen* [2000a], *Bernhardt* [2002], *Hysell et al.* [2004], *Bernhardt et al.* [2006], *Larsen et al.* [2007], *Hysell et al.* [2009]).

1.6 Neutral winds

Neutral winds are needed to study irregularities in the *E* layer. They and the associated neutral turbulence are observed remotely. A comprehensive list of techniques used to observed the neutral winds is found in section 2.1. Researchers at Arecibo have been trying to determine the neutral winds, but technical limitations have undermined their efforts. Just recently, *Hysell et al.* [2014] used different transmitting modes to estimate the neutral winds for the mesosphere and lower thermosphere (MLT) based on the ISR ion drifts measurements. This new methodology uses the full capabilities of the Arecibo Observatory, including the Gregorian upgrade from 1997. These newly obtained winds open the possibility to study neutral instabilities.

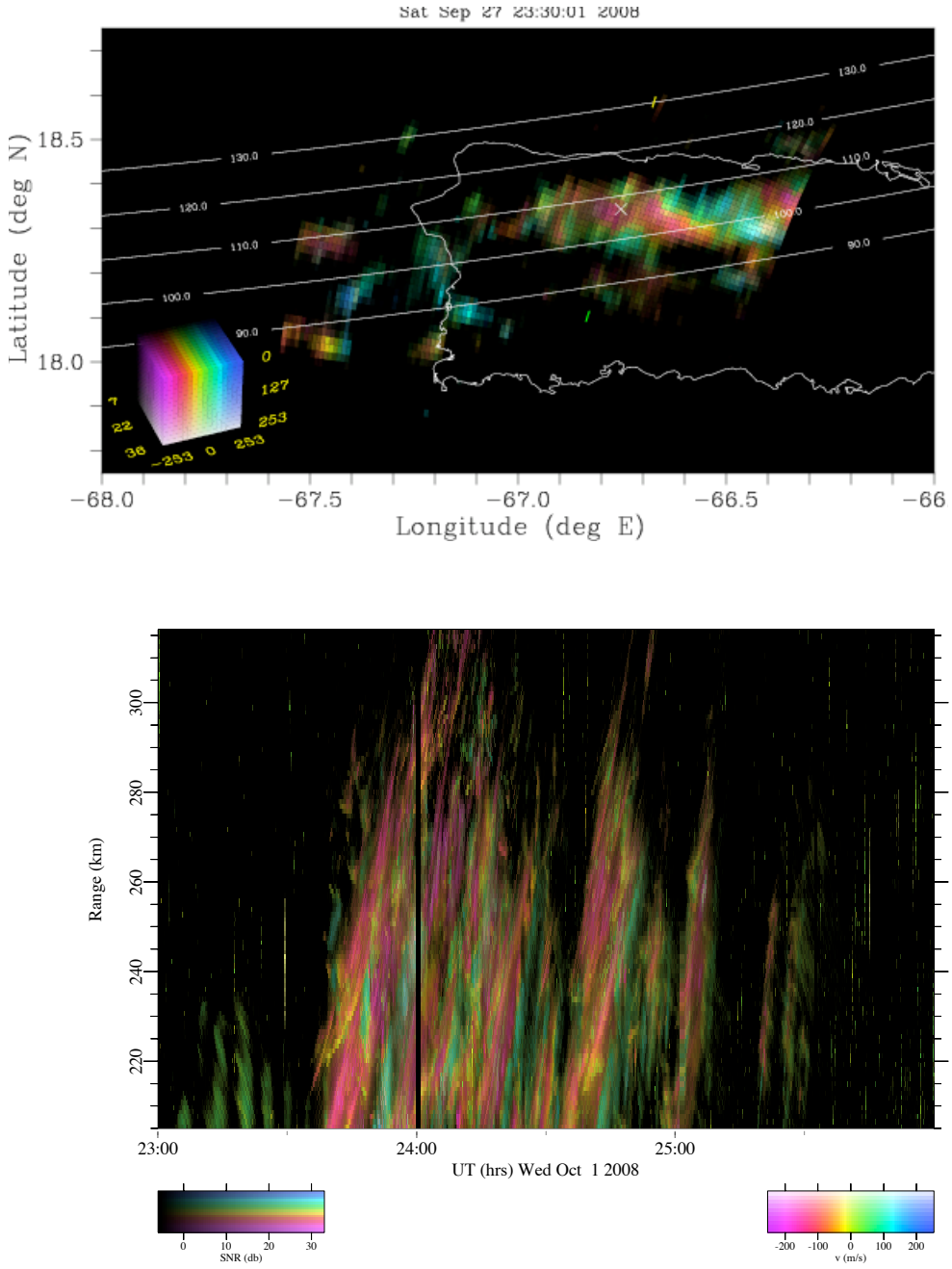

Figure 1.3: Nighttime irregularities over Arecibo at *E*-region heights when E_s is present. The irregularities presented in this Figure are known as quasi-periodic (QP) echoes. The echoes are observed with a coherent scatter radar located on St. Croix and looking perpendicular to **B** over Arecibo at 105 km. The first panel shows the propagating echoes over the island. The second panel shows the echoes registered by the radar as functions of time and altitude. The color scale indicates variations in Doppler, intensity, and spectral width.

Neutral instabilities can be produced by multiple forces. Dimensionless numbers have been used to quantify the importance of each force. The Richardson number (R_i) expresses the influence of the buoyancy or the shear, especially in stratified fluids. Smaller R_i represents fluids with dominant shear velocity. The velocity shear overcomes the tendency of the fluid to remain stratified generating turbulent flows and mixing when $R_i < 1/4$. This is known as the necessary but not sufficient condition for dynamic instability. In that regime, phenomena like the Kelvin-Helmholtz rolls are developed. Negative R_i values correspond to negative square buoyancy frequencies (N^2), generated by large inverse temperatures that disrupt the natural oscillations and propitiate breaking of the stratification, allowing mass parcels to ascend. When R_i is large, the fluid is buoyancy-driven and remains stratified.

$$R_i = \frac{N^2}{S^2} \tag{1.2}$$

where N is the buoyancy or Brunt-Väisälä frequency, U is the neutral wind, $S = \partial U/\partial z$ is the wind shear.

Similarly, the Rossby number (Ro) is the ratio of convection to the Coriolis force. The viscosity force ($v \cdot \nabla v \sim U^2/L$) overcomes the Coriolis force ($\Omega \times v \sim U\Omega$) when Ro is large. On the other hand, the flow rotates close to the planetary rotation when small Ro. Baroclinic instabilities are related to rapid rotation ($Ro < 1$) and stratified mediums ($R_i > 1$). This instability is the mechanism that gives the shape to the rotational winds in the atmosphere due to an unbalance between the pressure gradient and the density gradient.

$$Ro = \frac{U}{Lf} \tag{1.3}$$

where $f = 2\Omega \sin\phi$ is the Coriolis frequency, Ω is the angular frequency of planetary rotation, ϕ is the latitude and L is the characteristic scale length.

The objective of this thesis is to use the estimated neutral winds to analyze the MLT region and the various instabilities it may support to explore the origin and characteristics of the E region.

Structure of this dissertation

This dissertation explores possible neutral instabilities that could be occurring in the MLT region coinciding with E-region heights. The neutral winds have to be estimated to study the neutral activity. Chapter 2 explains how the winds are estimated using an inverse method and the modern capabilities at the Arecibo Observatory. An error analysis is performed to validate the methodology using a truth model that resembles the observed neutral winds by themselves or contaminated by perturbations (or gravity waves). This chapter also lays out experimental and theoretical foundations of ion-neutral coupling in the MLT region. The radar modes used at Arecibo are described in section 2.3, and the coupling equations for the neutral and the charged particles are described in section 2.4.

Examples of estimated neutral winds, electric fields, and temperatures from two ISR coordinated "World Day" campaigns at Arecibo are shown in Chapter 3. The ISR temperatures are compared with the MSIS-90 model estimates. The

neutral winds are compared with estimates from the MSIS-90 model and with potassium Doppler lidar observations. The neutral wind estimates are also compared with observations made with rocket-borne chemical releases, Na lidar, and with the Fabry-Perot Doppler interferometer carried by the TIMED satellite (TIDI).

The subsequent chapters are dedicated to studying instabilities, first from negative to positive R_i, during the day. Negative N^2 (and consequently negative R_i) is the indication of static instability. Values of R_i between 0 - 0.25 are a possible indication of the presence of dynamic instability. Chapter 4 explores static instability as the origin of *E*-layer irregularities. Chapter 5 studies dynamic stability as the source of billows and irregularities between 100 - 130 km.

The combined presence of $Ro < 1$ and $R_i > 1$ at the MLT region suggests that cyclone-type irregularities due to Coriolis effects can be formed. A study of reversals in the rotational diurnal neutral winds is performed in Chapter 6, looking for indicators of planetary-wave activity. The rotational changes are used to detect changes in areas dominated by the Coriolis or the Lorentz forces.

A summary of previously published work regarding nighttime dynamic-instability as an explanation for QP echoes is presented in Chapter 7. Analysis of the R_i and eigenfunction analysis is performed using estimated wind profiles.

A Discussion and summary are presented in the last chapter.

2

NEUTRAL WIND MEASUREMENT TECHNIQUE USING THE ARECIBO INCOHERENT SCATTER RADAR

"I wanted to adopt a name of the wind, but not "hurricane" or "breeze"; one day, I was impressed by the description of the wind made by Reclus in his famous work, and I found in it that name: Mistral."

– Gabiela Mistral, Poet

Summary

A method to estimate neutral winds in the MLT region is presented. The method uses inverse methods to estimate the neutral winds from data collected during the ISR coordinated World Day campaigns at Arecibo. This technique is compared with the experimental configuration and methodology used in the AIDA campaign run in 1989. An analysis to study the effects of different flow conditions on estimation errors is presented since AIDA suggested that the wind estimates could be contaminated by gravity waves. The new method is tested using a truth model which includes a rotational component (or Ekman spiral) at *E*-layer heights as well as a sinusoidal component representing gravity waves. A Monte Carlo error propagation analysis is performed to evaluate the accuracy of the obtained winds. Good agreement between the theoretical method and the estimated winds was obtained using an appropriate regularization parameter. Analysis of how error propagates for different horizontal wavelengths shows that the error decrease for wavelengths of the order of a planetary scale. Examples of how to set the regularization parameter according to the anticipated

gravity wave activity are presented. The new method can reconstruct the neutral winds in the mesosphere, suppressing the impact of data fluctuations and improving the accuracy of the model estimates.

2.1 Introduction

Measurement of the neutral winds in the MLT region is key to understanding the physical phenomena that govern the *E*-layer of the ionosphere. Neutral winds in the MLT region have been measured with several techniques: chemical releases [e.g., *Larsen* [2002], *Larsen et al.* [2005] and references therein] and Doppler lidar [e.g. *Zhao et al.* [2003] and *Chu et al.* [2005]], meteor trail echoes (*Elford* [1959], and references therein), and partial reflection (PR) using low and mid frequency (LF and MF) radars to obtain average winds using a technique developed by *Briggs* [1984] (e.g. *Manson et al.* [1985], *Vincent and Lesicar* [1991] and *Franke and Thorsen* [1993]). Recently, an effort to estimate the MLT wind fields has been undertaken over Europe using multi-static meteor radars (*Stober and Chau* [2015]). Also, efforts to estimate neutral winds at about 250 km using Oxygen optical emissions are been implemented by *Makela et al.* [2011], *Englert et al.* [2012], and *Harding et al.* [2015]. The MLT measurements yield information about the large-scale behavior of the winds. However, there is a lack of systematic observations about microphysics in the layer dynamics.

Hines et al. [1993] and others reported on an extensive effort to estimate the neutral winds in a special edition of Journal of Atmospheric and Terrestrial Physics (Vol 55, 1993) using measurements performed with the Arecibo ISR in 1989. The campaign was called Arecibo Initiative in Dynamics of the Atmosphere - AIDA. They used multiple-receiver MF/HF radars and multiple processing schemes like spaced antenna (SA), full correlation analysis, Imaging Doppler Interferometry (IDI) and beam synthesis. The results from the different techniques did not agree. *Kudeki et al.* [1993] in a subsequent analysis showed that the experimental configurations used were not optimal. The authors also

suggested that a rigorous analysis of the errors was needed due to an increase of systematic errors when gravity waves are present in the MLT region.

Hysell et al. [2009] used a new technique to estimate the neutral winds during a strong sporadic-*E* (E_s) layer at night. The data were collected with the Arecibo ISR using a dual-beam World Day experiment. Neutral winds and plasma temperatures were estimated using nonlinear least squares fitting of the autocorrelation functions. The algorithm fit all the variables at all altitudes at the same time. The methodology assumed that the winds were dominated by their horizontal components, and the vertical winds were neglected ($w = 0$), as well as the influence of the electric field ($E = 0$). They also assumed equal ion and neutral horizontal drift velocities ($u_h = v_h$). The composition was estimated assuming a combination of heavy Fe+ and light Mg+ metallic ions (with weights of 56 and 24) in thermal equilibrium. The ion drifts were estimated using the conjugate gradient inverse method. Finally, the Richardson number was calculated to identify the regions that were dynamically unstable.

Hysell et al. [2014] expanded the 2009 work to include the full set of neutral winds (horizontal and vertical) along with electrodynamic effects in the layer. Using an inverse method approach, the electric fields and daytime ion composition were obtained and used to estimate the ion drifts in the *E* layer. The methodology is described in the following section as well as the configuration of the Arecibo ISR experiments. The new algorithm is validated against a truth model which includes possible gravity-wave effects. The errors are estimated and analyzed.

2.2 Arecibo ISR - The old and new configurations

The AIDA campaign was performed in 1989. At the time of the campaign, only one ISR beam was available (the Gregorian reflector system was installed in 1997). Beam swinging was used during the experiment. The beam was confined to the magnetic meridional plane (in the $\hat{y}$ direction). The configuration is shown in Figure 2.1 a). When the AIDA winds were estimated, the effects of the electric field were neglected by restricting the beam to the direction parallel to the the magnetic field, and considering only the magnetic parallel direction in which the ion and neutral drifts are equal ($\mathsf{v}_{\parallel} = \mathsf{u}_{\parallel}$). Assuming homogeneous flow conditions ($u_y = 0$), the velocity ($\mathsf{u}_{\parallel}$) estimators depend upon the derivative of the vertical velocity (w_x). The doppler beam swinging estimate for the winds yields $\mathsf{u}_{\parallel} = (V_+ - V_-)/(2\sin\theta) = u_o + w_y z_o$ with the line-of-sight velocities:

$$V_+ = (w_o + w_y z_o \tan\theta)\cos\theta + (u_o + u_y z_o \tan\theta)\sin\theta \tag{2.1}$$

$$V_- = (w_o - w_y z_o \tan\theta)\cos\theta - (u_o + u_y z_o \tan\theta)\sin\theta \tag{2.2}$$

where u_o, w_o represent the wind components at the center of the radar volume $(0, 0, z_o)$. Also, y is the meridional direction, u_y, w_y stand for the partial derivative $\partial u/\partial y, \partial w/\partial y$ and θ is the zenith angle of the beam.

On the other hand, the new ISR coordinated World Day campaigns at Arecibo use two beams: the Gregorian and the line feed systems. This allows two pointing positions at the same instant in time. For the 2015 experiment, the beam formed with the line-feed system was fixed at zenith, and the beam from

the Gregorian was fixed at 15 degrees zenith and rotated in azimuth at a rate of 15 minutes per 360 degrees (see Figure 2.1 b)). The Gregorian beam direction alternated every 360 degrees: one turn was clockwise, the following was counterclockwise, and so on.

In the new experiments, the winds are estimated using the electrodynamics of the layer, including the effects of the electric and magnetic fields, as well as the daytime composition. The neutral winds dominate the dynamics of the lower altitudes of the *E*-layer. The electric field effects start to change the behavior of the layer at approximately $\approx$ 120 km, where the gyro to collision frequency is close to one. Such effects have not been considered in previous estimates of *E*-layer neutral winds. The new methodology also assumes that the vertical wind is horizontally uniform and that the electric field is the same in the *E* and *F* regions.

The differences between the AIDA and the World Day configurations are crucial and related to the configuration and capabilities of Arecibo and to the way in which the winds are estimated. The new configuration gives more parameters (See Figure 2.1 b)) by increasing the degrees of freedom. During the AIDA campaign, vertical variations in the horizontal winds could not be estimated (*Kudeki et al.* [1993]). The data parameters from the World Day campaign solve this shortcoming. Also, the new mode has the azimuth swing which allows the estimation of the complete vector winds. The AIDA winds were restricted to the parallel to **B** direction. With the new method, the three components of the neutral winds are estimated considering the effects of the **E** and **B**

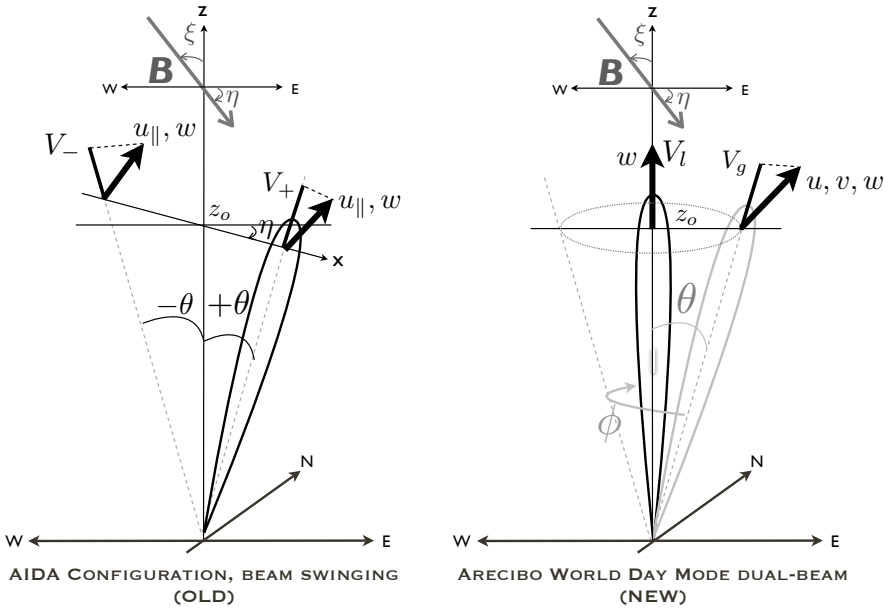

Figure 2.1: Configurations of the incoherent scatter radar at Arecibo Observatory. a) Before the Gregorian upgrade with only one beam and b) Current, with line feed (black) and Gregorian (gray) beams. The AIDA campaign allowed measurements of the line-of-sight drifts V_- and V_+ at different times in the direction parallel to **B** to estimate the horizontal component of the neutral wind ($u_\parallel$). The new configuration uses two beams simultaneously to estimate the three components of the neutral winds u, v, w.

fields, as well as composition, temperature, and density variations.

2.3 ISR coordinated World Day campaigns at Arecibo

As was described in the previous section, the World Day antenna configuration at Arecibo allows the estimation of the three components of the neutral winds using the new rotating Gregorian feed. Since these campaigns are organized a few times per year, an extensive database exists that can inform the behavior of

the *E* layer. Wind estimation is now being performed for these campaigns. The following section describes the transmitting modes used at Arecibo for these campaigns.

2.3.1 Transmitting modes

The estimation of the winds uses two of the transmitting modes of the World Day campaigns. Each mode targets a different set of ranges: the coded long pulse (CLP) is used to obtain measurements from the *E* layer and long multifrequency pulses (MRACF) from the *F* layer.

The long multifrequency pulses or MRACF code (*Sulzer* [1986a]) is a technique used when the signal-to-noise ratio is very high, as in studies of the *F* region at Arecibo. The technique increases the number of independent samples (K) to reduce the mean square statistical error ($MSE = \frac{(1+N/S)^2}{K}$) (*Farley* [2009]). It spreads the powerful transmitted signal over seven independent transmitted frequencies using phase modulation. A computer program generates a code using $+$, $-$, or 0 characters to obtain the best possible spectrum with n uniformly-spaced lines with uniform amplitude and with a maximum deviation of 1 dB. The code has a baud width of $4\mu s$ which corresponds to the maximum bandwidth (250 MHz) allowed by the array processor at Arecibo. Each baud is subdivided in four characters (each one of $1\mu s$), creating a code of $28\mu s$ which is repeated 11 times. Considering the composition of the *F* region, the frequency separation between the emitted codes is 30 kHz, accommodating the typical 12 kHz O^+ spectrum (and most of the H^+ spectrum) at 430 MHz transmitting frequency. This condition also guarantees that the spacing is wide enough to

sample independently scattered signals. The backscatter signals from the seven transmitted frequencies are captured with only one 2 MHz-bandwidth receiver. The signal is processed using Fast Fourier transforms (FFTs) to generate a complex spectrum which is later converted to an ACF by replacing the negative lags for the positive. A correction to the lags in the ACF should be done to center them at the same range. Taking the inverse FFT of the corrected ACF produces the real power spectrum needed to measure the ion drifts. The MRACF technique produces ion drifts in the *F* layer with narrower standard deviation than the predecessor "long pulse" technique.

The CLP (*Sulzer* [1986b]) pulses are widely used to observe the *E* layer. The transmitted CLP is a pseudo-random code that minimizes the uncorrelated clutter from unwanted ranges in the returned signal. This is made possible by using a single long pulse with the same length as the predecessor "multi-pulse" technique. The long-pulse is modulated with a binary phase code with a baud length A and code length N. The binary phase code is selected at random for half of the transmitted pulses. The received signal is the sum of the wanted signal from the specific range and the unwanted clutter from other ranges. Since the every returned signal has been multiplied by a unique random code, each looks like random noise. Over many pulses, the noise flattens, and only the information from the desired range is left (*Farley* [2009]).

2.4 Estimating the neutral winds in the *E*-layer

The equations of motion that govern the ion dynamics in the *E* region are derived from the coupled equations for neutral, ion, and electron particles:

$$\begin{aligned}
\rho_n \frac{d\mathsf{u}}{dt} &= -\nabla p_n - 2\rho_n \mathbf{\Omega}_E \times \mathsf{u} + \rho_n \mathsf{g} + \mu \nabla^2 \mathsf{u} + m_i n_i \nu_{in}(\mathsf{v}_i - \mathsf{u}) \\
&\quad + m_e n_e \nu_{en}(\mathsf{v}_e - \mathsf{u}) \qquad (2.3) \\
m_i n_i \frac{d\mathsf{v}_i}{dt} &= -\nabla p_i + m_i n_i \mathsf{g} + n_i q(\mathbf{E} + \mathsf{v}_i \times \mathbf{B}) - m_i n_i \nu_{in}(\mathsf{v}_i - \mathsf{u}) \qquad (2.4) \\
0 &= -\nabla p_e - q n_e(\mathbf{E} + \mathsf{v}_e \times \mathbf{B}) - m_e n_e \nu_{en}(\mathsf{v}_e - \mathsf{u}) \qquad (2.5)
\end{aligned}$$

The subscripts (n, i, e) correspond to the neutral, ion and electron particles moving with velocities u, v_i and v_e, respectively. For midlatitude E-layer conditions, the collisions frequencies with neutrals $\nu_{in} \sim 10^3\ s^{-1} << \nu_{en} \sim 10^6\ s^{-1}$. The magnitude of the Earth's angular velocity is $\mathbf{\Omega}_E \sim 7.3 \times 10^{-5}$ rad/s. To decouple the electric field, the equations for the charged particles are added::

$$\begin{aligned}
m_i n_i \frac{d\mathsf{v}_i}{dt} &= -\nabla(p_i + p_e) + m_i n_i \mathsf{g} + q(\mathbf{E}(n_i - n_e) + (n_i \mathsf{v}_i - n_e \mathsf{v}_e) \times \mathbf{B}) \\
&\quad - m_i n_i \nu_{in}(\mathsf{v}_i - \mathsf{u}) - m_e n_e \nu_{en}(\mathsf{v}_e - \mathsf{u}) \qquad (2.6)
\end{aligned}$$

Neglecting electron pressure gradients and electron neutral collisions (ν_{en}) in equation (2.5), the electrons drift under the influence of the electric field with a velocity $\mathsf{v}_e = \mathbf{E} \times \mathbf{B}/B^2$, also known as plasma drift velocity. Compared with collisions, gravity and pressure gradients are negligible at E-layer heights. Then, assuming quasi-neutrality ($n \sim n_i \sim n_e$) and neglecting the effects of gravity and gradients in pressure and neutral-electron collisions (because $m_i \nu_{in} >> m_e \nu en$), the equation remaining is:

$$m_i \frac{d\mathsf{v}_i}{dt} = -q\left(\frac{\mathbf{E} \times \mathbf{B}}{B^2} - \mathbf{v}_i\right) \times \mathbf{B} - m_i \nu_{in}(\mathsf{v}_i - \mathsf{u})$$

For simplicity, a change of variables is implemented: $m = m_i$, $v = v_i$ and $\nu = \nu_{in}$:

$$m\frac{d\mathsf{v}}{dt} = q(\mathbf{E} + \mathsf{v} \times \mathbf{B}) - m\nu(\mathsf{v} - \mathsf{u}) \tag{2.7}$$

Taking the cross product of the equation (2.7) with $\mathbf{B}$, the perpendicular component of the ion drift is obtained. Taking the dot product with $\mathbf{B}$, the parallel component is obtained. Neglecting ion motion, the expressions for the ion drifts are:

$$\begin{aligned} \mathsf{v}_{\parallel} &= \mathsf{u}_{\parallel} \\ \mathsf{v}_{\perp} &= \frac{\mathbf{E} \times \mathbf{B}}{\mathtt{B}^2} r_0 + \frac{\mathbf{E}_{\perp}}{\mathtt{B}} r_1 + \mathbf{u} \times \hat{b} r_1 + \mathsf{u}_{\perp} r_2 \end{aligned} \tag{2.8}$$

where

$$\begin{aligned} r_0 &= \sum_j \frac{1}{1 + \nu_j^2/\Omega_j^2} \\ r_1 &= \sum_j \frac{\nu_j/\Omega_j}{1 + \nu_j^2/\Omega_j^2} \\ r_2 &= \sum_j \frac{\nu_j^2/\Omega_j^2}{1 + \nu_j^2/\Omega_j^2} \end{aligned}$$

where the electric field, ion drifts and neutral winds are, respectively, $\mathbf{E} = (\mathsf{E}_{\perp e}, \mathsf{E}_{\perp n}, \mathsf{E}_{\parallel})$, $\mathsf{v}_{\perp} = (\mathsf{v}_{\perp e}, \mathsf{v}_{\perp n}, 0)$, $\mathsf{v}_{\parallel} = (0, 0, \mathsf{v}_{\parallel})$ and $\mathsf{u} = (\mathsf{u}_{\perp e}, \mathsf{u}_{\perp n}, \mathsf{u}_{\parallel}))$ in the reference frame of the magnetic field coordinate system, with $\mathbf{B} = (0, 0, \mathtt{B})$ and the unitary vector $\hat{b} = (0, 0, 1)$. The symbol $\perp$ indicates perpendicular or $\parallel$ parallel to $\mathbf{B}$, and $\perp e$ and $\perp n$ are perpendicular in the east and north direction, respectively. The ratios r_0, r_1, r_2 are functions of the ion gyro frequency Ω_j and

ion-neutral collision frequency ν_j for each species (j). For multiple ion species, the ratios are the sum of the ratios of the individual components, weighted by the proportion of every species in the total composition.

The neutral winds in the E layer dominate the ion dynamics as the ratio of the gyrofrequency to collision frequency is comparable to or less than unity. In the E region, the coefficient r_2 from the equation (2.8) (e) is order unity, and the coefficients r_0, r_1 are smaller. To calculate these coefficients, the specific composition ratios from each species should be calculated.

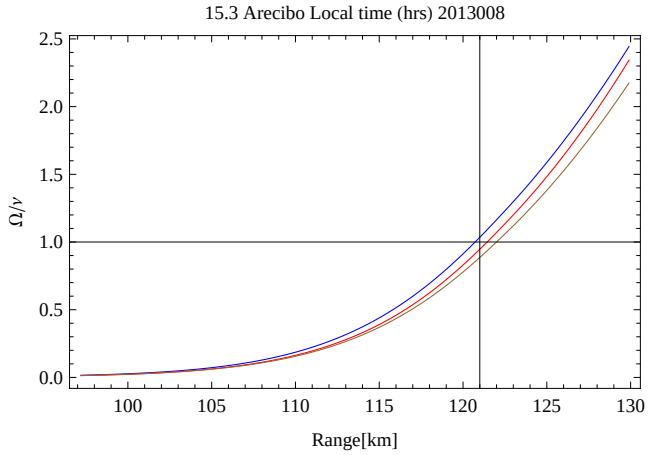

Figure 2.2: Example ratios of gyro- to collision- frequencies for Arecibo daytime conditions. Three compositions are shown: O+ (blue), NO+(red), O2+(brown).

At F-region heights, the ratio gyro to collision frequency is $\Omega/\nu >> 1$ which indicates that the perpendicular component of the ion drifts are proportional to $\mathbf{E} \times \mathbf{B}$ (or $r_0 >> r_1 >> r_2$ with $r_0 \approx 1$). The perpendicular component of the ion drifts at F layer heights is:

$$\mathsf{v}_{\perp F} = \frac{\mathbf{E} \times \mathbf{B}}{\mathbb{B}^2} r_0 = \frac{1}{\mathbb{B}} \begin{pmatrix} E_{\perp n} \\ -E_{\perp e} \end{pmatrix}_F \tag{2.9}$$

showing that the perpendicular ion drifts at F region heights are proportional to the perpendicular electric fields. Since it is assumed that **B** field lines are equipotentials, which results in a height-invariant **E** field (or $\mathbf{E}_F = \mathbf{E}_E$ for the E and F-regions). The E-field can be estimated using the ISR data from the F-region.

To solve the system in the equations (2.8), the **E** field and the compositions have to be estimated. *Hysell et al.* [2014] used an inverse methods approach to solving the system as will be explained in the following subsections.

2.4.1 Electric fields

The electric fields are generally expressed in terms of magnetic coordinates. However, the Arecibo measurements produce data in a combination of absolute geographic coordinates and relative position (range and beam coordinates). To find an expression of the Arecibo ion drifts in term of the magnetic coordinates, it is necessary to make a series of transformations.

First, for any radar range bin, the acquired ion drifts for each beam (l, g) at Arecibo can be written in terms of a geographic Cartesian (up, east, north) coordinate system, as follows:

$$\begin{pmatrix} \mathsf{v}_l \\ \mathsf{v}_g \end{pmatrix} = \underbrace{\begin{pmatrix} 1 & 0 & 0 \\ c\theta & s\phi s\theta & c\phi s\theta \end{pmatrix}}_{Q} \begin{pmatrix} \mathsf{v}_{up} \\ \mathsf{v}_E \\ \mathsf{v}_N \end{pmatrix} \tag{2.10}$$

Where θ and ϕ are the azimuth and zenith angles of Arecibo beams. The az-

imuth angle varies in time according to the rotation rate of the Gregorian feed. The line feed is fixed at zenith ($\phi = 0$), and the Gregorian feed is inclined ($\phi \approx 15\,\text{deg}$). The "s" and "c" are shorthands for sin and cosine.

Second, the drifts are projected into the components of the magnetic field: parallel ($\|$), perpendicular to the horizontal ($\perp_E$), and perpendicular to the meridional ($\perp_N$) plane. The magnetic field is defined by its zenith ξ and azimuth η angles.

$$\begin{pmatrix} \mathsf{v}_{up} \\ \mathsf{v}_E \\ \mathsf{v}_N \end{pmatrix} = \underbrace{\begin{pmatrix} c\xi & 0 & s\xi \\ s\eta s\xi & c\eta & -s\eta c\xi \\ c\eta s\xi & -s\eta & c\eta c\xi \end{pmatrix}}_{R} \begin{pmatrix} \mathsf{v}_{\|} \\ \mathsf{v}_{\perp_E} \\ \mathsf{v}_{\perp_N} \end{pmatrix} \tag{2.11}$$

Finally the transformation matrix that relates the beam and the geographic coordinates is:

$$\begin{pmatrix} \mathsf{v}_l \\ \mathsf{v}_g \end{pmatrix} = QR \begin{pmatrix} \mathsf{v}_{\|} \\ \mathsf{v}_{\perp_E} \\ \mathsf{v}_{\perp_N} \end{pmatrix} \tag{2.12}$$

where

$$S = \underbrace{\begin{pmatrix} c\xi & 0 & s\xi \\ c\theta c\xi + s\theta s\xi(s\phi s\eta + c\phi c\eta) & s\theta(s\phi c\eta - c\phi s\eta) & s\xi c\theta - c\xi s\theta(s\phi s\eta + c\phi c\eta) \end{pmatrix}}_{S=QR} \tag{2.13}$$

Since the Arecibo beams acquire data corresponding to n distinct times, the previous matrix belongs to $\mathbb{R}^{2n\times 3n}$ and can be written as follows:

$$\begin{pmatrix} \mathsf{v}_{l1} \\ \mathsf{v}_{g1} \\ \vdots \\ \mathsf{v}_{ln} \\ \mathsf{v}_{gn} \end{pmatrix} = \begin{pmatrix} S_1 & & \\ & \ddots & \\ & & S_n \end{pmatrix} \begin{pmatrix} \mathsf{v}_{\parallel 1} \\ \mathsf{v}_{\perp_E 1} \\ \mathsf{v}_{\perp_N 1} \\ \vdots \\ \mathsf{v}_{\parallel n} \\ \mathsf{v}_{\perp_E n} \\ \mathsf{v}_{\perp_N n} \end{pmatrix} \tag{2.14}$$

This transformation matrix has the form of a discrete linear inverse problem $Gm = d$. The data vector d has $2n$ observations and the model vector m has $3n$ parameters.

The matrix G for this case is not square, and it is an underdetermined problem. However, this can be seen as an optimization problem, where the introduction of additional penalties can create a unique solution. *Hysell et al.* [2014] uses weighted damped least squares to seek the best solution m from a statistical point of view (*Aster et al.* [2005]).

$$m = \underset{m}{argmin}\ (Gm - d)^t\ W_d\ (Gm - d) + \alpha^2\, m^t\, W_m\, m$$

where the maximum likelihood estimate of the model is:

$$\hat{G}^{-1} = (G^t W_d G + \alpha^2 W_m)^{-1} G^t W_d \tag{2.15}$$

$$m \approx \hat{G}^{-1} d \tag{2.16}$$

Here, W_d is the data error covariance matrix and W_m is a model weight matrix. The weight matrix can be used as a penalty for spurious temporal fluctuations not supported by the data. This expression reflects the use of second-order Tikhonov regularization. It was used to minimize the "roughness" of the model trough an appropriate selection of W_m. The α term is a regularization parameter that balances the impacts of the penalties.

The described methodology yields the perpendicular ion drifts for the F region, needed to estimate the **E** fields that propagate to the E layer and needed to estimate the neutral winds.

2.4.2 Ion composition

Hysell et al. [2014] followed a theoretical photochemical model for the ion densities in the F region (*Richards et al.* [2010]) and adopted it for the E region assuming thermal and photochemical equilibrium and neglecting transport. Considering O^+, O_2^+ and NO^+, the balance equations are:

$$\begin{aligned} & & \textit{Production} & & \textit{Removal} \\ O_2^+ : & \quad \alpha N[O^+]N[O_2] = & \gamma N[O_2^+]N[e^-] \\ NO^+ : & \quad \beta N[O^+]N[N_2] = & \delta N[NO^+]N[e^-] \end{aligned} \tag{2.17}$$

Where α and β are the rate coefficients for charge exchange and γ and δ are the coefficients for dissociative recombination, respectively, which depend on electron temperature, T_e. The temperature is obtained by fitting the ISR Arecibo spectra to the theoretical curve, assuming $T = T_e = T_i$. This assumption is

valid for altitudes lower than 200 km, where the collision with neutrals dominates the heat exchange. Using the chemical coefficients from *Schunk and Nagy* [2004] as well as ion-neutral collision frequencies and neutral density estimates from NRLMSISE-00 model, the equations (2.17) are solved algebraically for the number density fraction of the molecular species for a given temperature. Then, iteration between temperature and composition estimates is done to fit the electron temperature.

The electron density is estimated from the ISR power profiles using a normalization constant defined from the common-volume ionosondes.

2.4.3 Neutral winds

The neutral winds are estimated for the MLT region using inverse methods. To organize the system in a matrixial form, the equations (2.8) and (2.9) are written organized by terms pertinent to the *E* and *F* layers, as follows:

$$\begin{pmatrix} \mathsf{v}_{\parallel} \\ \mathsf{v}_{\perp e} \\ \mathsf{v}_{\perp n} \end{pmatrix}_{E} - \underbrace{\begin{pmatrix} 0 \\ -r_0\mathsf{v}_{\perp e} - r_1\mathsf{v}_{\perp n} \\ r_0\mathsf{v}_{\perp n} + r_1\mathsf{v}_{\perp e} \end{pmatrix}_{F}}_{U} = \underbrace{\begin{pmatrix} 1 & 0 & 0 \\ 0 & r_2 & r_1 \\ 0 & -r_1 & r_2 \end{pmatrix}}_{V} \begin{pmatrix} \mathsf{u}_{\parallel} \\ \mathsf{u}_{\perp e} \\ \mathsf{u}_{\perp n} \end{pmatrix} \tag{2.17}$$

Here, the velocities for the *E* region are inside the parenthesis under the the subscript *E*. The *F* subscripts indicate that the velocities in the parenthesis are deduced from *F* region measurements and *F* region ion drifts. Multiplying both sides of equation (2.17) by the matrix *S* from equation (2.12) gives:

$$\begin{pmatrix} v_l \\ v_g \end{pmatrix}_E - SU = SV \begin{pmatrix} u_{\parallel} \\ u_{\perp E} \\ u_{\perp N} \end{pmatrix}, or$$

$$\begin{pmatrix} v'_l \\ v'_g \end{pmatrix} = Y \begin{pmatrix} u_{\parallel} \\ u_{\perp E} \\ u_{\perp N} \end{pmatrix} \tag{2.18}$$

The primed quantities are line-of-sight ion drifts for the E region with electric field corrections. The matrix $Y \in \mathbb{R}^{2\times 3} = SV$ refers to a single time and range measurement. When data are acquired at n times and in m ranges independently, the more general matrix is:

$$\begin{pmatrix} v'_{l1,1} \\ v'_{g1,1} \\ \vdots \\ v'_{lm,n} \\ v'_{gm,n} \end{pmatrix} = \underbrace{\begin{pmatrix} Y_{1,1} & & \\ & \ddots & \\ & & Y_{m,n} \end{pmatrix}}_{Z\in\mathbb{R}^{2mn\times 3mn}} \begin{pmatrix} u_{\parallel 1,1} \\ u_{\perp E1,1} \\ u_{\perp N1,1} \\ \vdots \\ u_{\parallel m,n} \\ u_{\perp Em,n} \\ u_{\perp Nm,n} \end{pmatrix} \tag{2.19}$$

The size of the matrix Z depends on the experiments which usually involve hundreds of ranges and time steps. To solve the system in equation (2.19), an iterative method is employed since the matrix inversion of Z is computationally expensive. *Hysell et al.* [2014] uses the conjugate gradients least squares or CGLS method using sparse mathematics. This method does not require any matrix inversion.

The CGLS method finds the solution for the equation (2.16) by solving the least squares problem: $(G^t W_d G + \alpha^2 W_m)m = G^t W_d d$ by finding the residual of the normal equations (*Aster et al.* [2005]):

$$\widetilde{G}^t(\widetilde{G}m - d) \approx 0 \tag{2.20}$$

where

$$\widetilde{G} \equiv \begin{pmatrix} W_d^{1/2} G \\ \alpha W_m^{1/2} \end{pmatrix}$$
$$\widetilde{d} \equiv \begin{pmatrix} W_d^{1/2} d \\ 0 \end{pmatrix}$$

with

$$W_m = \begin{bmatrix} 1 & 1 & & & & \\ & 1 & -2 & 1 & & \\ & & & \ddots & & \\ & & & & 1 & 1 \end{bmatrix}$$

and iterating:

$$s_k = \widetilde{d} - \widetilde{G} m_k$$
$$res_k = \widetilde{G}^t s_k$$

The matrix expression for $\widetilde{G}$ and $\widetilde{d}$ are the first row of matrices augmented by the rows of the second matrix or by zeros. The notation in the weight matrices

mean: $W_i = W_i^{1/2\,t} W_i^{1/2}$. Here, W_m enforces second-order Tikhonov regularization in altitude and time, penalizing spurious spatiotemporal fluctuation. The weight matrices are positive definite.

The neutral winds are obtained for the *E*-layer by minimizing the residual (res_k) of the equation (2.20) through this iterative method.

2.5 Testing the method

After the AIDA campaign, *Kudeki et al.* [1993] warned about the impossibility of truly reconstructing the neutral winds, mainly because of the radar technology available to collect the data. Also, they warned about possible data contamination by gravity waves. The main objective of this section is to study how the numerical method behaves in the reconstruction of (first) a theoretical model for the rotating neutral winds in the absence of gravity waves and (then) a model including different gravity waves to observe how the wind estimates diverge from the theoretical model. The theoretical model chosen to represent the neutral winds is the Ekman spiral, as shown in the following section.

2.5.1 First truth model - Ekman spiral

The Ekman spiral corresponds to the solution of the surface wind drift current in the ocean (*Holton* [2004]) and similar conditions in atmospheric boundary layers. The Ekman spiral was named for the oceanographer V.W. Ekman who first solved this system. This solution represents some of the most relevant characteristics of the neutral winds in the lower thermosphere: rotation, steep shears

and peak speeds of the order up to 150 m/s around E_layer heights (*Larsen* [2002]). The Ekman spiral is described as:

$$\begin{aligned} u_{ek} &= u'(r)\cos(\alpha) + v'(r)\sin(\alpha) \\ v_{ek} &= -u'(r)\sin(\alpha) + v'(r)\cos(\alpha) \\ w &= 0 \end{aligned}$$

where α is the angle of rotation of the spiral, r is the relative height and the parameters s, u' and v' are:

$$\begin{aligned} s &= 2\pi\,\frac{z-100}{50} \\ u' &= 100\left[1 - e^{-s}\cos(s)\right] \\ v' &= 100\left[e^{-s}\sin(s)\right] \end{aligned}$$

The methodology explained in the previous section was applied to estimate the neutral winds, and this is the result. The oscillatory horizontal and the null vertical winds are very well reconstructed, as seen in Figure 2.3.

2.5.2 Complete truth model - Ekman spiral and gravity waves

Kudeki et al. [1993] showed that estimates of the winds from the AIDA campaign could have systematic errors due to sinusoidal wind variations. The presence of gravity waves in the lower ionosphere has been an object of study for many

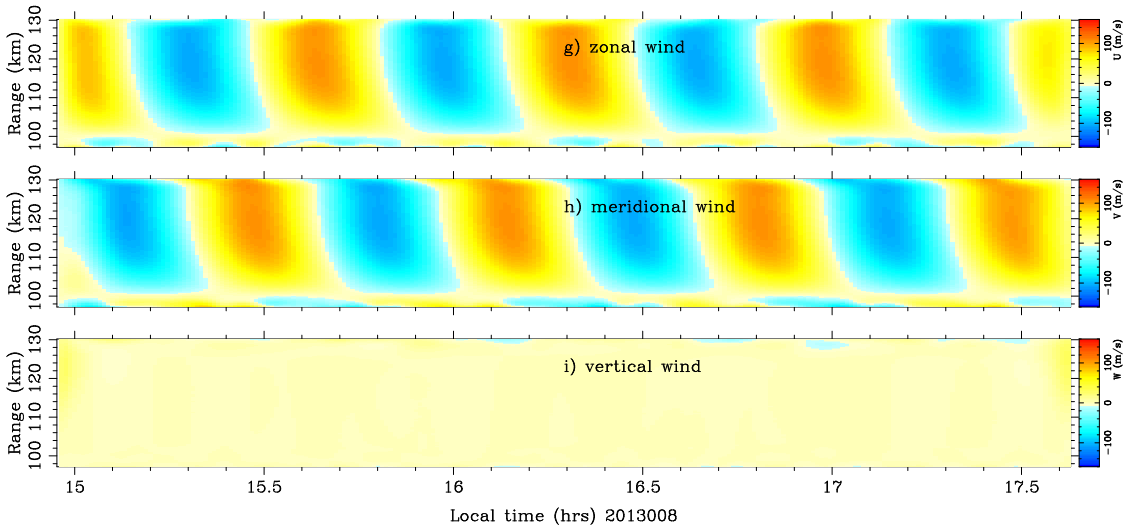

Figure 2.3: Estimated winds for a Ekman spiral truth model

decades (*Fritts and Alexander* [2003]). The major influence of the gravity waves occurs below 110 km because of the decreasing density at higher altitudes. To test the model, a gravity wave was superimposed on the Ekman spiral winds detailed in the previous section.

The Arecibo beam can sample the propagating wave (Ekman spiral and gravity wave) where the beams of the ISR intersect the wave at certain instants of time. According to the position of the beam, the winds can be decomposed into a coordinate system as follows:

$$
\begin{aligned}
u_{gw} &= A\cos(\theta_{gw})\sin(\phi_{gw})\cos(\psi) \\
v_{gw} &= A\cos(\theta_{gw})\cos(\phi_{gw})\cos(\psi) \\
w_{gw} &= -A\sin(\theta_{gw})\cos(\psi)
\end{aligned}
$$

where the phase, ψ, depends on the characteristics of the gravity wave (horizontal wavelength λ_x, vertical wavelength λ_z, frequency f, and wave number N), the virtual height of the wave (r), the angle ϕ and the elevation θ of the beam.

$$\begin{aligned} \psi &= r\,\frac{f}{N}\Big[\cos(\theta)\cos(\theta_{gw}) + \sin(\theta)\sin(\theta_{gw})\cos(\phi - \phi_{gw})\Big] - t\,f \\ f &= N\sqrt{\frac{1}{\lambda_x^2 + \lambda_z^2}} \end{aligned}$$

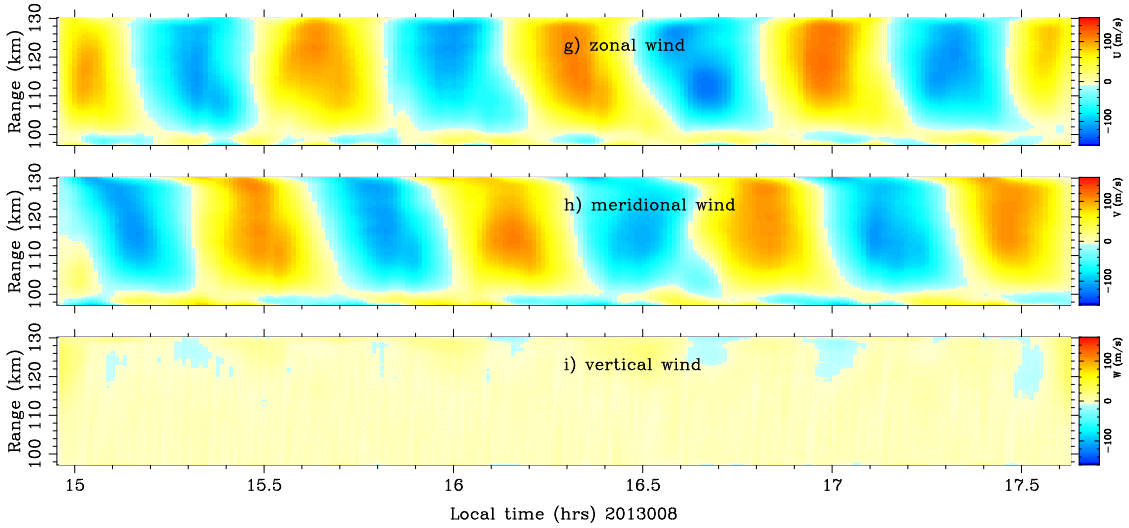

Figure 2.4: Estimated winds for an Ekman spiral plus a gravity wave with a horizontal wavelenght of $\lambda_x = 25$ km.

The Figure 2.4 shows an example where the winds were estimated when the truth model was conformed by the Ekman spiral and the gravity waves. The parameters for the gravity wave were: horizontal wavelength $\lambda_x = 25$ km, vertical wavelength $\lambda_z = 15$ km, amplitude $A = 10$ m/s, and period $= 10$ min. The estimated horizontal components resemble the values recovered from the

Ekman spiral alone, and the vertical component started to have some structure with values that could resemble the actual observations from the *E* layer.

2.5.3 Selecting the optimal regularization parameter

The optimal solution for the estimated neutral winds is the one that minimizes the error between the reconstruction and the data, or in this case the model and the truth model. In Figure 2.5, we compare the truth model and the wind estimates performed by the algorithm. The algorithm used has a regularization parameter that could be tuned to minimized the errors. A technique called L-curve is used to select the best regularization parameter. With this technique, the regularization parameter sets an optimal balance between the the errors due to perturbation versus the regularization effects, as it is explained in the following section. Then, the regularization parameter could minimize error perturbations when the data is contaminated by oscillated short-wavelength gravity waves. The optimal regularization parameter for the measurements is associated with the selection of the good model to estimate the winds. The error analysis of the model (with a fix regularization parameter) is performed by the standard Monte Carlo analysis, which statistically measures the deviation of the wind estimates from the original data. The following sections will expand the selection of the regularization parameter, and then the error analysis is going to be performed.

L-curve

The objective of the wind estimation algorithm is to minimize the residual. However, what is the best way to minimize the residual to fit the data to the

real model? The optimal solution can be obtained by adjusting a regularization parameter, α, included in the method (See equation (2.20)). The wind estimates of Figure 2.5 recover the essence of the theoretical model, but there is a question of how to set the regularization parameter to find the most accurate solution and to reduce spurious fluctuations.

First, a procedure for finding the optimum balance between the optimal value of the norm of the model $||m||_2$ and $||\widetilde{G}m - \widetilde{d}||_2$, called L-curve, is performed. This graphic tool displays the trade-off between the size of the regularized solution and the data due to the changes in the regularization parameter (*Hansen* [2001]). Figure 2.6 shows some examples for different parameters of the truth model. Here, the optimum α should be the one in the inflection point which is the point that divides the solutions dominated by regularization errors ($||m||_2$) from the solutions dominated by perturbation errors ($||Gm - d||_2$). When plotting diverse examples, we observed that the L-curve optimal regularization parameter changes when the gravity wave parameters change.

The best regularization parameter should guarantee the best match between the regularized solution and the data or in our case, the truth model. To understand these L-parameter changes, an analysis of the dependence of the variations according to the regularization parameter was done. The average on-time and range, $\bar{\sigma}$, of the standard deviation for every profile of the difference between the Truth model and the estimated values was obtained and is presented in the Figure 2.7. The best fitting model is then obtained using the regularization parameter that corresponds to the minimum value of $\bar{\sigma}$. Here, the regularization parameters seem to guarantee a most accurate recovery of the characteristics of the oscillations of the winds. For future analysis the optimal regularization pa-

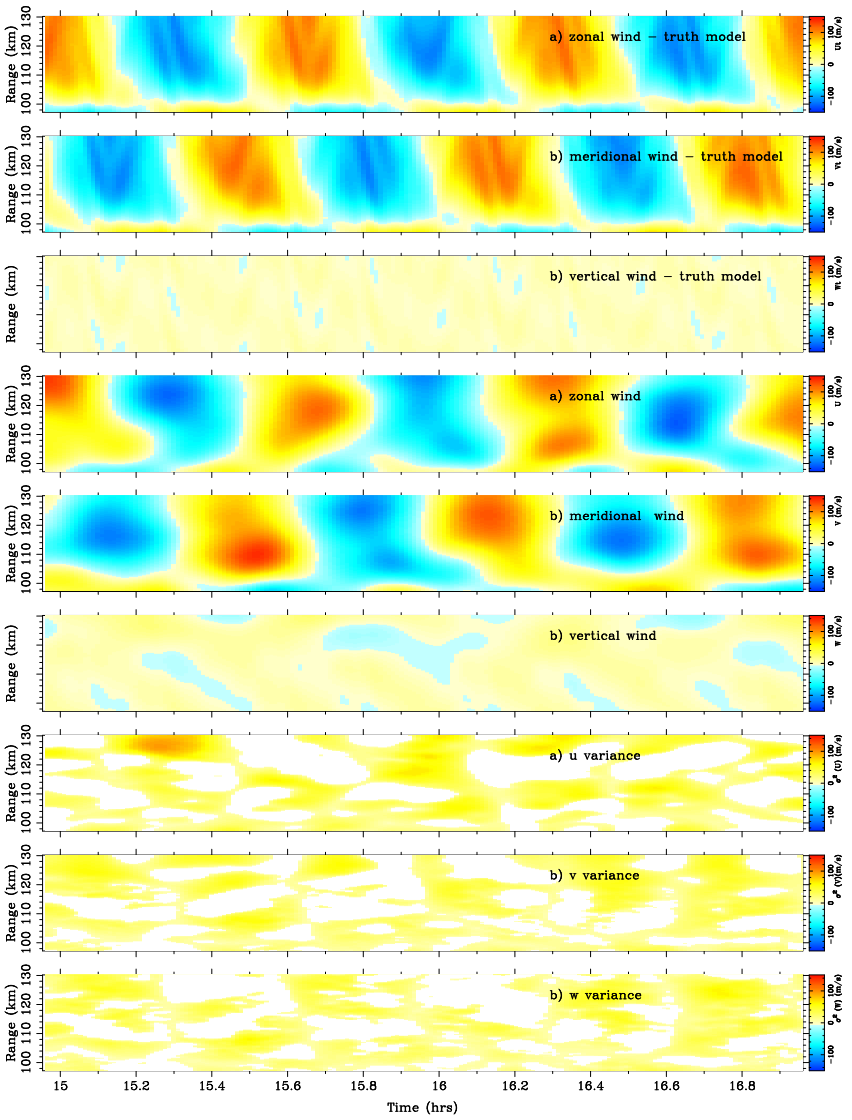

Figure 2.5: Panels a, b, c correspond to the zonal, meridional and vertical wind components of the truth model. Panels d, e, f are the wind components of the wind estimations performed with the numerical model. The last three panels are the difference of the two models. The truth model included the Ekman spiral and gravity waves with horizontal wavelength $\lambda_x = 50$ km, vertical wavelength $\lambda_z = 30$ km, amplitude $A = 15$ m/s and period of 10 min. The regularization parameter for the numerical method is: $\alpha = 0.075$. The difference is close to zero for a large set of the estimated values. However, *Hysell et al.* [2014] advised about the increasing discrepancies at the top altitudes, as they are also observed here.

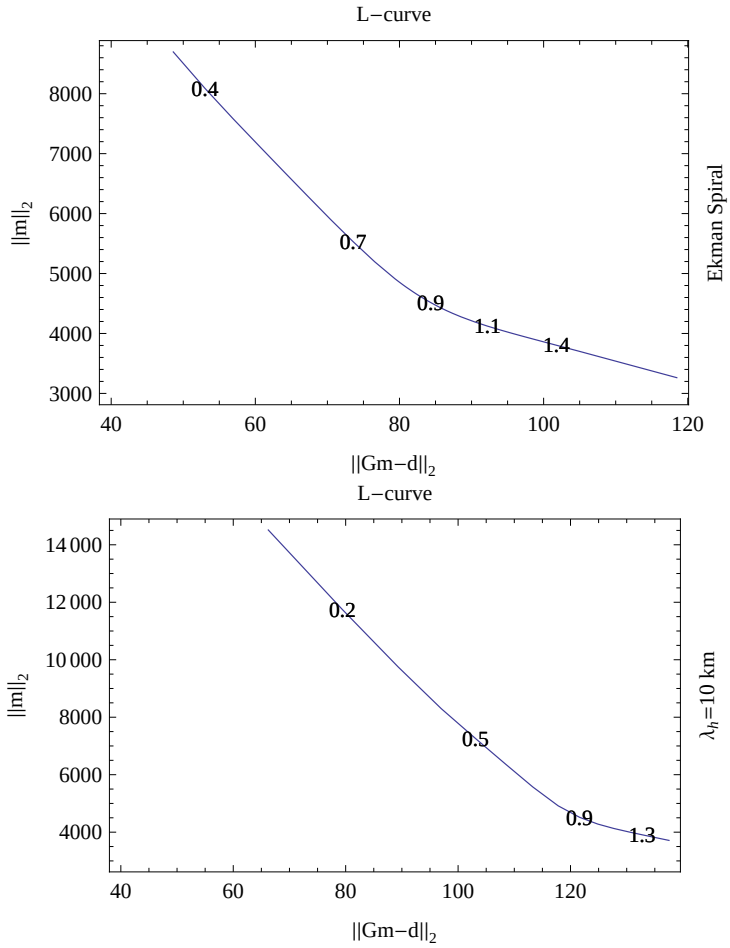

Figure 2.6: L-curve for the truth model. The trade-off between the norm of the model and the perturbation changes according with the regularization parameter values, α, shown over the line. The inflection point is obtain with $\alpha \sim 0.9$ for the Ekman Spiral, or when gravity waves are included with horizontal wavelength $\lambda_h = 10$ km.

rameter that minimizes the disparity between the models will be chosen using the latest technique.

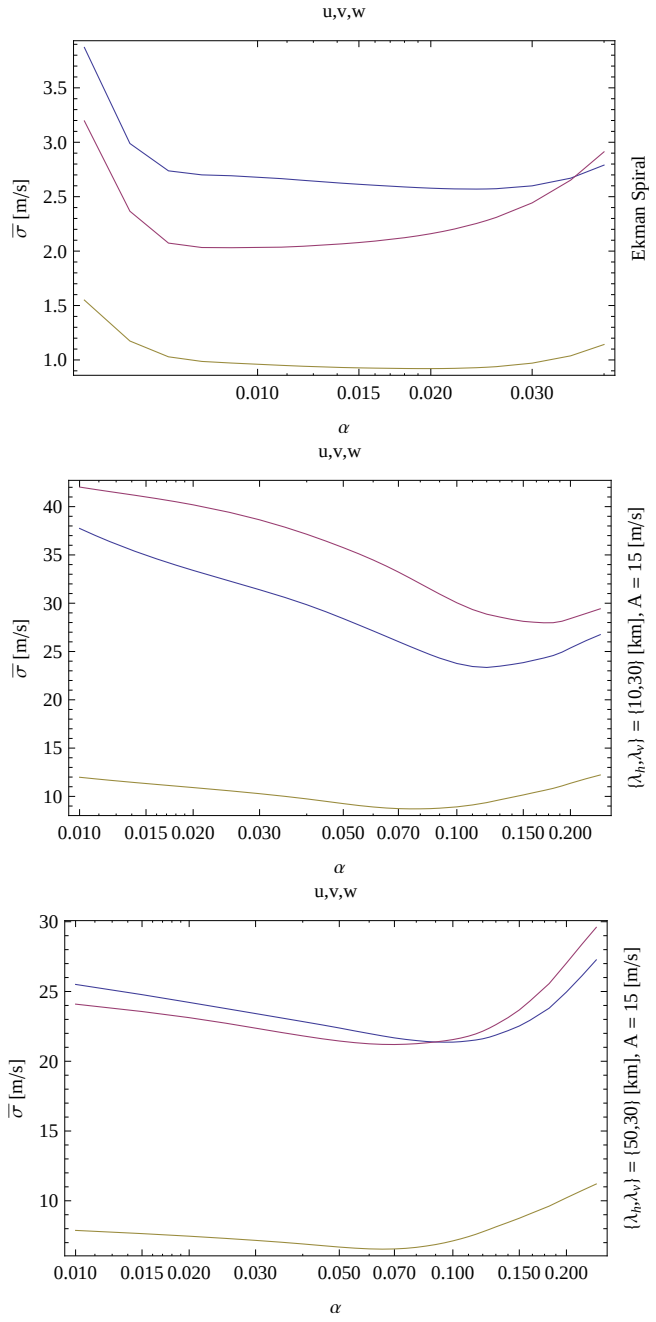

Figure 2.7: Regularization parameter for the Ekman Spiral and for Gravity waves with horizontal wavelength of 10 and 50 km superposed to the Ekman spiral. Here, the average on time and range of the standard deviations for every wind profile component are depicted in the color: red (u) , blue (v), yellow (w). The optimized α parameters for every case are: for Ekman spiral: $\alpha(u,v,v) = (0.024, 0.009, 0.02)$, for λ_h = 10 km: $\alpha(u,v,w) = (0.12, 0.17, 0.075)$, for λ_h = 50 km: $\alpha(u,v,w) = (0.095, 0.07, 0.065)$.

The regularization parameter for different gravity wave conditions

Recent observations of the gravity waves in the ionosphere (*Fritts et al.* [2015]) are reporting the presence of a wide variety of waves. They propagate at small (10 km) and long (planetary scale) horizontal wavelengths.

Gravity waves affect the numerical error of the neutral winds estimates by increasing the perturbation errors. Also, some parameters of the propagating gravity wave could be in the similar order magnitude of the experiment parameters at Arecibo, and that amplify the error due to instrumentation. For example, if the magnitude of the horizontal wavelength of a gravity wave is less or equal to the diameter (50 km at an altitude of 100 km) of the collecting area, the two possible samples per height are not truly representative of the oscillation of the wave. Analysis of the standard deviation of the estimated winds (Figure 2.8) shows that small horizontal wavelengths induce the largest errors. However, the standard deviation approaches an asymptotic stage as gravity waves reach dimensions of planetary scale.

Choosing a regularization parameter that optimizes the fitting between the model and data could help to minimize the error induced by the perturbations generated by the gravity waves. Analysis of the variation of the regularization parameter over an L-curve shows that smaller regularization parameters favor larger regularization errors with small perturbation errors. Also, larger regularization parameters propitiate large perturbation errors and small regularization errors (See Figure 2.6).

Figure 2.8 shows how the error changes according to α for different gravity wave parameters. Here, smaller regularization parameters produce the larger

discrepancies between the truth model and the estimated values for shorter wavelengths but small discrepancies for minimal perturbations (like wavelengths of planetary wave scale) seen in the first panel. Larger regularization parameters (like the latest panel) translates in an increase of the overall error so the penalty of the reduction of the errors induced by the data perturbations.

Recommendation about the regularization parameter

Choosing the correct regularization parameter generates the optimal fit for neutral winds. Using the L-curve criteria is not enough due to the presence of gravity wave perturbations in the MLT region. A new method using the minimal difference with a truth model is presented. This methodology shows that for gravity waves with short wavelengths, the optimal regularization parameter is large (of the order of $\alpha \approx 0.2$). For planetary waves, the optimal regularization parameter is smaller than $\alpha \approx 0.01$.

The authors recommend changing the α parameter accordingly to the characteristics of the suspected presence of a specific gravity wave family.

2.5.4 Monte Carlo error analysis

To study how the errors propagate through the iterative method, like the algorithm presented here, a Monte Carlo error analysis is used.

A Monte Carlo error analysis is performed after adding independent Gaussian random noise to the truth model. The noise is generated in accordance with the error estimates calculated for the ISR data and then added to the ion drifts.

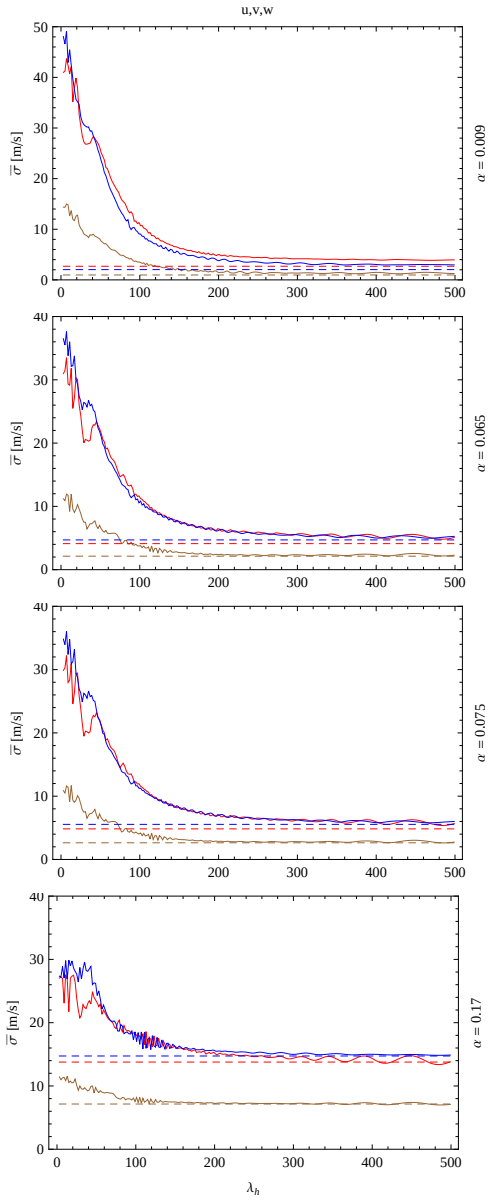

Figure 2.8: The total average of the standard deviation $\overline{\sigma}$ versus vertical wavelength λ_h for different α parameters. The standard deviation $\overline{\sigma}$ is the average in time and altitude of the standard deviation for the estimated winds when an specific horizontal wavelength of the theoretical gravity wave model was choosen. The α was chosen to minimize $\overline{\sigma}$ from the Figure 2.7. a) $\alpha = 0.009$, minimizes $\overline{\sigma}_v$ when no gravity waves. b) $\alpha = 0.065$, minimizes $\overline{\sigma}_w$ when gravity waves are present with $\lambda_h = 50$ km. c) $\alpha = 0.075$, minimizes $\overline{\sigma}_w$ when gravity waves are present with $\lambda_h = 10$ km. d) $\alpha = 0.17$, minimizes $\overline{\sigma}_v$ for the same conditions of c).

Then, the winds are estimated from a statistical ensemble of $10,000$ members, using a regularization parameter $\alpha = 0.075$.

The error propagation shown in the Figure 2.9 a) are 16 m/s for the horizontal east component, 9 m/s for the horizontal north component, and ≈ 2 m/s for the vertical component. The figure also shows that the error in the vertical component oscillates with a period similar to the used for the model of the gravity wave. The variation in the error for the horizontal components is minimal and does not seem to be strongly related to variations in the gravity wave or the Ekman model.

Error propagation with altitude is shown in Figure 2.9 b). The standard deviation is low except for higher altitudes, as shown by *Hysell et al.* [2014]. Panel c) shows the error for some instant of time. These plots show small errors for lower altitudes with small variations at the highest ranges.

The Monte Carlo error propagation method for the estimated neutral winds of a truth model shows minimal error variations in time and altitude with errors in order of magnitude of 10% of the maximum amplitude of the winds. The higher errors are found at higher altitudes where the gyro-to-collision frequency ratio is bigger than one, and the neutral particles are not totally dominating the dynamics of the region.

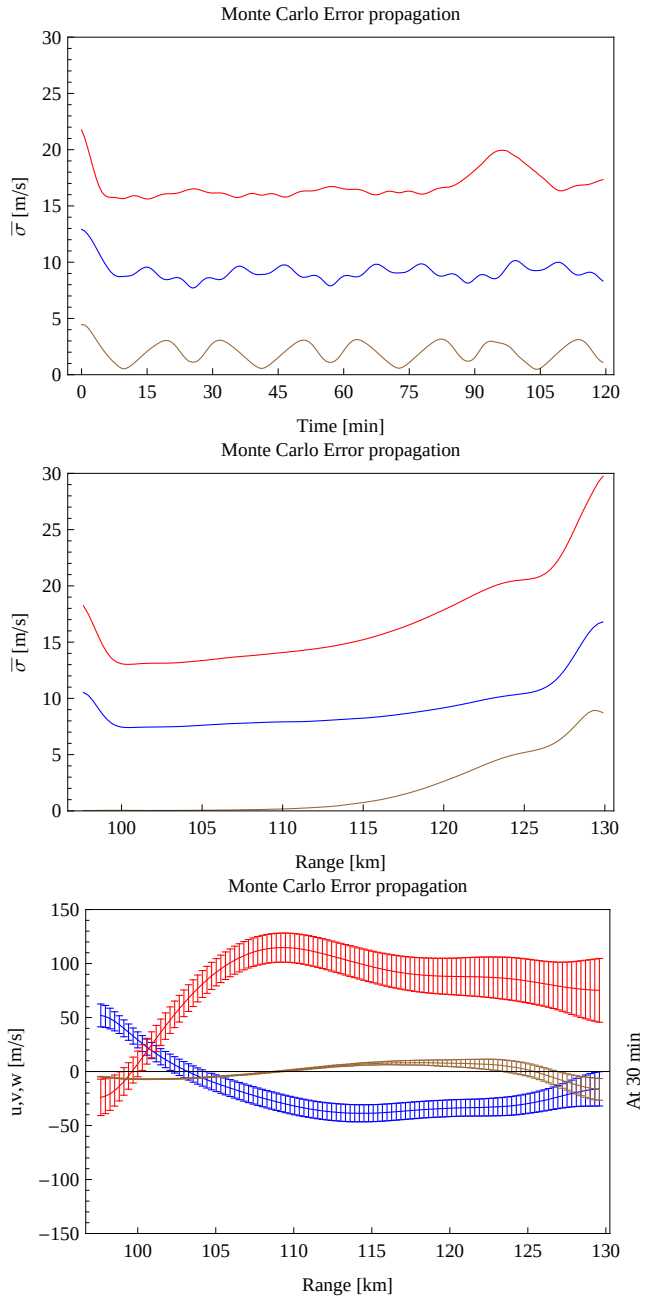

Figure 2.9: Monte Carlo analysis. The first panel averages the propagation of the standard deviation over all the altitudes. The second panel averages the standard deviation over 2h. The third panel is the Monte Carlo Errors at 30 min. The color convention is: $\overline{\sigma}(u)$ (red) , $\overline{\sigma}(v)$ (blue), $\overline{\sigma}(w)$ (yellow).

2.6 Neutral winds estimates from real data: example and Monte Carlo error analysis

The algorithm to estimate the neutral winds was applied to real data, collected during a World Day campaign at Arecibo, on November 4, 2013. Figure 2.10 shows the estimated winds for that day when the regularization parameter is $\alpha = 0.075$ (See caption for more details). The estimated winds feature the same general characteristics as rockets and lidar observations. The example presented corresponds to a normal day with smooth temperatures and electric field (panels e) and f)). The horizontal winds (panels g) and h)) have large amplitudes up to 150 m/s, with strongest shears at around 105 km. They depict what look like a diurnal and semidiurnal tidal effects of descending layers. The vertical winds (panel i)) are not as large, but they are not negligible. The vertical winds are in order of magnitude of 10 m/s, which agree with measurements from *Larsen and Meriwether* [2012].

A Monte Carlo analysis was performed. Independent Gaussian random noise of the order of the error estimates calculated for the ISR data was added $10,000$ times to the ion drifts used to estimate the neutral winds. The error propagation for the randomized estimated winds has similar characteristics to the error obtained with the truth model. The error in time (first panel of Figure 2.11) shows an oscillation in the three components of the winds, correlated with the Gregorian beam swinging. In the zonal component, the swing creates an error of 2 m/s, in the meridional of 1 m/s and in the vertical of 2.5 m/s. These values are less than the error propagation associated with the height dependence of the system for the horizontal winds. For the vertical wind, the error is

slightly bigger. An explanation for the increase in the error values could be the way the winds are estimated since the algorithm only uses the measurements from the line of feed (pointing at zenith) and omits the Gregorian data when calculating the vertical winds. Also, the vertical winds error increases by 2 m/s before sunrise or after sunset, when the ionization is lower.

The error propagation varies with height since lower altitudes are dominated by neutral collisions and higher altitudes are dominated by magnetized particles. Panel b) in Figure 2.11 shows that, for lower altitudes, the error is of the order (7, 13, and 1) m/s for the zonal, meridional and vertical components of the neutral winds. For higher altitudes, the error is (9, more than 20, and 5) m/s. In the collision dominated region, the method estimated the winds with errors smaller than 10% of the maximum amplitude.

2.7 Conclusions

The Arecibo upgrade allowed performing experiments with dual beams and novel codes ideally designed to estimate the drifts in the *E* layer. These facts made possible experiments that could not be performed during the AIDA campaign in 1989.

Hysell et al. [2014] presented a new methodology to estimate the parameters needed to obtain the three components of the neutral winds in the MLT region. Using the information for the whole range of the ionosphere, from the lower *E* to the *F* layer, the methodology estimates the electric fields and composition as well as the three components of the neutral winds in altitudes between $97 - 130$ km.

Following the lessons from the AIDA campaign, the methodology was tested for idealized waves, including sinusoidal variations or gravity waves on top of the expected rotational winds. Possible gravity waves of the order of planetary scale ($\lambda \approx 500km$) do not affect the reconstruction of the winds. However, winds contaminated by gravity waves of the order of the dimensions of the Arecibo collecting area ($\lambda < 50km$) induce errors. Those errors could be minimized by the use of an optimal regularization parameter for the suspected gravity wave.

Monte Carlo error analysis found that the algorithm reconstructs daytime horizontal neutral winds with errors less than 10% of the maximum amplitude, but increasing with altitude. This new methodology expands the capabilities of the ISR at Arecibo, allowing us to monitor the neutral winds at *E*-region heights.

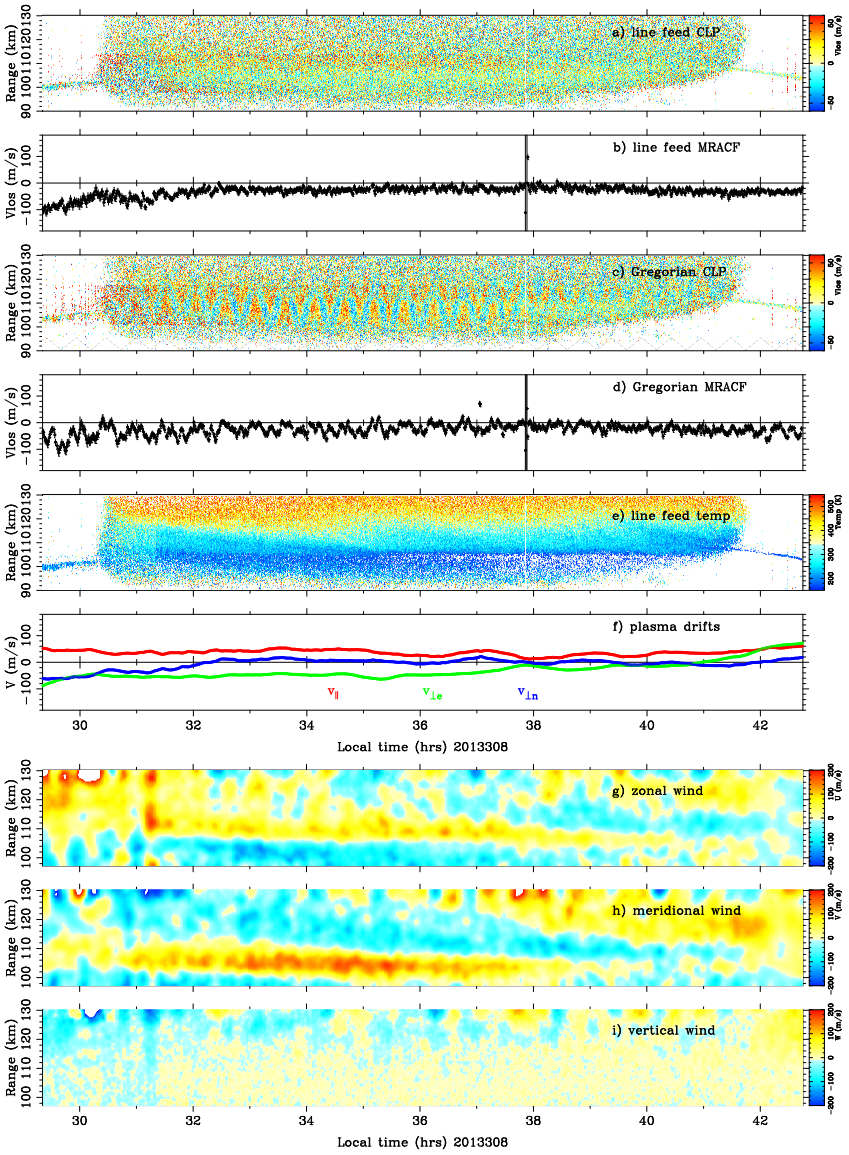

Figure 2.10: Winds Estimations for November 4, 2013. The panels a) and c) corresponds to the ion drift data for the *E* region, collected with Arecibo. The panels b) and d) corresponds to the average ion drifts for the *F* layer. Panel e) is the estimated temperatures. Panel f) have the three components of the electric field. Panel g) to i) are the estimated zonal, meridional and vertical neutral winds for the MLT region.

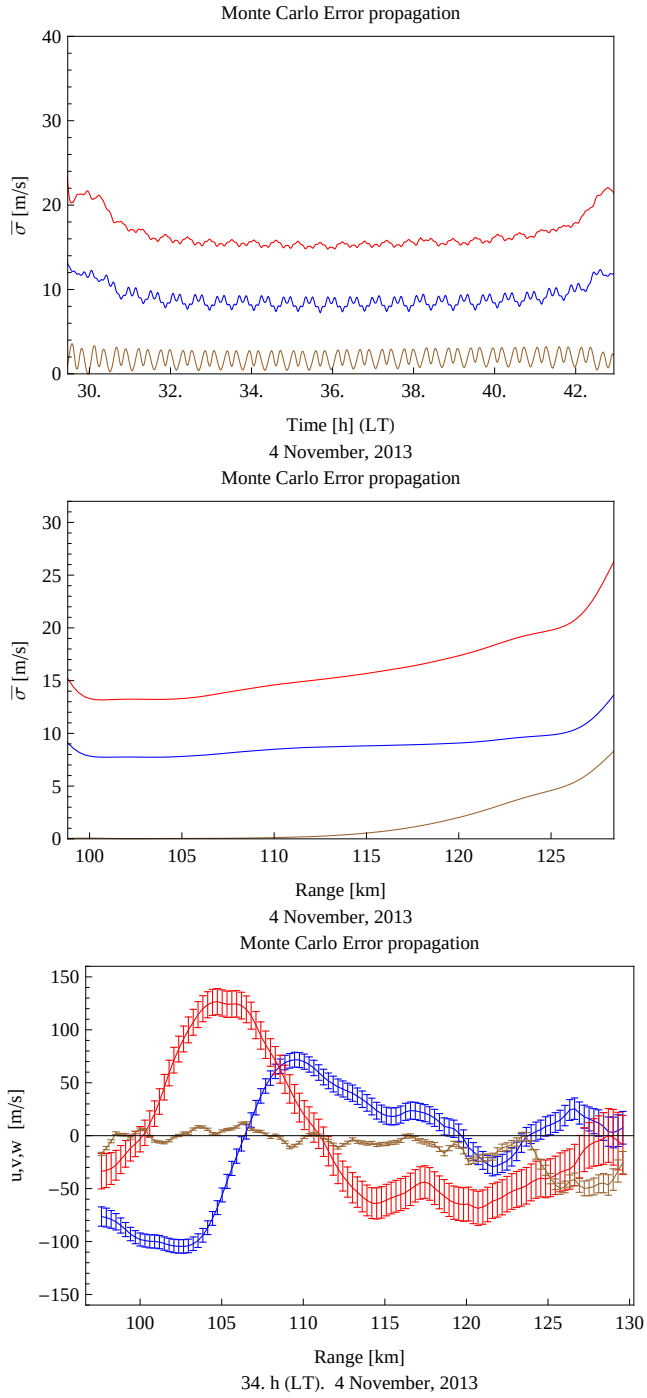

Figure 2.11: Monte Carlo analysis for real data. The first panel averages the propagation of the standard deviation over all the altitudes. For the day, the sunrise is at 30h and sunset at 42h (LT). The second panel averages the standard deviation over the day. The third panel corresponds to the instant of time at 34h (LT). The color convection is: $\overline{\sigma}(u)$ (red) , $\overline{\sigma}(v)$ (blue), $\overline{\sigma}(w)$ (yellow).

3

NEUTRAL WINDS ESTIMATES - EXAMPLES

"There is no drop of water in the ocean, not even in the deepest parts of the abyss, that does not know and respond to the mysterious forces that create the tide."

– Rachel Carson

The neutral winds estimated for the Arecibo World Day campaigns performed during 2013 and 2014 are perhaps the first set of data available to study daytime MLT irregularities between 95 and 130 km altitude. Other instruments and techniques have some technical limitations. For example, most lidars measurements operate during the night and reach heights just up to about 110 km. Also, rocket campaigns observations are confined to the duration of the flight. The fallen spheres technique is limited in altitude, too. Satellite observations require 60 days to reconstruct the neutral winds from one day. The neutral winds along with temperatures and electric fields estimates presented here give us the best information to diagnose the MLT. This chapter also compares the results with measurements from other instruments and models for the appropriate altitude ranges or time.

3.1 Introduction

The three components of the neutral winds at *E*-layer heights are reconstructed using the numerical method described by *Hysell et al.* [2014] and explained in Chapter 1. The neutral winds are estimated during the daytime when the ionization is strong and when no magnetic storms are underway. An equipoten-

tial **B**-field line is assumed, resulting in a height-invariant electric field. The methodology solves for the appropriate daytime composition to then estimate the neutral winds for three World Day campaigns performed during 2013-2014 with a total of six complete daytime data sets.

Neutral winds in the MLT-region has been characterized using remote sensing and in-situ observations. Chemical-release wind measurements from more than 400 sounding rocket campaigns compiled by *Larsen* [2002] show strong shears in the zonal and meridional wind components, with peak velocities exceeding $\pm$100 m/s at about 105 km altitude and wind shears larger below than above the winds peak. The wind measurements also show small velocities for altitudes below about 85 km. Pictures of the TMA chemical releases published by *Larsen et al.* [2005] show evidence of the neutral wind rotational behavior. Lidar observations like those from the Colorado State University (CSU) Na lidar in *Yue et al.* [2010] show neutral wind peak values around 100 km altitude with shears larger than 40 m/s/km at heights above about 95 km. Lidar and rocket measurements have similar peak and shear values. However, the altitude of the peak is always lower in the lidar measurements. It seems that the difference between the techniques is the reason for the disagreement. The chemical tracer measurement is almost instantaneous at all heights since the experiment time lasts less than about 10 min. The lidar wind meanwhile is averaged over a time interval which can be up to 1h (*Yue et al.* [2010]). The winds in the MLT-region are created by long time tidal effects and planetary waves as well as short time local waves like gravity waves. The sampling of the two techniques could correspond to two different conditions in the atmosphere. However, long trends of winds obtained with chemical-tracer and lidar techniques agree regarding the magnitude and the vertical wind structure (*Larsen et al.* [2003]).

The characteristics of the neutral winds suggest that irregularities in the mesosphere and lower thermosphere (MLT) region can be generated in a similar way as in the lower layers of the atmosphere. The variety of ion dynamics measured in the MLT region with incoherent scatters could be the result of neutral atmosphere activity. *Larsen* [2000b], *Larsen et al.* [2004] and recently *Hysell et al.* [2012] have been proposing that nighttime coherent scatter echoes and rolls, observed with Arecibo and St. Croix coherent radar, are products of the shear instability that produces billows of the Kelvin-Helmholtz type. However, observations from the TOMEX rocket campaign with simultaneous Na lidar observations at the Starfire optical range suggest other factors besides shear instability produce irregularities in the mesospheric and lower thermosphere. *Liu et al.* [2002]) observed that convective instability was likely to occur in the presence of large negative temperature gradients at lower altitudes. This phenomenon is called "heating from below" by *Chandrasekhar* [1961]. Lidar temperatures for heights below 105 km vary between 150 ^{o}K and 230 ^{o}K as shown by *Friedman and Chu* [2007]. MSIS temperatures range from about 180 ^{o}K at 90 km to about 500 ^{o}K at 130 km with a minimum value at about 98 km. Observations performed by *Gardner et al.* [2002] revealed the presence of convective regions inside an *E* layer. *Dickinson* [1973] and *Molemaker et al.* [2005] predicted baroclinic instabilities in the mesosphere, but little work has been done to detect this in the lower thermosphere.

The parameters that characterize local stability are the Brunt-Vaisäla frequency (N^2) and the Richardson number (R_i) which are determined by temperature (T) and shear (S) variation:

$$N^2 = \frac{g}{T}\left(\frac{dT}{dz} + \frac{g}{c_p}\right) \tag{3.1}$$

$$R_i = \frac{N^2}{S^2} \tag{3.2}$$

where g is gravity at the appropriate height, c_p is the atmospheric specific heat and z is the vertical direction.

Many instabilities can be identified by these parameters. It is easy to visualize them in the R_i dimension. When the Brunt-Vaisäla frequency is negative ($R_i < 0$) the atmosphere is convectively unstable (*Marshall and Schott* [1999] and *Peixóto and Oort* [1984]). Kelvin-Helmholtz instabilities can develop when $0 < R_i < 1/4$ (*Miles* [1961] and *Howard* [1961]). Baroclinic instabilities occur for $R_i \to \infty$ (*Charney* [1947], *Eady* [1949], *Green* [1960]), usually when big temperature gradients are present for surfaces of constant density. The criteria are necessary but not sufficient conditions for the development of instabilities.

The present chapter presents some examples of neutral wind estimates based on Arecibo data. Some days are characterized by negative temperature gradients that could induce negative Brunt-Vaisála frequency. Also, there are data sets with large shears that could indicate the formation of billows due to dynamic instability. In some cases, sharp temperature gradients are present which could lead to baroclinic instability formation. The following chapters will analyze each of these instabilities. Meanwhile, some illustrative examples will be shown here.

3.2 Examples

The ISR Arecibo data presented here correspond to six days from three different campaigns performed between 2013 and 2014. Figures 3.1 to 3.4 correspond to campaigns performed in 2013 and Figures 3.5 to 3.7 correspond to a selection from the 2014 campaigns.

To estimate the neutral winds, temperatures are calculated by fitting the backscatter power spectrum to the autocorrelation function and assuming thermal equilibrium ($T_n = T_e = T_i$). The temperatures obtained (panel e) in figures 3.1 to 3.7) vary from about 200^oK to more than 500^oK. At about 95 km, the temperature is near to 400 ^{o} K, decreasing to a minimum near 98 km. This feature seems to agree with MSIS model. However, the ISR values at 95 km are slightly higher than both MSIS and the potassium Doppler lidar temperatures obtained by *Friedman and Chu* [2007]. For these altitudes, the ISR temperature error is high. The general vertical temperature gradient between 100 km and 130 km is about 10^oK/km and agrees with the values generated by MSIS-90. A significant difference with MSIS temperatures is present in some ISR temperature profiles, where the temperature gradient is not uniform (see temperatures in Figure 3.7), inducing changes in the Brunt-Väisälä frequency and perhaps creating the conditions for convective instability as will be explored in Chapter 4.

Using the ISR temperatures and ion drifts, neutral winds are estimated as described in Chapter 1. The winds shown here are characterized by features similar to the winds observed with chemical releases and lidars techniques. The peaks in the horizontal wind change from day to day but reach a maximum at altitudes below 120 km with magnitudes exceeding 100 m/s and in some

cases reaching 200 m/s. The biggest vertical shears for the horizontal wins are observed at altitudes below the wind peaks, reaching up to 40 m/s/km. Hodographs for the horizontal winds show rotational behavior (see figures in Chapter 6). Smaller vertical velocities are found. Although usually rockets and liars do not measure the vertical component, small vertical velocities are expected under the following reasoning:

$$w = H\left(\frac{\partial u}{\partial x} + \frac{\partial v}{\partial y}\right) \tag{3.3}$$

This is the incompressibility condition with $\partial w/\partial z = w/H$, where w is the vertical velocity, H is the scale height and u and v are the zonal and meridional horizontal winds, respectively.

There is a clear formation of two horizontal velocity layers. The peaks of these layers usually descend slowly at different rates. The lower layer starts at about 110 km altitude at sunrise and descends at a rate of $\sim$ 1 km/h, and is observed more clearly in the meridional winds. This layer is associated with a diurnal S(1,1) tide. The upper layer is observed mostly during the afternoon which could indicate that starts at altitudes higher than 130 km at sunrise, descending at $\sim$ 4 km/h. This layer is associated with a semidiurnal tidal wind. *Haldoupis* [2011a] showed that diurnal S(1,1) tidal wind with vertical wavelength $\lambda_z = 28$ km and semidiurnal S(2,6) zonal tidal wind with $\lambda_z = 33$ km explain the formation of the descending ion layers observed by the Arecibo ISR. Winds obtained by the Fabry-Perot Doppler interferometer carried by TIMED satellite (TIDI) see a similar stratification of the winds (*Killeen et al.* [2006]) with amplitude values in the same order of magnitude. However, in the TIDI measurements, the semidiurnal tidal effects are seen more clearly in the zonal winds

and the diurnal tidal effects in the meridional winds.

3.3 Discussion

The neutral wind estimates presented in this chapter agree qualitatively with previous nighttime observations made with the chemical release and lidar techniques. Peak and shear values are in the same range as those observed with rockets and lidars. The altitudes for the peaks and the evolving shapes found here agree mostly with the chemical release data. The descending patterns agree with diurnal and semidiurnal tides according to calculations for ion descending layers formed due to a wind-shear mechanism.

Vertical temperature values and gradients agree with lidar and MSIS model values except at low altitudes. At heights below 100 km, the temperature error is high. For the calculations in the following chapters, only temperatures with small errors should be considered. For altitudes greater than 100 km, the high resolution of the data shows evidence of changes in temperature gradient not considered before during strong daytime ionization. Also, the vertical winds are structured in order of 10 m/s.

The neutral wind, electric field, and temperature estimates are useful tools for understanding the dynamics of the MLT region. The variations in the observed features suggest the presence of different regimes of the Richardson number, the main indicator of the necessary conditions for the development of neutral irregularities. A deeper study of each of these irregularities is the subject chapters to follow.

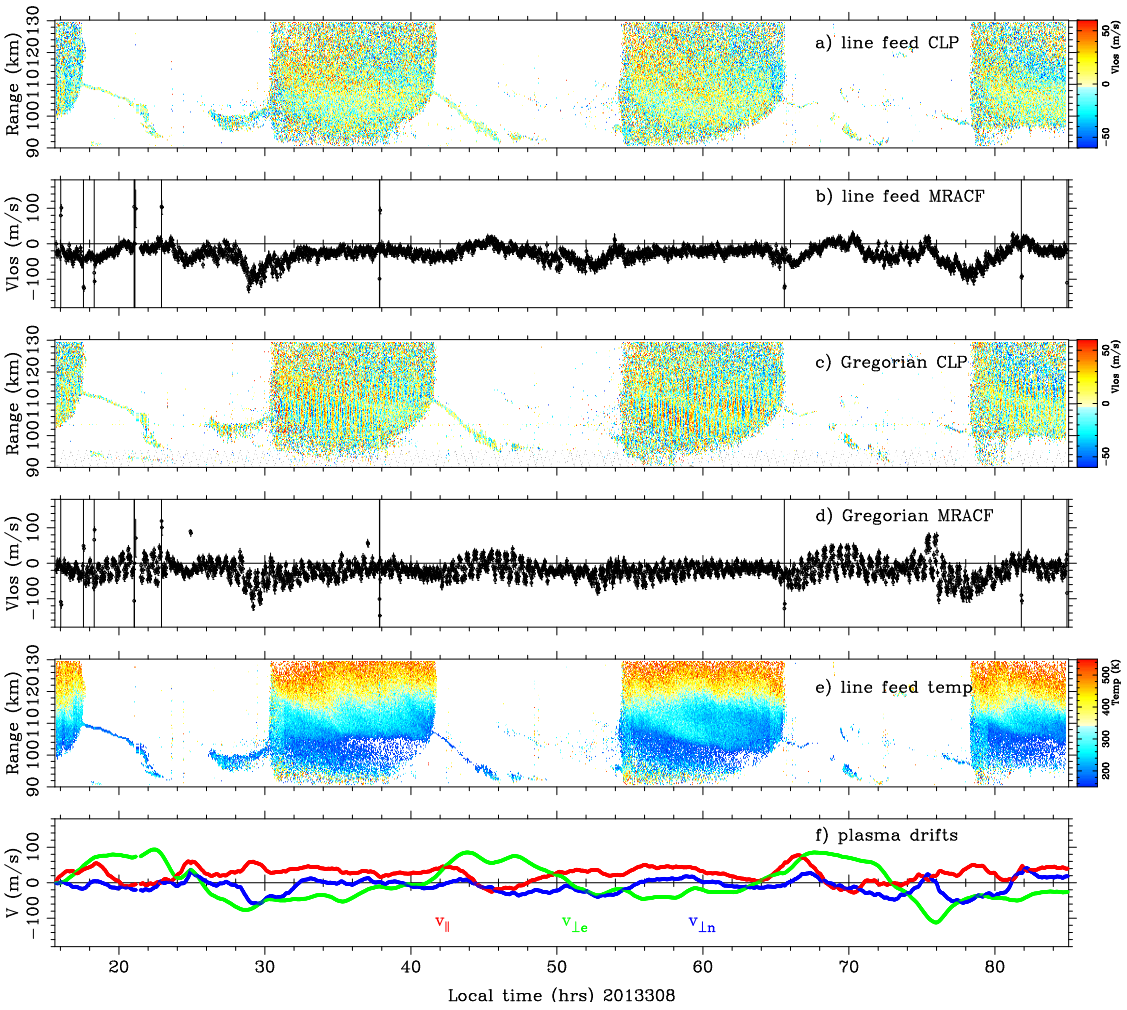

Figure 3.1: ISR Arecibo observations of three days starting on November 4/2013. For every panel, the vertical axes extends from 90 to 130 km and the horizontal axe represents Arecibo local time. Panels a) and c) correspond to the *E* region ion drifts estimated from the CLP collected data from the two beams (line feed and Gregorian). The line feed was pointing to zenith (vertical), and the Gregorian was rotating in azimuth at 15 deg zenith angle at a rate of approximately 15 min per 360 deg. Panels b) and d) plot the height-integrated *F* region line-of-sight ion drifts calculated from the MRACF data from the two beams. Panel e) shows the temperature profiles, derived from fitting the autocorrelation function of the CLP data from the vertical beam, assuming thermal equilibrium. Panel f) shows the plasma drifts for the *F* layer which are an indication of the **E**-field in the perpendicular-to-**B** direction.

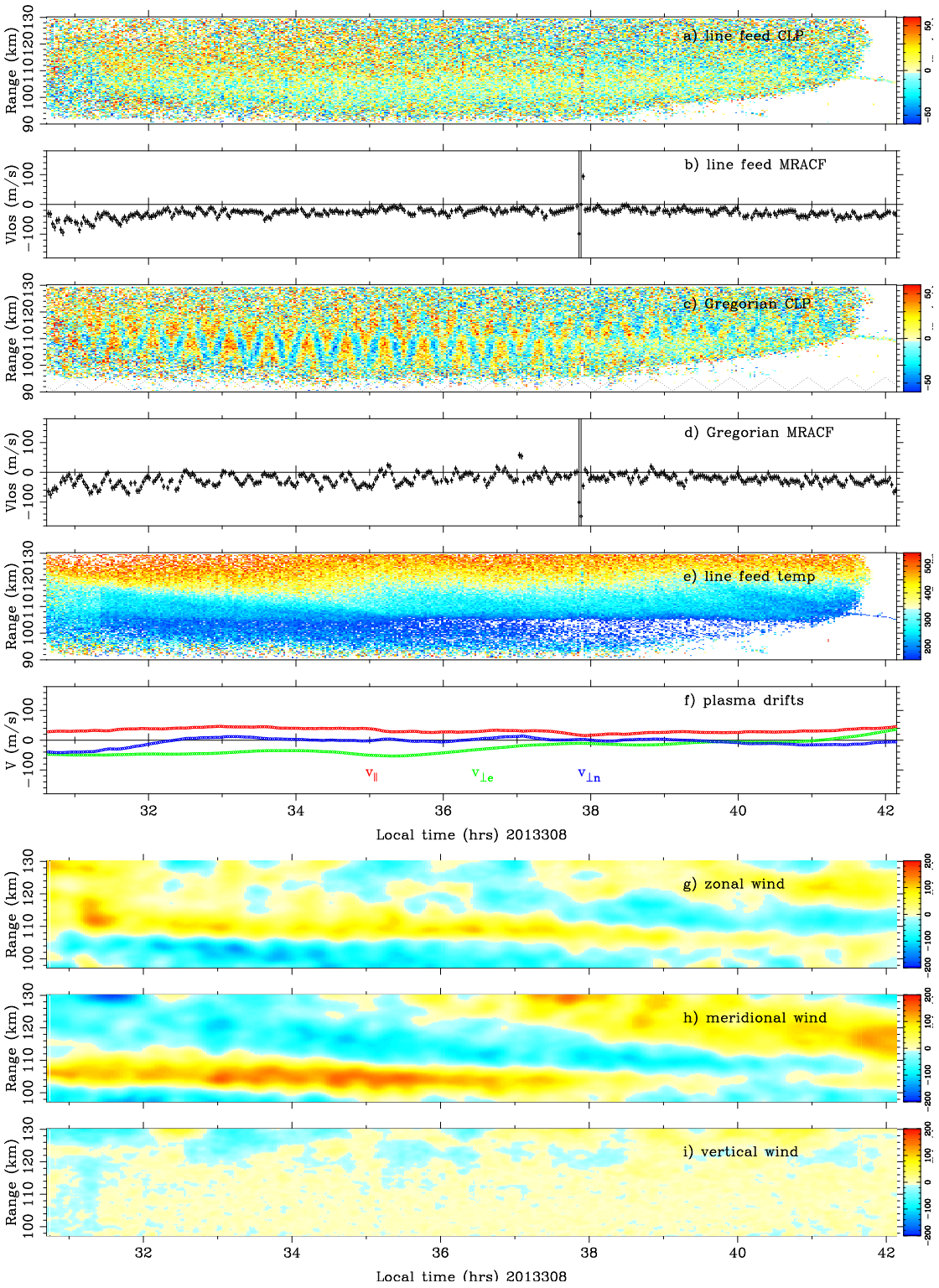

Figure 3.2: Arecibo ISR observations from November 4/2013, and daytime neutral winds estimates (panel g) zonal, h) meridional and i) vertical wind). Panels a) to f) are described in Figure 3.1.

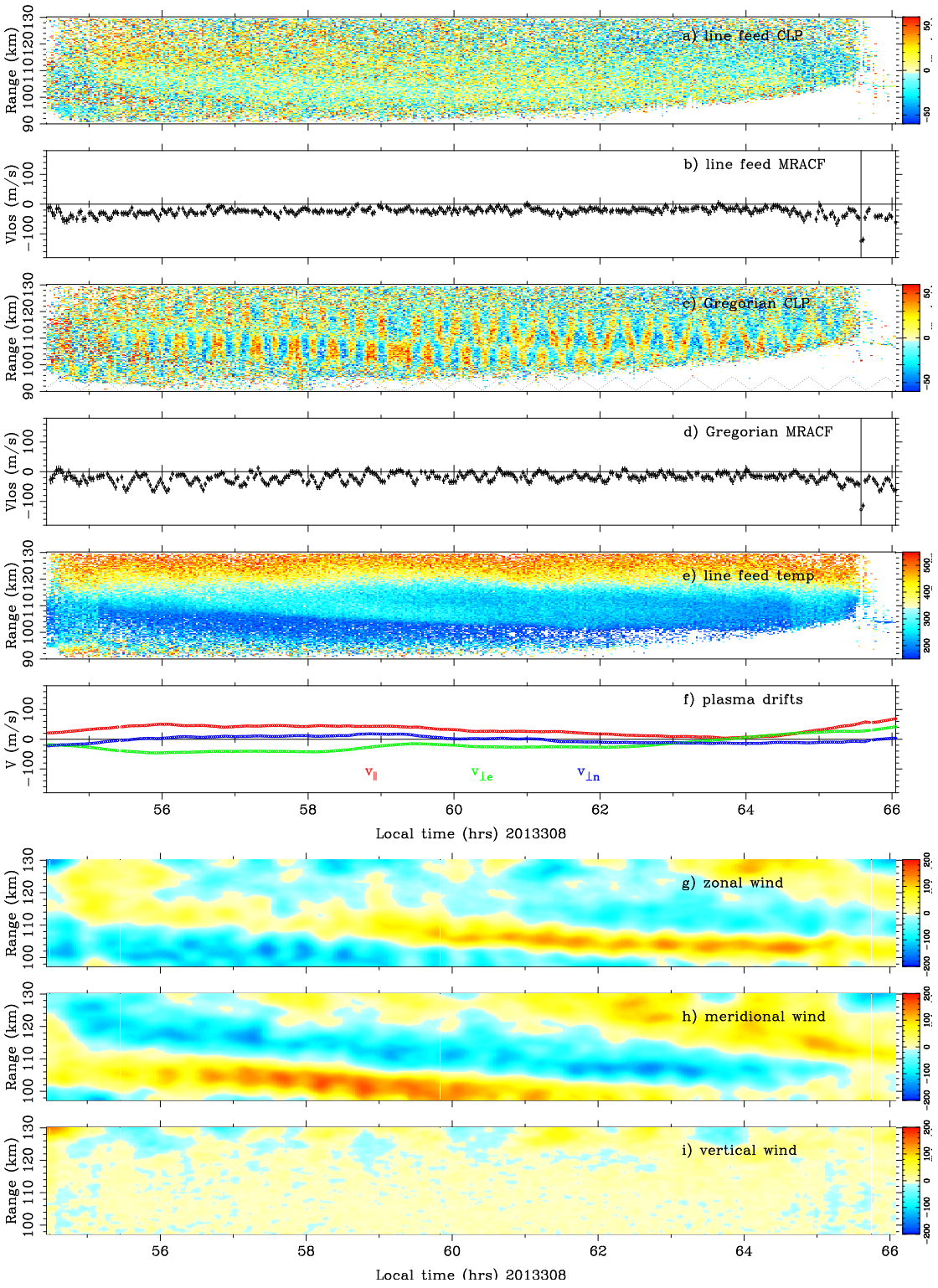

Figure 3.3: Arecibo ISR observations and daytime neutral winds estimates for November 5/2013. Panel descriptions are detailed in Figure 3.1

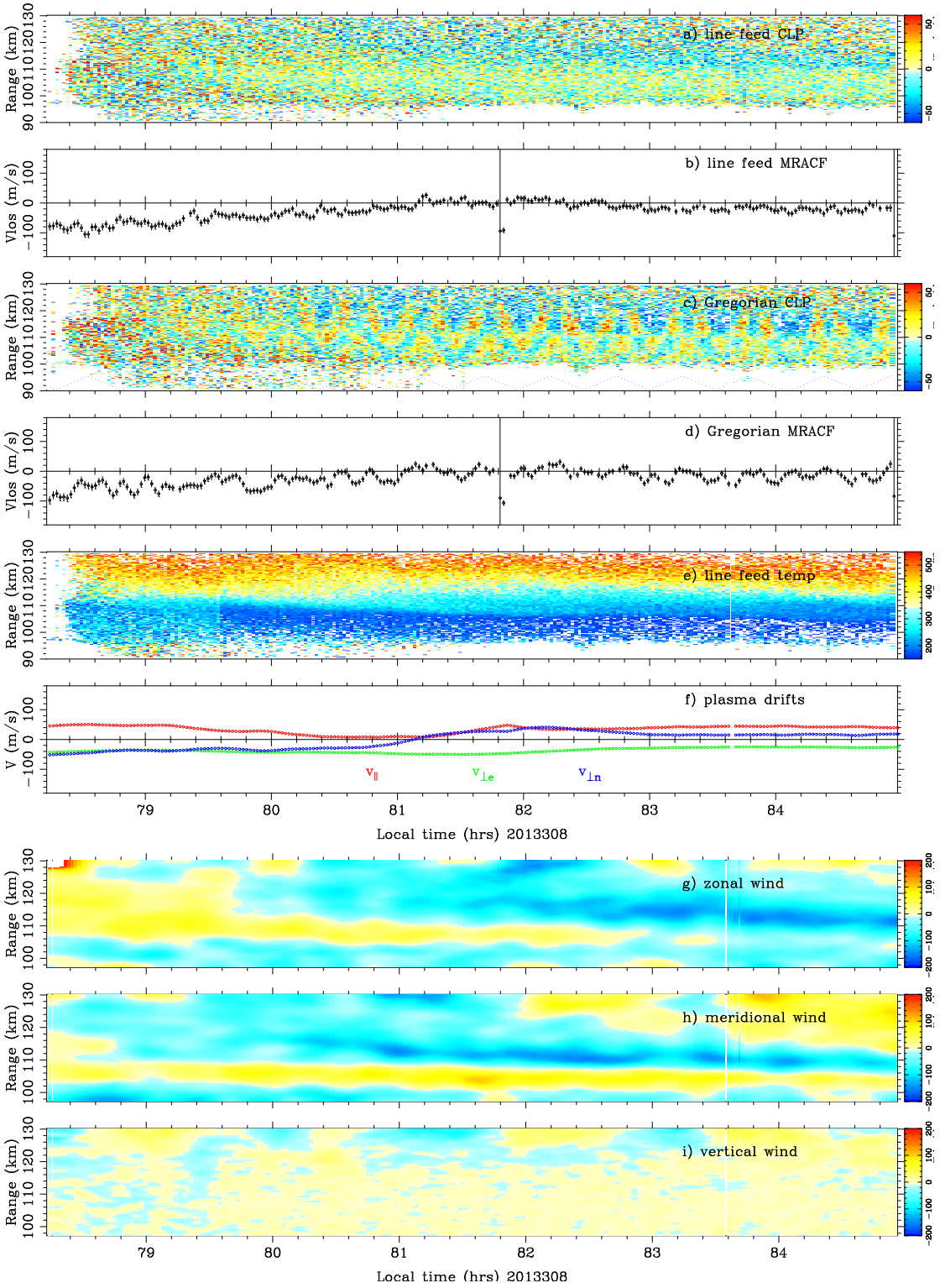

Figure 3.4: Arecibo ISR observations and daytime neutral winds estimates for November 6/2013. Panel descriptions are detailed in Figure 3.1

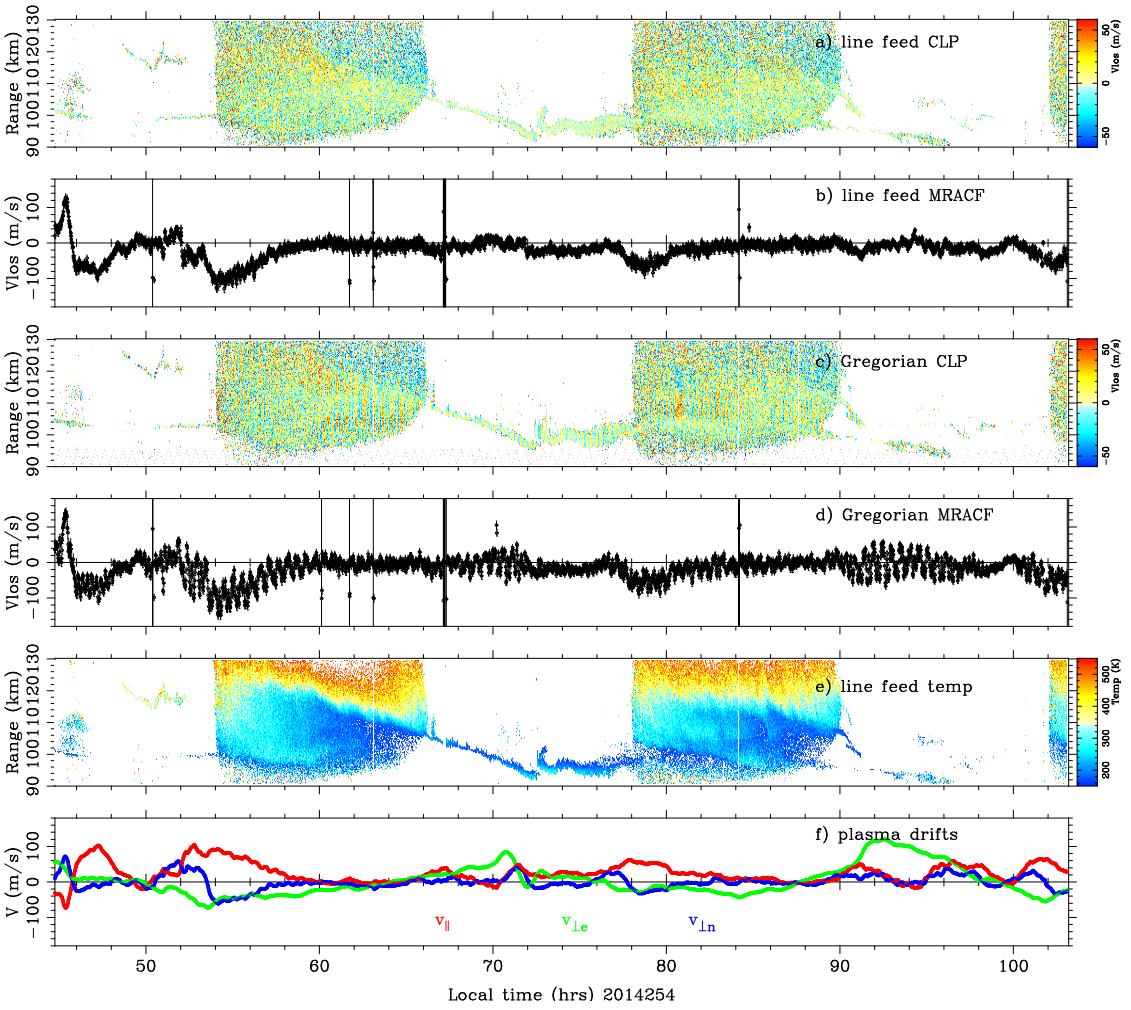

Figure 3.5: Arecibo ISR observations of two and a half days starting on September 11/2014. Panel descriptions are detailed in Figure 3.1

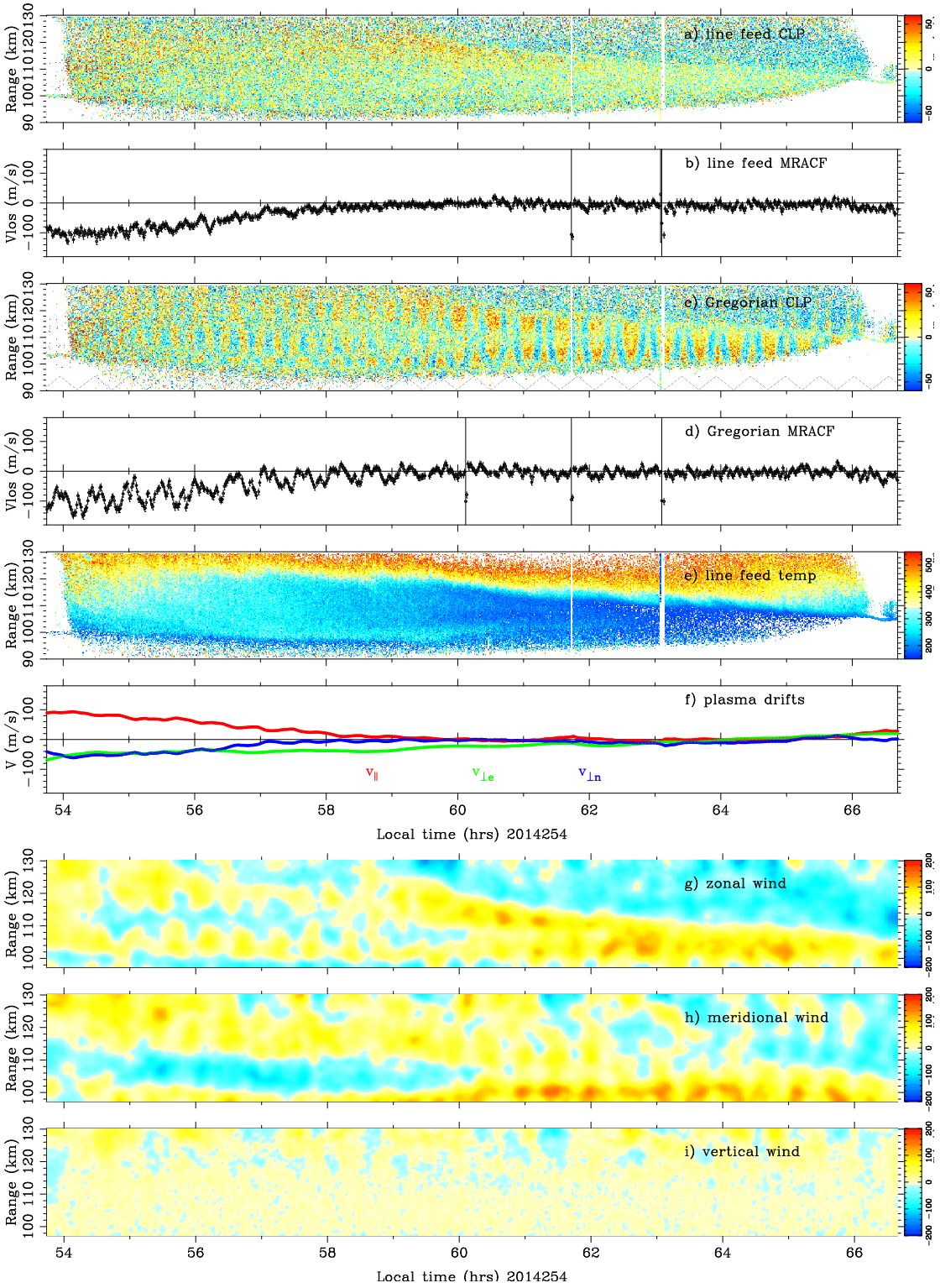

Figure 3.6: Arecibo ISR observations and daytime neutral winds estimates for September 11/2014. Panel descriptions are detailed in Figure 3.1.

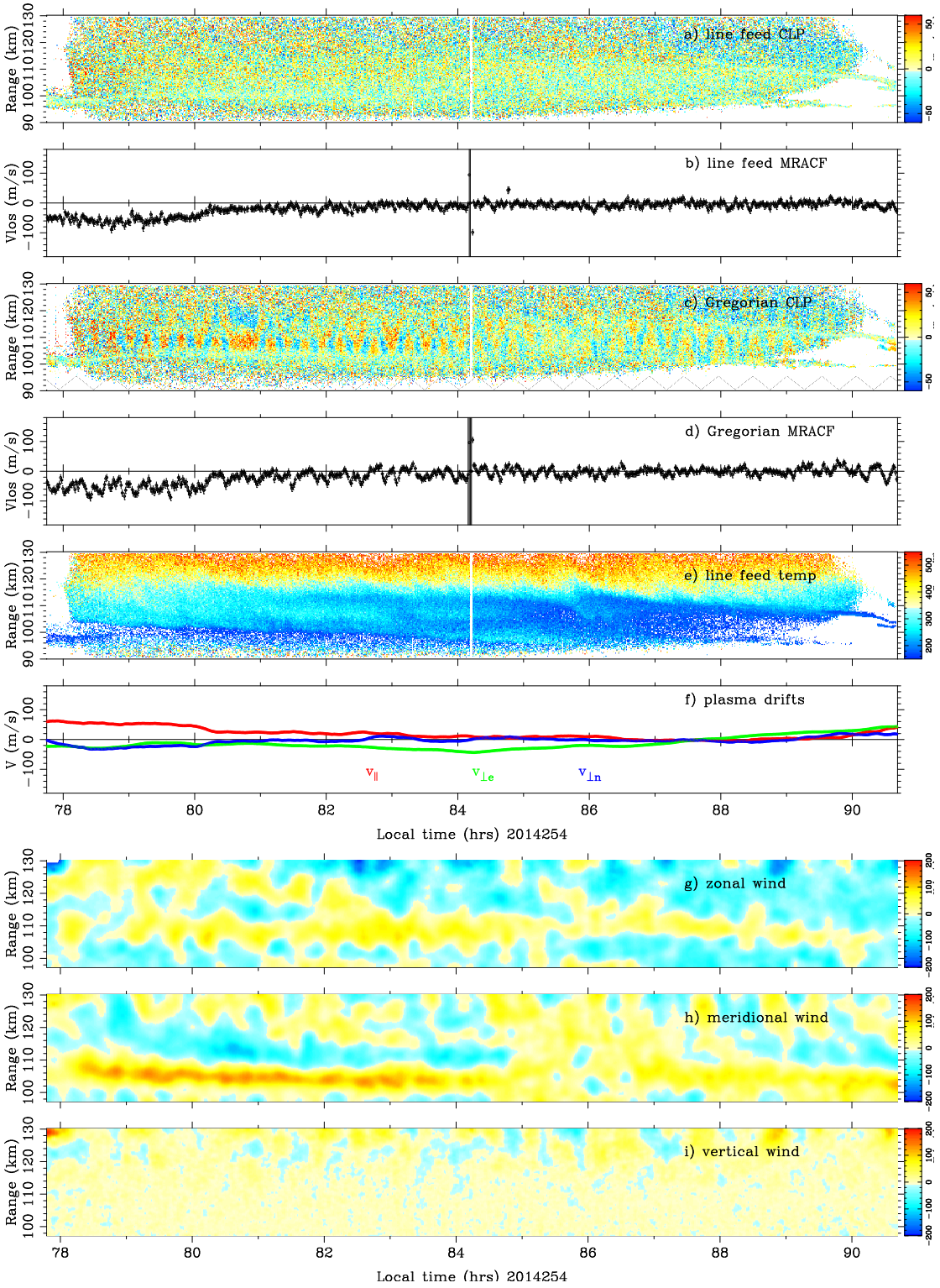

Figure 3.7: Arecibo ISR observations and daytime neutral winds estimates September 12/2014. Panel descriptions are detailed in Figure 3.1

4

CONVECTIVE INSTABILITY

"The Eastern sky was all grey blue - bunches of clouds - different kinds of clouds - sticking around everywhere and the whole thing - lit up - first in one place - then in another with flashes of lightning - sometimes just sheet lightning - and sometimes sheet lightning with a sharp bright zigzag flashing across it."

– Georgia O'Keeffe

Convective instability requires high inverse temperatures that can destabilize the natural oscillations of the atmosphere. At equilibrium the mass parcels oscillate but when the irregularity is developed the mass ascends without limits. These irregularities in the MLT can be one possible cause for the breakage of the ion layers in the *E* region. Negative buoyancy frequencies or negative Richardson numbers characterizes the convective events. This chapter is the first one of a series of analyses about particular irregularities, organized from negative to positive Richardson numbers.

4.1 Introduction

Static instability is the source of convective patterns when the time scale of the motion is short compared to changes in composition or heat content. The patterns are produced by the exchange of two parcels of fluid at different elevations. A parcel finds stable equilibrium when it is displaced upward because it loses "weight," but gravity forces it to descend to its original position. The equilibrium is unstable when a parcel is lighter than the surrounding environ-

ment, and gravity is insufficient to force descent. This instability is known as the Bèrnard problem (Bèrnard performed the earliest experiments in 1900 to demonstrate the onset of thermal instability in fluids heated from below), although the phenomenon of thermal convection has been studied by Count Rumford (1797) and James Thomson (1882). *Chandrasekhar* [1961] summarized the theory from a general fluid dynamics point of view.

The thermal patterns explain convective weather in tropical zones produced by cold air on top of warm air. *Brunt* [1927] was perhaps the first to relate the buoyancy frequency with oscillations in the atmosphere. Forty years later, *Lorenz* [1967] gave the fundamentals for understanding how the small-scale convective motions stabilize the stratified atmosphere. *Peixóto and Oort* [1984] studied temperature changes with height and related the decrease of temperature with atmospheric instabilities. *Gill* [1982] contextualize the theoretical fluids approach to include atmospheric variations and to finally connect the instabilities with negative buoyancy or Brunt Väisälä frequency values.

Inverted layers in the MLT region could trigger static instabilities due to the presence of negative temperature gradients larger than the adiabatic lapse rate. These instabilities are indicated by the presence of negative buoyancy frequency. *Meriwether and Gerrard* [2004] characterizes low-latitude to mid-latitude "double" mesosphere inversion layers (MILs) using Na lidar systems operating at night. One of the possible formation mechanisms of the upper MIL layer is nonlinear gravity wave-tidal interactions. The gravity-tidal MILs reach a maximum temperature between $85 - 95$ km with amplitudes of $20 - 50$ K over the background temperature. *Larsen et al.* [2004], *Liu et al.* [2004] and references therein showed overturning structures between 90 - 100 km during the Tur-

bulent Oxygen Mixing Experiment (TOMEX) campaign performed in October 2000. The overturning structures were observed with the University of Illinois lidar located at the Starfire Optical Range (SOR) in New Mexico, and the temperature enhancements were measured with a rocket launched from White Sands Missile Range at about 10 UT (LT + 6 h). At the moment of roll development, there were lower layers with negative Brunt-Väisälä frequency patches. *Gardner et al.* [2002] also used data from SOR to show large temperature perturbations due to a semidiurnal tide, producing statically unstable regions. *Mlynczak et al.* [2001] used falling sphere measurements from Super-Loki rockets to explains the temperature enhancement of the "upper" MIL as being due to the increase in ozone during the day. The altitude of the ozone-upper MIL layer, though, is lower than 90 km. It seems that the correlation between the temperature enhancement and the ozone concentration is a coincidence and not an indication of thermal dependence of the chemical kinetics (*Meriwether and Gerrard* [2004]).

MILs have been observed with Na lidars operating at night. Since the density of these neutral layers is not related to solar variations, it is possible that MILs are present also during daytime. The region where the "upper" lidar MILs have been observed corresponds to a range of altitudes between $90 - 100$ km. However, the lidar observations are restricted to heights below 105 km. Similar inverted temperature profiles could be observed at higher altitudes with other remote or in-situ instruments.

From very high altitudes down to the mesopause (~ 90 km), the neutral particles absorb UV and EUV radiation from the sun. This process increases the temperature and creates the plasma due to the ionization of the neutral atmosphere during radiation absorption. It is assumed that the neutral density de-

cays uniformly with altitude. However, when this density stratification breaks, higher neutral density zones are generated, and inverse temperature profiles can be observed. Gravity wave-tidal interactions, irregularities produced by the nature of the neutral winds in the MLT region, as well as meteor ablation, could be the reason for these changes in density. Na density layers are routinely observed by modern lidars (*Li et al.* [2009]). Examples of a non-uniform Na density layers are shown by the density maps obtained with the large zenith telescope (LZT) lidar in Canada (*Pfrommer et al.* [2009]).

During the World Day campaigns, MLT inverse temperature profiles are frequently observed during the day with the Arecibo ISR (Figures 3.1-3.7). To estimate Arecibo temperature profiles, quasi-thermal equilibrium is assumed. The inverse temperature profiles indicates that highly convective conditions can be due to "heating from below" (as stated by *Chandrasekhar* [1961]). Additionally, this region often shows high neutral winds with maximum shear peaks between 100 - 115 km (*Larsen* [2002]). The convective instability (driven by temperature gradients) would induce the transition to dynamic instability (driven by wind shear) at higher altitudes. The possibility of convective layers at the bottom of the *E*-region during the day is investigated in this chapter. The theoretical framework and observations are presented.

4.2 Natural oscillations in the atmosphere - Theory

The MLT ion motion follows neutral motion in large part at altitudes of interest, so we explore neutral behavior for clues to what is happening. The dynamics of the neutral atmosphere are studied using the standard fluid equations as

follows.

4.2.1 The buoyancy fluid model

The MLT region consists of electrons, ions, and neutral particles. The neutral particles in the ionosphere behave as a Newtonian fluid with varying density (ρ) and temperature (T). Assuming that there are no production or losses and that the mass is conserved, the *continuity equation* is used:

$$\frac{D\rho}{Dt} = -\nabla \cdot (\rho \mathsf{u}) \tag{4.1}$$

The pressure in the MLT region is very small, and the density changes are independent of pressure effects. The density variations in a parcel are only temperature dependent. However, large shear velocities are observed in the MLT region. For this analysis, the Boussinesq approximation is used, neglecting density variations except when they could cancel the gravitational force. This results in $D\rho/Dt \sim 0$ which leads to the incompressibility condition:

$$\nabla \cdot \mathsf{u} = 0 \tag{4.2}$$

The equation of motion for Newtonian fluids is known as the *Navier-Stokes* equation. For incompressible fluids, the Navier-Stokes equation reduces to what is known as the *momentum equation*:

$$\frac{D\mathsf{u}}{Dt} = -2\Omega \times \mathsf{u} - \frac{1}{\rho}\nabla p - g + \nu\nabla^2\mathsf{u} \tag{4.3}$$

where $\frac{Da}{Dt} = \frac{\partial a}{\partial t} + \mathsf{u} \cdot \nabla a$ is the advective derivative. The vector field $\mathsf{u} = (u, v, w)$ represents the three components of the neutral wind (east, north, vertical) in the (x, y, z) directions, respectively. The Coriolis force is governed by the angular velocity of the Earth, Ω. A viscous fluid resists the deformation of shear stress. The measure of that resistance per unit density is called kinematic viscosity ν. The pressure gradient depends on the pressure-density relationship as stated by the *equation of state* for ideal gasses

$$p = \rho RT \tag{4.4}$$

moreover, the gravity term is related with pressure gradients as indicated by the *hydrostatic equation*

$$\frac{dp_o}{dz} = -g\rho_o \tag{4.5}$$

where gravity, g, is in the z direction. The equilibrium or "background" state of density and pressure are $\rho_o(z)$ and $p_o(z)$. The gas constant is R, and the absolute temperature is T.

The perturbed density and pressure are defined by $\rho(z,t) = \rho_o(z) + \rho'(t)$ and $p(z,t) = p_o(z) + p'(t)$ which depart from the equilibrium density ($\rho_o(z)$)

and pressure ($p_o(z)$) states in perturbation quantities (ρ') and (p'), respectively. Assuming these perturbations, the density term in the incompressibility condition $D\rho/Dt = 0$ becomes:

$$\frac{\partial}{\partial t}(\rho_o + \rho') + u\frac{\partial}{\partial x}(\rho_o + \rho') + v\frac{\partial}{\partial y}(\rho_o + \rho') + w\frac{\partial}{\partial z}(\rho_o + \rho') = 0 \tag{4.6}$$

here, $\rho_o(z)$ and $\rho'(t)$. Consequently, the density gradients with respect to the horizontal component are $\partial(\rho_o + \rho')/\partial x = \partial(\rho_o + \rho')/\partial y = 0$. The equilibrium density gradient with respect to time is also invariant: $\partial\rho_o/\partial t = 0$. However, the density perturbation changes with time. The vertical background density variation is retained to obtain:

$$\frac{\partial\rho'}{\partial t} = -w\frac{\partial\rho_o}{\partial z} \tag{4.7}$$

The density perturbation is produced only by the vertical variation of the background density distribution.

The temperature variations and the gravity forces dominate the dynamics of the fluids in the MLT region. Thus, the viscosity and rotation terms are neglected from the *momentum equation* (4.3). Assuming small perturbations p' and ρ', the following system is obtained for the three components (x,y,z)

$$\rho_o\frac{\partial u}{\partial t} + \frac{\partial p'}{\partial x} = 0 \tag{4.8}$$

$$\rho_o\frac{\partial v}{\partial t} + \frac{\partial p'}{\partial y} = 0 \tag{4.9}$$

$$\rho_o\frac{\partial w}{\partial t} + \frac{\partial p'}{\partial z} = -g\rho' \tag{4.10}$$

The definition of the *Brunt-Väisälä frequency* (named after *Brunt* [1927] and *Väisälä* [1926]) is also dependent on the vertical background density variation

$$N^2 = -\frac{g}{\rho_o}\frac{\partial \rho_o}{\partial z} \tag{4.11}$$

$N(z)$ is also known as the *buoyancy frequency* after *Turner* [1973] since the restoring force that produces the oscillation is the buoyancy force, F. It has units of (rad/s).

To obtain the relationship for the vertical oscillations in the atmosphere, equation (4.10) is differentiated with respect to t and combined with equation (4.7). Using the definition of the *buoyancy frequency*, the following expression is obtained:

$$\frac{\partial^2 w}{\partial t^2} + N^2 w = -\frac{1}{\rho_o}\frac{\partial^2 p'}{\partial z \partial t} \tag{4.12}$$

When the variations of the perturbed pressure vanishes ($\partial p'/\partial t = 0$), the solution of equation (4.12) represents vertical oscillation in the atmosphere. This vertical movement has the frequency of oscillation $N(z)$, produced by the *buoyancy force*, F,

$$F = \rho g V \tag{4.13}$$

where V is the volume displaced by the buoyancy force.

4.2.2 Stable and unstable conditions

The atmosphere could be statically stable or unstable accordingly to the solutions of equation (4.12) when neglecting variations of the pressure perturbations with respect to time and height.

$$w(t) \quad = \quad Ae^{iNt} + Be^{-iNt} \tag{4.14}$$

where A and B are constants. The solutions are oscillatory if the *buoyancy frequency* (N) is real (or $N^2 > 0$). In this case the *buoyancy period* is $2\pi/N$. If the *buoyancy frequency* is imaginary (or $N^2 < 0$), there are growing solutions associated with unbounded vertical growth.

To understand the stability of the atmosphere, the example of the exchange of two parcels of fluid at different levels is used. If the parcel ascends to reach a level where it is heavier than the surroundings, then gravity forces the parcel to descent, generating oscillations. For this case, the equilibrium is stable when the solutions are damped or the Brunt-Väisälä frequency is positive ($N^2 > 0$). The solution from equation (4.12) is $w(t) = A\cos(Nt) + B\sin(Nt)$, since $e^{\pm iNt} = \cos(Nt) \pm i\sin(Nt)$ (See Figure 3.5 a)).

The atmosphere is convectively unstable, however, if the parcel is lighter than the surroundings and is not restored to the original position. The condition for instability is present when the solutions are exponentially growing $w(t) = Ae^{Nt} + Be^{-Nt}$ (when negative buoyancy frequency, $N^2 < 0$) (See Figure 3.5 b)).

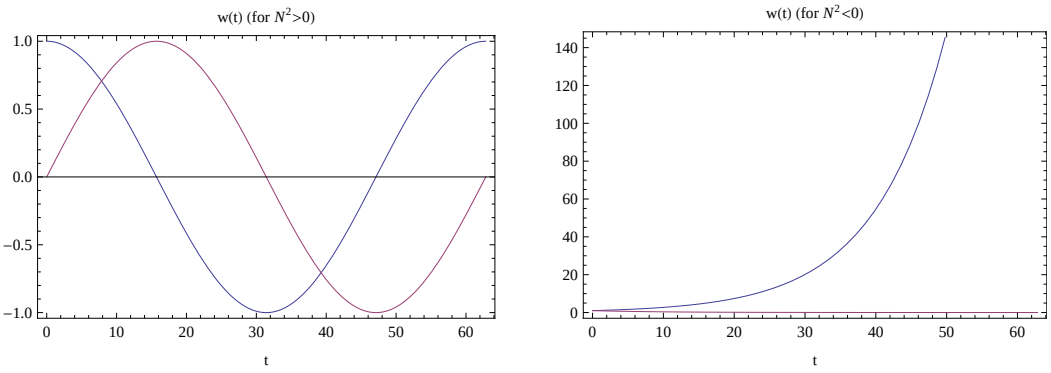

a) b)

Figure 4.1: Solutions for the equation (4.12) when $\partial p'/\partial t = 0$. a) Oscillatory solutions when $N^2 > 0$ are form by the combination of the two terms (red and blue) shown here. b) Solutions when $N^2 < 0$ are dominated by the exponentially growing term (blue).

4.2.3 Buoyancy frequency - temperature dependance

The atmosphere could be statically stable or unstable accordingly to temperature changes in height (or the vertical component, z). For adiabatic conditions (no variations in the total heat content), the temperature change dT is related to the pressure change dp by

$$dT = \frac{\alpha T}{\rho c_p} dp \tag{4.15}$$

where c_p is specific heat at constant pressure and α is the thermal expansion coefficient for constant composition, $\alpha = -\rho^{-1}\partial\rho/\partial T$. Introducing the *hydrostatic equation* (4.5) in equation (4.15), the relation between temperature and the adiabatic lapse rate is obtained

$$dT = \Gamma dz \tag{4.16}$$

The adiabatic lapse rate, $\Gamma = -g\alpha T/c_p$, is an indicator of the variations in density with respect to temperature when there is no heat transfer with the surroundings. However, there are internal density changes

$$d\rho = \left(\frac{\partial \rho}{\partial p}\right) dp + \left(\frac{\partial \rho}{\partial T}\right) dT \tag{4.17}$$

From equation (4.15), the expression $\partial\rho/\partial p = -\alpha^2 T/c_p$ is obtained. The Brunt Väisälä frequency dependence on temperature, $N^2(T)$, is finally obtained by introducing the previous expression for $\partial\rho/\partial p$ in the equation (4.17). Introducing its derivate with respect to z into the equation (4.11), the following expression is obtained:

$$N^2 = g\alpha \left(\frac{dT}{dz} + \Gamma\right) \tag{4.18}$$

Equation (4.18) is equivalent to the equation (3.1) for the Brunt-Väisälä frequency shown in the previous chapter when conditions for an ideal atmosphere $\Gamma \equiv g/c_p$ are considered. The buoyancy frequency is associated with a period $T_B = 2\pi/\sqrt{N^2}$.

The condition for instability ($N^2 < 0$) is present when the force produced by the vertical shear in temperature is larger than a factor of the gravitational force (or the adiabatic lapse rate for an ideal atmosphere). These conditions were observed below 96 km almost every day in the observations to follow.

4.3 Observations

The ionosphere absorbs solar UV radiation, creating free electrons and ions. During that process, the photoelectron kinetic energy is increased. The highly energetic photoelectrons are thermalized via inelastic collisions with neutrals and electron Coulomb interactions. The newly thermalized photoelectrons are cooled by vibrational and rotational electron and ion motion as well as by heat transfer when ions elastically collide with neutrals. The electron, ion, and neutral temperatures are dominated by collisions. Below 200 km, quasi-thermal equilibrium ($T = T_e = T_i = T_n$) is reached due to the constant heat exchange via neutral collisions. For higher altitudes, this assumption is not valid because of the neutral density decreases and also the neutral collisions. With smaller neutral collision frequencies, the heat transfer is not effective and there is no thermal equilibrium. For the purpose of this study, quasi-thermal equilibrium is assumed. Electron temperature estimates from Arecibo are obtained by fitting the backscatter power spectrum to the theoretical autocorrelation function. This function has steep peaks when high-temperature electrons are present but is almost flat for cold electrons. The autocorrelation function is calculated assuming the ion composition of O^+, O_2^+, and NO^+, as described in equation (2.17).

Temperature estimates have been obtained during ISR World-Day campaigns at Arecibo. The estimates are calculated when Arecibo is pointing at zenith (using the line feed system). Some of the profiles have nearly constant positive temperature gradients (dT/dz). However, some profiles have different structures that induce inverse temperature profiles (See Figure 3.6 panel c, corresponding to September 14, 2014). Previous Arecibo observations by *Hysell et al.* [2009] and *Hysell et al.* [2014] showed temperatures with inverted profiles at the

bottom of the *E*-layer. However, they were focused on studying the presence of dynamic instability and did not explore the possibility of static instability.

The temperature profiles are used to calculate the *Brunt Väisälä frequency* and period (equation (3.2)) in the range 90 - 130 km using the parameters in Table 4.3. The buoyancy values are calculated only when the temperature error is less than 20%. The *buoyancy period* is calculated only for positive values of the *buoyancy frequency*. The temperature gradient is computed using the five-point differentiation equation (4.19) to smooth spurious data and obtain an error term $O(h^{(4)})$.

$$\begin{aligned} \frac{dT}{dz}(z_o) = \quad & \tfrac{1}{12h} \quad \Big[T(z_o - 2h) - 8T(z_o - h) \\ & +8T(z_o + h) - T(z_o + 2h)\Big] \\ & +\frac{h^4}{30}T^{(5)}(z) \end{aligned} \tag{4.19}$$

where z_o is the center altitude and h is the vertical resolution.

An isothermal ionosphere ($dT/dz = 0$) with a mean temperature of 250 K has a buoyancy frequency N $\sim 0.02\ s^{-1}$ which corresponds to a period of $\sim$ 5 min. This period has been assumed as the buoyancy period of the MLT region in most of the literature. However, the ionosphere is not isothermal, and positive mean temperature rates of the order $\sim$ 10 K/km are observed, which corresponds to buoyancy period of $\sim$ 4 min. When the temperature profiles are non-uniform, these rates increase, and smaller (bluish) and larger (reddish) periods are observed as it is seen in panel d) from Figures 3.6 and 4.6. For cases when the temperature is mostly uniform, periods close to 5 min are observed (greenish color). The observations here show strong horizontal bands with pe-

riods close to 3 min at altitudes were strong temperature gradients are found. These bands are not necessarily located at the same altitude as the ion layers (see Figure 4.3).

The square of the *buoyancy frequency* (N^2) is sometimes negative at altitudes where the temperature gradient is more negative than the negative adiabatic lapse rate ($dT/dz < -\Gamma$). This condition suggests the presence of convective patterns along the lower MLT region. Negative values of N^2 are distributed all through the E layer. However, a larger concentration is frequently found at altitudes close to 100 km (see Figure 4.4) or above the structures observed in the temperature profile. The Figures 4.4 and 4.5 show the combined and positive and negative *Brunt - Väisälä frequency* profiles.

The backscatter power detected by the Arecibo radar is proportional to ion density. Usually, the density profiles are obtained by calibrating the backscatter profiles with data collected by ionosondes. Nighttime high-density ion layers are known as sporadic or E_s layer. In Figure 3.6, the E_s layer seems to be associated with inverted temperature profiles, propagating after sunset with negative buoyancy frequencies. Previous observations with Arecibo have also shown inverse temperature profiles at night, e.g. observations from the night of September 27, 2008, between 20-21 h and 25 - 30 h (LT) (See Figure 4.6). It seems that convective activity could be present in the E_s layers.

N^2 Parameters		
Adiabatic lapse rate	Γ	9.47 K km^{-1}
Gravity at 100 km	g	9.5 m s^{-2}
Atmospheric specific heat for T = 250K	c_p	1003 J kg^{-1} K^{-1}

Table 4.1: Parameters used to calculate the Brunt Väisälä frequency for the Figures 3.6 and 4.3. Here the lapse rate for an ideal atmosphere is $\Gamma \cong g/c_p$ (equivalent to $\alpha = 1/T$). Gravity changes with altitude at $g(z_o) = g_o/R_e^2(z_o + R_e)^2$, where R_e is the radius of the Earth.

4.4 Discussion

The focus of this chapter is the presence of inverted temperature ($dT/dz < 0$) profiles that could cause static instability in the lower MLT region. Sensitive measurements from Arecibo show negative temperature gradient profiles between 90 and 100 km. Previous Arecibo observations have been used to calculate temperature profiles that show these inverted layers, but they have not been used to calculate negative buoyancy frequency or Richardson numbers parameters. This chapter studies the buoyancy frequency for two Arecibo World-day campaigns performed in 2013 and 2014. When the profiles are analyzed, negative patches of the Brunt-Väisälä frequency are often observed at the bottom of the E layer, suggesting the presence of convective zones. Sometimes, these layers persist throughout the morning and continue during the afternoon and early evening. The inverted layers that persist into the evening with negative buoyancy seem to match the characteristics of the lower sporadic E_s layers that emerge at night. Since the ion chemistry used to estimate the temperatures in this chapter corresponds to the diurnal characteristics, conclusions for nighttime observations can not be extrapolated from the data shown here. However,

the height and width from previous nighttime observations agree with the sporadic layers present below or around 100 km (p.e. observations shown in Figure 4.6). These layers are not caused by the instability itself, but both could have a common cause, like breaking gravity waves.

The formation of diurnal ion layers and nocturnal E_s-layers is controlled by tides, although unexpectedly sharp density increases along with the locations of E_s-layers seem to be the effect of instability. Lower *E*-region layers between 95 to 105 km have been attributed to the diurnal tidal mode S(1,1) with a descent speed of approximately 1.0 km/h (*Haldoupis* [2011a]). However, the ion layers presented here seem to maintain altitude or in some cases to ascend during the local afternoon (See Figures 3.6 and 4.3).

One possible explanation for the formation of the observed inverse layers is daytime ozone dynamics, but the range of altitude does not coincide with ozone observations performed by *Mlynczak et al.* [2001]. Also, planetary waves could be driving the instabilities, but *Brown et al.* [2004] showed that the long-wavelength planetary waves cause wave dissipation, creating the lower layer of the MIL at around 80 km. The height and width of the inverse layers here are consistent with the characteristics of the upper layer of the double MIL, presented by *Meriwether and Gerrard* [2004]. However, the MILs seem to maintain a constant height.

Previous observations of layers between 80 to 100 km during the AIDA campaign at Arecibo in 1989 also showed wavy activity in addition to tidal influence (*Mathews* [1998]), suggesting a zone of gravity wave - tidal interaction. Tidal compression alone can generate changes in the temperature gradient. However, *Zhou and Mathews* [1995] showed that gravity waves affect the ionospheric

temperature by two mechanisms. The temperature gradients can vary due to compression of the mass when the gravity wave velocity is not in the range that produces dynamic instabilities $R_i < 1/4$. Also, the temperature changes are more severe when the tidal-gravity wave interaction generates breakdown gravity waves (with shorter wavelengths). Then, viscous dissipation transfer energy to the background medium because of the newly created high-speed short waves. These short wavelengths also seem to explain the shorter periodic structure inside some ion layers. In this case, the peak of the temperature gradient (= N^2 peak) follows the altitude of the maximum energy deposition.

Gravity wave breaking creates a stable zone below the breakdown height due to the increment in the temperature gradient. However, above the breakdown height, a zone of unstable conditions could be created, generating additional breaking, depositing energy at higher altitudes, and inducing an upward motion of the ion layer. Observations on September 14, 2014 between 86-87 h (LT) (see Figures 3.6 and 4.4) agree with this condition. At that time, there was an upward movement of the ion layer (110 -120 km) associated with a lower very stable zone (large $N^2 > 0$ at 115 km) and an unstable upper zone ($N^2 < 0$ at 118 km). As the ion layer ascended, the tidal force became negligible, and the breaking effects were intensified. If the breakdown height does not change in altitude, the location of the energy deposition is fixed, and ion layers keep their altitude (like the MILs).

Heating due to the constant gravity wave - tidal interactions can induce negative N^2 and launch growing vertical perturbations that generate ascending ion layers. The frequent presence of patches of negative Brunt Väisälä frequency along the layer suggests the permanent gravity-wave breakdown at *E*-layer

heights. Vertical descending speeds from the tides encountering positive ascending speeds due to convection could generate a concentration of ions. These ion density enhancement explains the formation of layers at unexpected places.

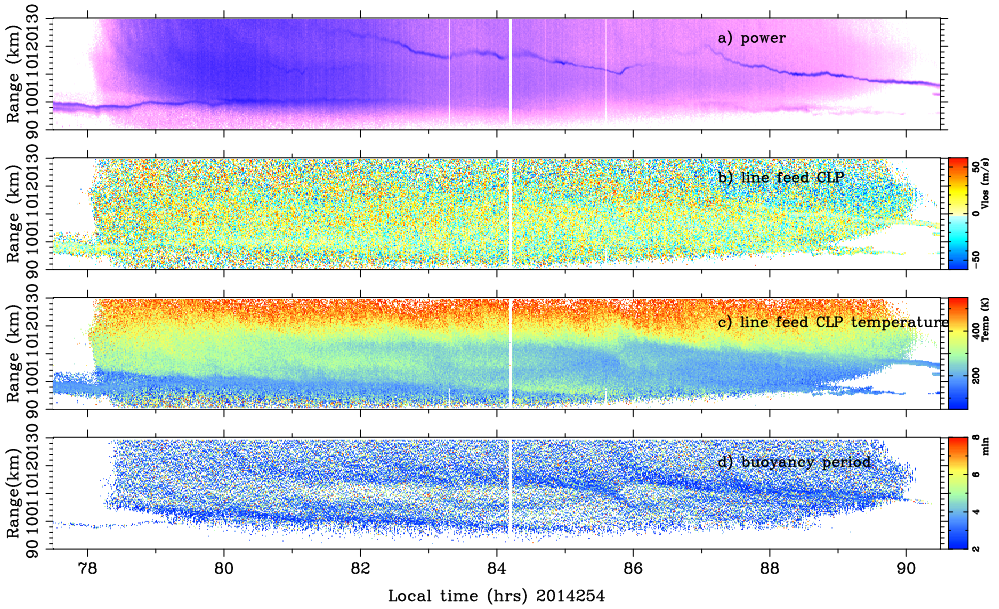

Figure 4.2: Temperature (^oK) and *buoyancy period* (min) for the observations made on September 14, 2014, which correspond to the fourth day (72 - 96 h LT) of the campaign started on September 11. Here, the first two panels show the data collected with Arecibo: a) backscatter power (the proxy of ion density), b) ion drift for the line feed (looking vertically). Panel c) is the temperature ($T = T_e = T_i = T_n$) (See text for details). Panel d) is the *buoyancy period* (min) calculated with the gradient of the previous panel. The strongly varying conditions in the temperature profiles generates conditions to observe buoyancy periods from 3 - 10 min or larger. In this non - isothermal medium negative gradients are also generated to develop the conditions to seed convection instability.

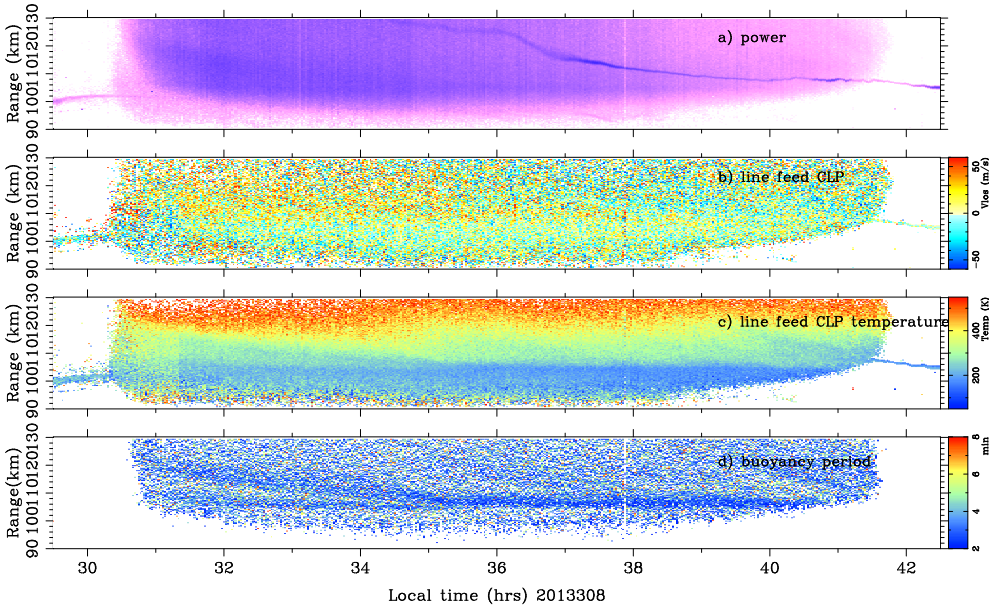

Figure 4.3: Temperature (^oK) and *buoyancy period* (min) for November 6, 2013 (the third day of the campaign started on November 4). See text from Figure 3.6 for panel descriptions. This day is an example of mostly uniform *E* region temperatures. The *buoyancy period* is close to 5 min for most of the region. However, the period is smaller in some horizontal areas around 105 km. In those areas, the temperature gradients are steep.

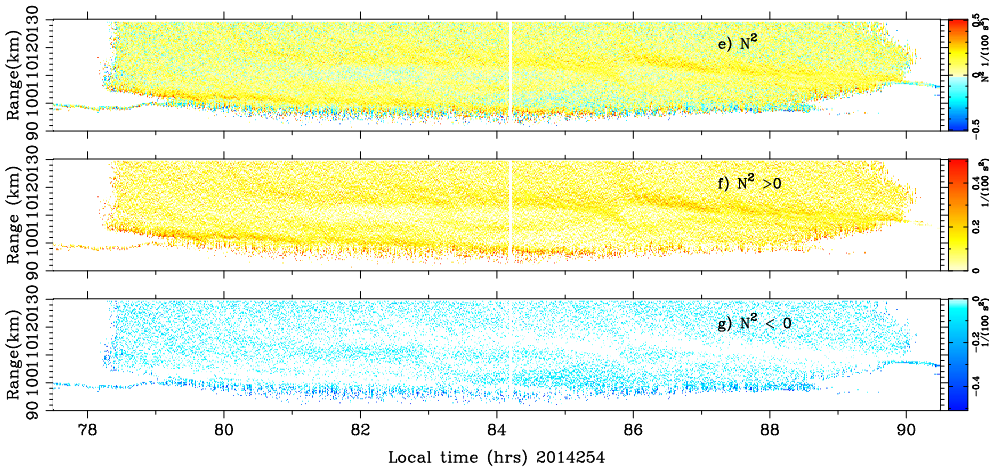

Figure 4.4: *Brunt-Väisälä frequency* ($N^2(1/s^2)$) profiles scaled by 10^{-2} for September 14, 2014 (see Figure 3.6). The first panel corresponds to the complete frequency profiles, calculated when the temperature error is less than 20%. Negative frequency values are indicated with bluish colors, and positive frequency values with a scale from yellow to red. The second panel shows just the positive values. The third panel shows the negative values in the same scale used for the first panel. Negative values are distributed all around the *E* region, but the bottom of the layer has the largest abundance of negative values. The conditions to develop convection instability are present.

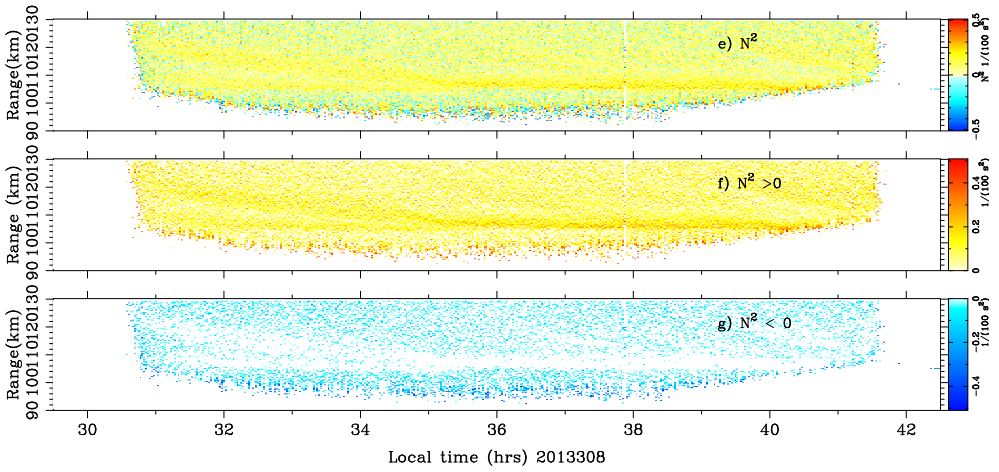

Figure 4.5: *Brunt-Väisälä frequency* ($N^2(s^{-2})$) profiles divided by 10^2 for November 6, 2013 (see Figure 4.3). Although this day has more uniform temperature changes, the presence of negative buoyancy frequency all around the region is shown.

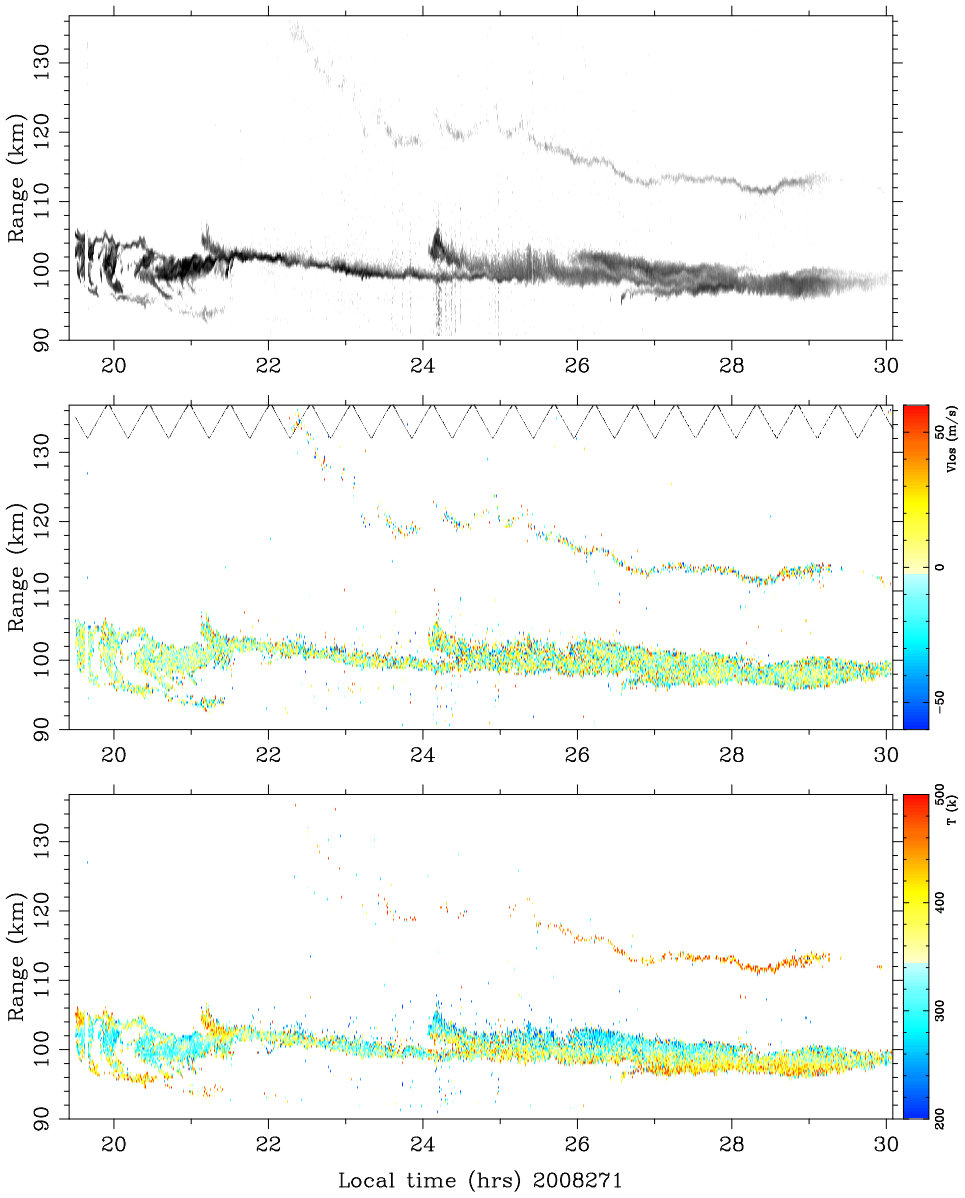

Figure 4.6: Arecibo nighttime observations from September 27, 2008 between 90-130 km vertical range. The panels correspond in order to 1) power profile, 2) ion drift profile, and 3) temperature profile. At the beginning of the night, Kelvin-Helmholtz rolls are observed (see *Hysell et al.* [2009] for analysis before 22h). After midnight through sunrise, inverted temperature profiles are seen. The conditions to develop convection instability are present.

5

DAYTIME DYNAMIC INSTABILITY

"The waves broke and spread their waters swiftly over the shore. One after another they massed themselves and fell; the spray tossed itself back with the energy of their fall. The waves were steeped deep-blue save for a pattern of diamond-pointed light on their backs which rippled as the backs of great horses ripple with muscles as they move. The waves fell; withdrew and fell again, like the thud of a great beast stamping."

– Virginia Woolf, *The Waves*

Dynamic instabilities have been observed in the sporadic E_s layer. Strong neutral wind shear that could induce Kelvin-Helmholtz rolls characterizes this kind of irregularity. Some characteristics of the E_s like split layers and patchy ion density areas can be attributed to this mechanism.

Billow activity is frequently present in the ion layers measured by the Arecibo ISR during the night. However, little research has been done to detect them during the day. This chapter investigates the presence of the necessary condition ($0 < R_i < 1/4$) to develop this irregularity during the day. Some examples are presented.

5.1 Introduction

The influence of neutral winds on plasma irregularities in the mesosphere and lower thermosphere (MLT) region has been studied for a half a century by

Dungey [1959], *Hines* [1960], *Whitehead* [1961] and *Axford* [1963] and many others. In the early nineties, *Yamamoto et al.* [1992] detected coherent echoes associated with irregular sporadic E layers (or E_s), using the MU radar in Japan. Extensive experimental capabilities for studying the relationship between the background conditions and the irregularities have been developed. In the Asian sector, the SEEK sounding rocket campaigns (*Fukao et al.* [1998], *Yamamoto et al.* [2005] and references therein) characterized the phenomena using in-situ plasma and neutral gas measurements. In the American sector, recurrent observations using the Arecibo incoherent scatter radar and coherent scatter radars with a common volume (*Hysell et al.* [2004] and references therein) are contributing details about the internal and regional structure of the irregularities and their evolution at night.

In earlier studies, *Miller and Smith* [1978] and *Smith and Miller* [1980] attributed mid-latitude E_s layers structure to turbulence generated by Kelvin-Helmholtz instability. *Larsen* [2000a] also attributed the large deformations in midlatitude E_s layers to neutral shear instability. *Larsen* [2002] pointed out the potential importance of large turning shears on atmospheric stability. *Larsen et al.* [2007] showed similarities between the neutral irregularities observed with green-line emission and plasma irregularities observed with radars.

Observations of pure neutral activity in the MLT region suggest that the region is dynamically unstable according to the Richardson number criterion, $Ri < 1/4$, for example *Hecht et al.* [2004], *Gardner et al.* [2002], and *Yue et al.* [2010]. Large neutral wind shears have been reported between 85 and 95 km in sodium lidar observations performed by *Fritts et al.* [2004] and *She et al.* [2004]. Some lidar facilities are able to estimate wind profiles as reported by *Liu et al.*

[2002] (in New Mexico), *Franke et al.* [2005] (in Hawaii), and *She et al.* [2009] (in Colorado). These facilities operate mostly at night.

In the inviscid fluid theory, strong shears are usually related to dynamic instability which has been studied extensively for two-dimensional flows (see *Drazin and Howard* [1966] for review). *Bernhardt* [2002] and *Bernhardt et al.* [2006] used models based on neutral wind forcing to investigate the evolution of observed coherent irregularities in the *E* region. *Hysell et al.* [2012] numerically solved the eigenvalue problem associated with Kelvin-Helmholtz dynamic instability.

New methodologies for measuring neutral winds and temperatures are also emerging. Techniques based in Fabry-Perot interferometry to measure the Oxygen emission at about 250 km altitude are implemented by *Makela et al.* [2011], *Englert et al.* [2012], and *Harding et al.* [2015]. *Stober and Chau* [2015] are developing a methodology to perform wind measurements at about 100 km altitude, using specular meteor radars. *Hysell et al.* [2014] uses ISR measurements to estimate neutral winds and temperatures at MLT altitudes. The ISR technique is used in this chapter to study daytime neutral winds over Arecibo, looking for the presence of dynamic instability in the MLT region. Specifically, a search for regions with $R_i < 1/4$ is performed. The first daytime analysis is presented for time intervals in 2013 and 2014 when these rare daytime irregularities were also present.

5.2 Dynamical stability model - Miles and Howard equations

The dynamical stability problem was address by *Miles* [1961] and *Howard* [1961]. They started with the linearized equations of motion, incompressibility and continuity as follows:

$$\rho\left(\frac{Du}{Dt} + U'w\right) = -\frac{\partial(p)}{\partial x} \tag{5.1}$$

$$\rho\left(\frac{Dv}{Dt} - N^2\eta\right) = -\frac{\partial(p)}{\partial z} \tag{5.2}$$

$$\frac{D\eta}{Dt} = w \tag{5.3}$$

$$\frac{\partial u}{\partial x} = -\frac{\partial w}{\partial z} \tag{5.4}$$

where $\frac{D}{Dt} = \frac{\partial}{\partial t} + U\frac{\partial}{\partial x}$ and $'$ indicates $\frac{d}{dz}$, ρ is density, p is pressure, u and w are the horizontal and vertical components of the perturbation velocity, g is gravity, and $N^2 = \frac{-g}{\rho}\frac{d\rho}{dz}$ is the Brunt Väisälä frequency term (see equation (4.11)). The density is perturbed $\rho = \rho_o - \rho_o'\eta$. The shear flow is $S = U'$ (see equation (3.2)).

Assuming spatially-periodic wave, a vertical perturbation could be represented by $\eta = F(z)e^{i(kx-\omega t)}$ where k is real and $\omega = \omega_r + i\omega_i$ is complex. This mode corresponds to a wave traveling in the $\mathbf{k}$ direction with phase velocity $\omega_r/|k|$. The flow is stable when $\omega_i \leqslant 0$ (or $\eta \sim e^{-|\omega_i|t}$) and unstable when $\omega_i > 0$ (or $\eta \sim e^{|\omega_i|t}$). Substituting η into the linearized equations (5.1) to (5.4) leads to the differential equation:

$$(\rho_o W^2 F')' + \rho_o \left[N^2 - k^2 W^2\right] F = 0 \tag{5.5}$$

Using $G = W^{1/2}F$, the differential equation takes the following form which is suitable for studying non-singular oscillations:

$$(\rho W G)' - \left[\frac{1}{2}(\rho U')' + k^2 \rho W + \frac{\rho}{W}(\frac{1}{4}U'^2 - N^2)\right] G = 0 \tag{5.6}$$

where the intrinsic phase speed of the perturbation W is defined by $W \equiv U - \omega$. The variables W and η can be written in three dimensions: $W = \frac{k_x u + k_y v - \omega}{k}$, $\eta = F(z)e^{\imath(k_x x + k_y y - \omega t)}$ (*Drazin* [2002]), using the standard variables for the atmospheric wind (u, v, w), where u is the zonal, v is the meridional and w is vertical wind. The boundary conditions are $F(z_o) = F(z_n) = 0$, where z_o and z_n correspond to the boundaries of the unstable region of interest.

Equation (5.6) can be integrated after multiplication by the complex conjugate G^*, with $\omega_i > 0$. The imaginary part becomes:

$$\int \rho(|G'|^2 + k^2|G|^2) + \int \rho(N^2 - \frac{1}{4}U'^2)\left|\frac{G}{W}\right|^2 = 0 \tag{5.7}$$

This equation establishes the most widely used instability condition when high-shear neutral winds are considered, as explained in the following section.

5.2.1 Instability criteria

Analyzing equation (5.7), it is apparent that the second integral should be less than or equal to zero because the first term is positive. Also, $N^2 \geqslant 0$ because the density stratification is the stabilizing agent ($-\frac{1}{\rho}\frac{d\rho}{dz} \geqslant 0$). These two conditions lead to the necessary condition for instability stated by *Miles* [1961] and known as the Richardson number condition:

$$R_i = \frac{N^2}{U'^2} = \frac{N^2 k^2}{(k_x u' + k_y v')^2} < \frac{1}{4} \tag{5.8}$$

Howard [1961] alerted about the points near $U' = 0$, where the R_i number is not well defined.

Similar criteria for instability have been found for wind profiles in the Boussinesq limit, neglecting the buoyancy term (resulting in Rayleigh's stability equation). The condition for instability $U''(z_c) = 0$ was stated by *Rayleigh* [1879]. Later, a stronger criterion was obtained by *Fjörtoft* [1950], requiring $U''(z)(U(z) - U(z_c)) < 0$. Rayleigh's and Fjrtoft's generalizations are necessary but not sufficient conditions for instability. *Rosenbluth and Simon* [1964] found a necessary and sufficient condition for plane parallel flows in terms of the wind profiles, using the Nyquist method when the wind profile has one inflection point. *Balmforth and Morrison* [1999] expanded this work, finding that Rayleigh's equation has an unstable eigenmode solution if the following condition can be satisfied by a wavenumber k and at least one inflection point z_c:

$$\int \frac{U''(z)\phi(z,k)}{U(z) - U(z_c)} dz > 1 \tag{5.9}$$

where $U''(z_c) = 0$. Equation (5.9) is considered the necessary and sufficient condition for instability.

5.2.2 Growth rate

Miles [1961] delimited the horizontal velocity $a \leqslant U(z) \leqslant b$ and used equation (5.5) to conclude that the complex wave velocity ω of an unstable mode should lie inside the semicircle in the upper half-plane with U for diameter.

$$\left[\omega_r - \frac{1}{2}(a+b)\right]^2 + \omega_i^2 \leqslant \left[\frac{1}{2}(a-b)\right]^2 \tag{5.10}$$

this is known as the semicircle theorem. Using the theorem and *Miles* [1961] limits for the Richardson number in the case of the unstable modes, *Howard* [1961] estimates the maximum growth rate as:

$$\omega_i^2 \leqslant Max\left[U'^2\left(\frac{1}{4} - R_i\right)\right] \tag{5.11}$$

This statement is not entirely accurate but gives a good approximation of the order of magnitude of the maximum growth rate.

5.3 Daytime observations

Observations for the MLT region over Arecibo were made during the World day campaigns in 2013 and 2014. The configuration of the Arecibo ISR is described in Chapter 2. For day-time data collection during the campaigns, the neutral

winds were estimated. The winds clearly reflect diurnal and semidiurnal tides, with layers of strong shear in the vertical direction. In some cases, the Arecibo backscatter power profile shows descending ion layers that oscillate or break, perhaps due to dynamic instability effects.

The Richardson number is calculated (see equation (5.8)) to investigate dynamic instability. The R_i is calculated with the same assumptions used in the previous chapter. The parameter values used to calculate N^2 were $\Gamma = 9.47$ (K/km) and $g = 9.5$ (m/s). The R_i depicted in Figures 5.2 and 5.3 corresponds to temperature errors less than 20% and temperature values smaller than $800K$. The temperature gradient is calculated using equation (4.19) and smoothed in the vertical direction. The wind shear is calculated using the perturbation wave vector. Following *Howard* [1961], the R_i calculation ignores small values of shear ($S > 10^{-9}$).

For most of the collected data, the condition $R_i < 1/4$ is infrequently observed during the daytime. However, for some individual cases, the instability condition is satisfied, usually in the presence of wavy ion layers. Two examples are shown here from late summer 2013 and fall 2014. That time of the year coincides with the daytime seasonal electron density peak (or maximum f_oE), detected by (*Baggaley* [1985]).

The conditions for ion convergence under the wind-shear mechanism are present for the time of the instabilities. E layer formation due to wind shear was proposed by *Whitehead* [1961], *Whitehead* [1972], and *Whitehead* [1989]. The ion convergence is generated when the propagation in the vertical direction is $V_{up} < 0$ above $V_{up} > 0$ (see Figure 5.1), were V_{up} is the velocity in the vertical direction accordingly to equation (2.11). Developing the equation and neglecting

the electric field and the neutral vertical velocity, the vertical ion motion is:

$$V_{up} = -r_1 \sin(\xi) u + r_2 \sin(\xi) v \tag{5.12}$$

where u and v are the horizontal components of the neutral winds and r_1 and r_2 are indicated in equation (2.8). The conditions that generate a layer due to a zonal wind shear are present when westward winds are above eastward winds. The meridional wind shear mechanism requires northward winds above southward winds. The later mechanism is present most of the time when we observe diurnal dynamic instability.

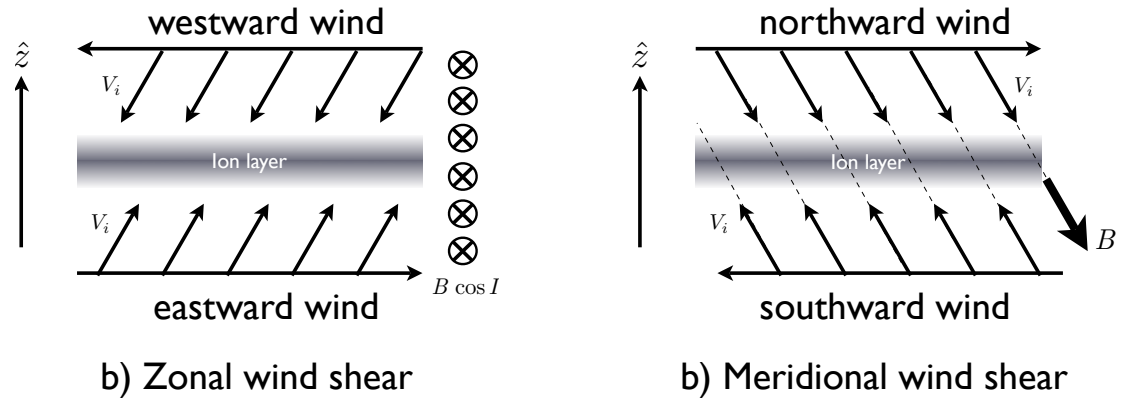

Figure 5.1: Illustration for the zonal and meridional wind shear theory mechanism of ion layers in the lower E region. This mechanism was developed to explain the Sporadic E layer formation.

High-density, descending ion layers were observed in the Arecibo backscatter power profiles on September 11, 2014 (see Figure 5.2). Starting the previous night, a low-altitude ion layer was present at around 100 km. This altitude could correspond to a diurnal S(1,1) tidal wind mode. Just after sunrise, the E region became intensely ionized by sunlight, and many descending layers

formed. Similar phenomena were observed by *Mathews* [1998] at night, a phenomenon he called "ion rain". Some of these descending layers were stronger than their companions. The intense ionization lasted until 11 am (LT) (83h of the campaign). The buoyancy period was close to 5 min. The horizontal wind shear (see Figure 5.2, panel g) shows extreme stratification and rapid changes in velocity in a confined altitude region. Inside the shear stratification layers, blue ($R_i < 1/4$) patches indicate the possibility of the development of instabilities. Those blue areas are present at the same time that wavy activity is observed in one of the intermediate descending-ion layers.

After 11 am (LT) on the same day, just one strong descending layer is seen. At 2 pm (LT) (86h), the layer started to ascend, and the density decreased until it is becoming invisible in the power profile. A few minutes later, the layer seems to reappear 5 km higher and was oscillating. At 3 pm, the layer became strong and descended again. During that period, an increase in the magnitude of the vertical neutral wind took place. The direction of the vertical speed enhancement was highly correlated with the ion layer movement. This activity could be the result of the presence of a gravity wave. There is neither evidence of high wind shear nor of $R_i < 1/4$ during that time.

During the day of November 7, 2013, (see Figure 5.3), much weaker ionization was observed. The neutral wind estimates were clearly stratified, producing a layer of high-speed shears at about 110 km altitude starting at 9:30 am (LT) (81.5h) and continuing into the afternoon. The wind shears were the strongest for a half hour (82.5 - 83h) around 110 km. The buoyancy period for that time and altitude was near 2.5 min. However, the high buoyancy frequency compensated for the high wind shear, producing areas with $R_i < 1/4$. During the same

period, the zonal and meridional winds were oriented in the way that facilitated ion convergence at altitudes close to 115 km (westward above eastward winds for the zonal and northward above southward winds, for the meridional). Although at this time the ion layer was barely perceptible in the Arecibo backscatter power profiles, the neutral background activity indicates the formation of irregularities.

The presence of $R_i < 1/4$ is observed during daytime at altitudes just below the ionization peak, which seems to agree with nighttime observations where the irregularities are observed at the bottom of the E_s layer (*Hysell et al.* [2009]). The wind profiles associated with the irregularities is spiral with more than a complete closed turn, agreeing with the previous nighttime observations. For the examples shown here, one case was cyclonic, and the other anticyclonic. Despite the direction of the winds, the conditions for ion convergence were present for the time and height of the irregularities described here.

The irregularities are presented at about the same altitude of the ion layer, which seems to correspond to the heights of the diurnal and semidiurnal tidal-wind modes. The diurnal tide is confined in the vicinity of few kilometers around 100 km altitude. Meanwhile, the semidiurnal tide descends from higher altitudes ($>$ 130 km) to reach the altitude of the diurnal tide at the end of the day or during the night. These layers propagate with descending rates that are in the proximity of the rates presented in the analysis of vertical propagation performed by *Haldoupis* [2011a]. The ion layers associated with the semidiurnal tide descend at a rate of ($\sim$ 2.2 km/h), and the diurnal tide descends at ($\sim$ 0.8 km/h). The extended altitude range influenced by the tides suggests that the irregularities could be present up to 130 km. However, the main effect

of the neutral winds is limited to the collisional region with gyro-to-collision frequency ratios $k_i = \Omega_i / \nu_{in} < 1$ (See Figure 2.2), where the ion layer confinement depends on the correct alignment in the direction of the neutral winds.

The winds producing the dynamic instabilities during the day and presented here are in close agreement with the daytime satellite observations made by TIDI, the Doppler interferometer on board the TIMED satellite (*Killeen et al.* [2006]). TIDI detects the orange, blue and red emissions of O_2 for altitudes between 70-120 km during the day and 80-103 km at night. Also, it is able to detect green-line emissions from O at night, complementing the previous measurements. Neutral winds are estimated using inverse methods. The satellite needs to go around the earth for 60 days to obtain the measurements corresponding to one full day at a particular location. The TIDI wind estimates for mid-latitudes show strong descending winds traveling north from 110 km altitude at sunrise to 100 km at sunset. The zonal winds moving eastward are located at higher altitudes, with descending peak winds going from 120 km to 100 km (sunrise to sunset) altitude. Those features are very similar to the winds estimated from the ion drifts collected with the Arecibo ISR and presented here (Figures 5.2 and 5.3). The nighttime wind profiles from TIDI show a jump in altitudes at sunrise and sunset, lowering the peak of the winds by 10 to 15 km in both the zonal and meridional components. The Arecibo estimates presented here are for daytime, but they do extend into nighttime, allowing us to observe the changes due to the presence or absence of solar ionization. However, previous Arecibo ISR nighttime estimates from E_s layers (*Hysell et al.* [2004], *Hysell et al.* [2009], *Hysell et al.* [2012], *Hysell et al.* [2014]) agree with TIDI observations and register the peak of the winds at lower altitudes than in the daytime observations.

There are altitude differences between the irregularities observed during the day and at night. Usually, nighttime ionospheric irregularities associated with QP echoes are seen at altitudes between 100-110 km. Meanwhile, the daytime examples show irregularities in the proximity of 110 km. One possible explanation is the change of altitudes for $k_i \sim 1$ between daytime and nighttime. During the day, the ratio $k_i = 1$ is met at about 120 km. At night, the ion collision frequency ($\nu_{in} \sim 10^{-5}(n + n_i)$) decreases due to the absence of solar radiation (*Kelley* [2009]), and the collisional region moves lower in altitude. Consequently, the ion layers (or E_s) present at lower altitudes than during the day. The change of collision frequency also affects the ion drag ($-\nu_{in}(V - U)$) from the *continuity equation* (equation (2.7)). For altitudes higher than $\sim$ 115 km, equation (2.7) decouples from the neutral winds at night. This factor plus the lower ionization preclude the formation of ion layers because of inappropriate zonal and meridional shear conditions in this altitude range. This explains the absence of the higher ion layers at night.

5.4 Discussion

Observations of daytime neutral activity in the E region are very sparse. Most optical instruments are not reliable during the day due to solar illumination. Just a few rocket experiments have been conducted to measure daytime neutral wind activity (*Mlynczak et al.* [2001] and *Pfaff et al.* [2012]) in the Mesosphere. Daytime neutral winds estimated from radar data are novel in the MLT region (*Hysell et al.* [2014]). Hence, the examples presented here correspond to the first neutral dynamic stability analysis in the daytime E region.

Instabilities generated by neutral winds are not frequently observed during the day. During the morning and early afternoon, most of the ion layers are present at relatively high altitudes, and the ratio between the ion gyro and collision frequencies does not allow ion irregularities forced by neutrals. However, there are some cases of low-altitude descending ion layers that seem to favor the development of irregularities. Two examples with $R_i < 1/4$ were presented in this chapter.

Variations in the Brunt-Väisälä frequency were reported for these datasets in the previous chapter. The period usually varies from 2 to 8 min. or more. The Richardson number $R_i = N^2/S^2$ can reach unstable values below $1/4$ when N^2 is small, even with modest speed shears. However, the observed shears are large and could induce large growth rates, accordingly to the approximation for Kelvin-Helmholtz billows $\sigma \propto (S^2 - 4N^2)$ (*Howard* [1961] and *Kunze et al.* [1990]) (see equation (5.11)).

Nighttime irregularities over Arecibo of the QP-echo kind usually propagate towards the south and southwest (*Hysell et al.* [2009]). The wind profiles at the time and altitude of the irregularities in question here had a southern direction, with some variations in the zonal direction. If the ion irregularities move in the same direction of the neutral winds, the changes in the direction of propagation could indicate a decoupling of geomagnetic field forcing.

The results presented here show dynamically unstable regions during the day which agree with most of the characteristics of the nighttime irregularities. However, the background Richardson number for most of the daytime *E* region is larger than unity. *Charney* [1947], *Eady* [1949], and *Green* [1960] suggest that baroclinic instabilities can occur for $R_i >> 1$ when large temperature gradients

are present. This is a possibility that could be researched in the future. *Howard* [1961] raised the issue of the possible misinterpretation of the R_i number when wind shears are small. To explore in detail the nature of the neutral particles and the ion layers that reside in the background ionization in the lower ionosphere, more detailed observations are required.

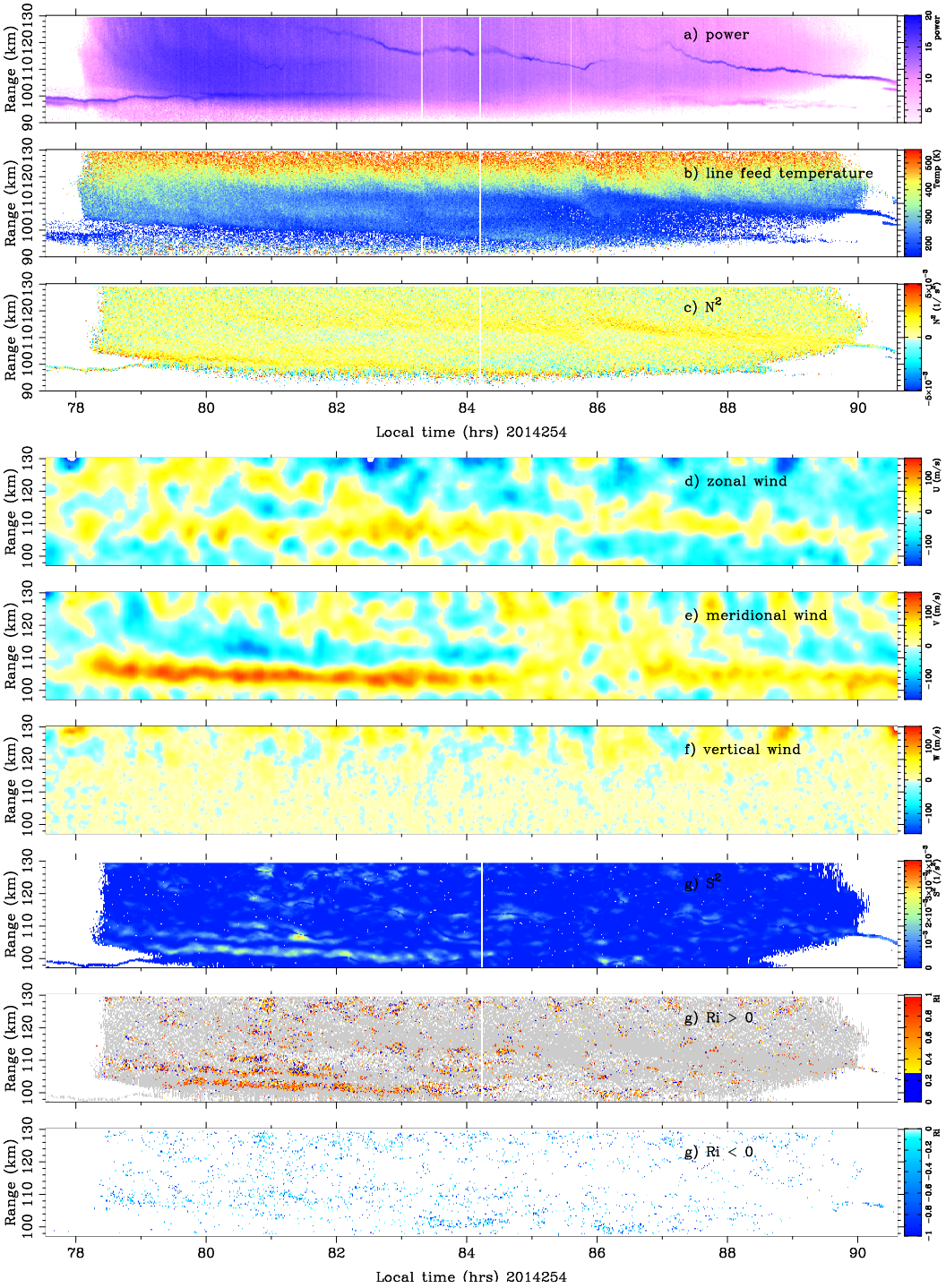

Figure 5.2: Day-time observations of the third day of the September 11, 2014, campaign. Data depicted from local sunrise to sunset 78.5h - 90h LT (or 6:30 am - 6:00 pm). (Continues on next page).

Figure 5.2: The data presented here and in the following figure show daytime observations for two campaigns where dynamic instability was detected. The first panel shows Arecibo backscatter power which is used as a proxy for electron density. The second panel is the estimated temperature for the line-feed measurements. The third panel corresponds to the buoyancy frequency. The fourth through sixth panels correspond to the horizontal and vertical neutral wind estimates. The seventh panel corresponds to the horizontal wind shear. The eighth panel is the positive Richardson number, where gray color indicates $R_i > 1$ and the color bar indicates $0 < R_i < 1$. The blue color is indicative of instability, $R_i < 1/4$. The last panel is the negative R_i, indicative of convection instability. Two main phenomena are worth noting during this day. The first is a rupture in the descending ion layer after 86h, possibly produced by gravity wave activity but without an indication of wind shears. Second, blue R_i patches are observed between 80 - 82h as a result of the high-speed shears and wave action at $\sim$ 110 km in a zone with high daytime background electron density that concealed the wave activity in a subtle descending ion layer. (See text for more details).

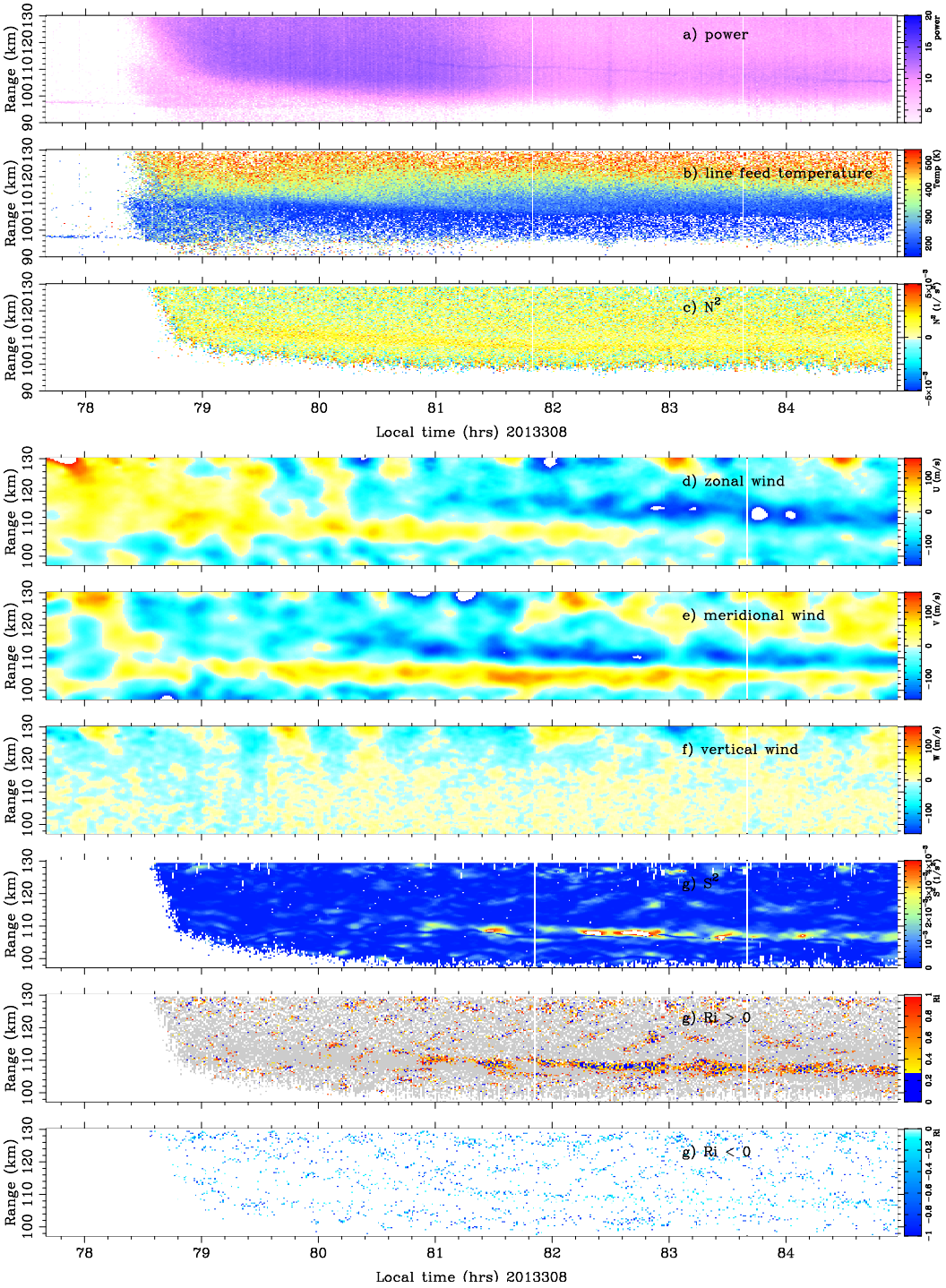

Figure 5.3: Day-time observations of the third day of the November 7, 2013 campaign. Panel descriptions are detailed in previous figure. (Continues on next page).

Figure 5.3: The data depicted goes from sunrise to sunset (78h-90h LT time of the campaign). The ion descending layers for that day were very subtle, and the temperature variation was very uniform throughout the day. However, at about 82h (LT) between $110 - 115$ km, the conditions for vertical ion convergence under the wind-shear mechanism were present. Additionally, the confined layer was located above a region with bursts of high meridional wind shears. These two factors created the growth of instabilities ($Ri < 1/4$), although the daytime ionization layer was weak. (See text for more details).

6

INSTABILITY INDUCED BY PLANETARY WAVES

"The wild winds had been sown and the whirlwinds were gathering."

– Pearl S. Buck

The effects of the rotation of the Earth are studied in the MLT. Previous analysis of convective and dynamic instabilities neglected the Coriolis force. However, there is evidence of wavelengths of the order of a planetary scale in the MLT. The previous chapter also shows that the daytime background MLT is a stable and stratified media ($R_i > 1$). This stable media and the rapid rotation of the Earth propitiate the formation of rotational (cyclonic) neutral winds. This rotational characteristic of the winds is always observed in the MLT. Additionally, the Coriolis force generates plasma waves in the *E* region that drive neutral wins. This mechanism could explain enhancements in the amplitudes and shears at around 115 km, observed by the chemical releases, and not explained by tides. The interaction of the Coriolis and Lorentz forces is imprinted in the rotational characteristics of the neutral winds. Examples of reverses in the rotation are presented as an indication of the balance of the two forces.

6.1 Introduction

Neutral winds at *E*-layers heights have been explained in terms of tidal motions (*Mathews* [1998], *Kirkwood and Nilsson* [2000], *Haldoupis and Pancheva* [2006]). Tides can explain the height of the ion layers and the correlated winds. However, characteristics like the direction of the rotation of winds and large-amplitude winds and shears are not totally understood. Observed neutral

wind amplitudes are usually larger than predicted by global circulation models (*Larsen* [2002]), especially in the region between 110 and 120 km where observations show enhancements in the neutral winds correlated with large electron densities. Dynamical studies, like the ones presented in previous chapters, assume a local system (or non-rotating planet) where the neutral winds evolve on a timescale of the order of the Brunt-Väisälä period (few minutes). The force generated by the rotation of the Earth, the Coriolis force, was previously neglected because of its long time scale (few tens of hours).

Studies of the MLT region have shown the presence of waves with periods of the order of a planetary scale. *Eyken et al.* [2000] was the first to find evidence of 8, 12 and 24h planetary waves with the EISCAT Svalbard Radar, at heights between 90-120 km. *Younger et al.* [2002] also showed 8, 12 and 24h tides, using wind estimates from an all-sky meteor radar in Northern Sweden. *Haldoupis* [2011b] observed in the summer of 1993 a 7-day wave with the Rome ionosonde. *Stevens et al.* [2003] and *Yue and Liu* [2010] provide evidence of the presence of planetary waves at MLT-region heights with observations of the water vapor ejected when the space shuttle was launched.

Since the late sixties, *Tolstoy* [1967] has shown that the ionosphere is able to support the propagation of Rossby waves since, for the characteristics of *E*-region ionization, the Coriolis force ($2v_n \times \Omega \sim 10^{-4} v_n/s$) is comparable to the Lorentz force ($\frac{1}{\rho}\mathbf{J} \times \mathbf{B} \sim 10^{-4}(v_i - v_e)/s$). *Mikkelsen et al.* [1981b] and *Mikkelsen et al.* [1981a], using chemical releases and radar measurements, showed that horizontal winds are in geostrophic balance in the direction perpendicular to the electric field momentum forcing. *Larsen and Walterscheid* [1996] included the Coriolis force in the dynamical study of the *E*-region flows to study the balance

between Coriolis and ion drag forces at high latitudes. The waves generated due to the Coriolis force in the ionized medium are known as magnetized Rossby waves (MRW) and have a wavelength of few thousand kilometers, traveling with a phase velocity close to the local neutral winds. These planetary waves drive winds and wind shears efficiently due to a balance between the Earth's rotation and Pedersen- and Hall-conductivity interactions at *E*-layer heights. This is a plausible explanation for high shear neutral velocities at around 115 km.

Kaladze et al. [2004] (also *Kaladze and Tsamalashvili* [1997], *Kaladze and Horton* [2006], *Kaladze et al.* [2007], *Kaladze et al.* [2011], *Kaladze et al.* [2013]) give the theoretical elements for understanding the MRW in the *E*-region at middle latitudes, showing that the electrodynamic ponderomotive forces acting on the rotating plasma generate vorticity in the opposite direction as the Coriolis force propagating westward or eastward (unlike non-magnetized Rossby waves that propagate westward). The direction of propagation depends on the balance between the Coriolis and the Lorentz forces which depends on the height-dependent conductivity in the *E*-region.

The relevance of the Coriolis force is indicated by the Rossby number ($Ro = U/f_\Omega L < 1$), where U is magnitude of the neutral velocity, $f_\Omega = 2\Omega_E \sin\lambda$ is the Coriolis frequency, Ω_E is the Earth's rotation frequency, λ is latitude, and L is the planetary wavelength. The Rossby number is $Ro \lesssim 1$, for standard values of the MLT region over Arecibo, like $U \lesssim 100$ m/s, $L \sim 2 \times 10^3$ km, $\lambda > 20^o$, and $\Omega_E \sim 7 \times 10^{-5}\ s^{-1}$. One of the possible irregularities generated by the Coriolis force is the baroclinic instability which is the mechanism that shapes the cyclones in the atmosphere. Baroclinic instability exists in the presence of rapid rotation (or

$Ro < 1$) and stably-stratified media ($R_i > 1$). From the previous chapter, we observed that values that characterized stable stratification are present during the day. Then, the MLT-region has the conditions needed to seed cyclones which will be moving horizontally over Arecibo.

The main goal of this chapter is to study the rotational properties of the neutral winds (the proxy for cyclones) in the mid-latitude E region over Arecibo as a way to diagnose the magnetized Rossby waves and the unstable equilibrium between the Coriolis and Lorentz forces.

6.2 Basic equations

Electrons, ions, and neutral particles are present in the MLT region. Neutral densities are dominant and create the condition for a weekly ionized medium or $n_e/n_n << 1$, where n_e and n_n correspond to the electron and neutral densities, respectively. The charged particles create a conductive medium, although the dynamics at these altitudes are controlled by the neutral particles, as discussed in previous chapters. The rotation of the Earth affects neutral particles mainly. However, the coupling between the equation of motions for the three species produces an appropriate equation for studying the balance between the Coriolis and the ion drag forces acting in the MLT region. The equations of motion that govern the neutral, ion, and electron particles are:

$$\begin{aligned} \rho\frac{d\mathsf{v}_n}{dt} &= -\nabla p_n - 2\rho\boldsymbol{\Omega}_E \times \mathsf{v}_n + \rho\mathsf{g} + \mu\nabla^2\mathsf{v}_n + m_i n_i \nu_{in}(\mathsf{v}_i - \mathsf{v}_n) \\ &\quad + m_e n_e \nu_{en}(\mathsf{v}_e - \mathsf{v}_n) \end{aligned} \tag{6.1}$$

$$m_i n_i \frac{d\mathsf{v}_i}{dt} = -\nabla p_i + m_i n_i \mathsf{g} + n_i q(\mathbf{E} + \mathsf{v}_i \times \mathbf{B}) - m_i n_i \nu_{in}(\mathsf{v}_i - \mathsf{v}_n) \quad (6.2)$$

$$0 = -\nabla p_e - q n_e(\mathbf{E} + \mathsf{v}_e \times \mathbf{B}) - m_e n_e \nu_{en}(\mathsf{v}_e - \mathsf{v}_n) \quad (6.3)$$

where the subscripts (n, i, e) denote the neutral, ion and electron variables. The Earth's rotation is $\mathbf{\Omega}_E$. These are the same equations presented in equation (2.5) of Chapter 2. Here, the pressure gradient, coriolis, gravitational, viscous, ion and electron drag and dissipative forces are present. Adding the three equations and considering ions in steady state yields:

$$\begin{aligned} \rho \frac{d\mathsf{v}_n}{dt} = & -\nabla(p_i + p_e + p_n) - 2\rho \mathbf{\Omega}_E \times \mathsf{v}_n + \rho \mathsf{g} + \mu \nabla^2 \mathsf{v}_n \\ & + m_i n_i \mathsf{g} + q(\mathbf{E}(n_i - n_e) + (n_i \mathsf{v}_i - n_e \mathsf{v}_e) \times \mathbf{B}) \end{aligned} \quad (6.4)$$

By assuming quasi-neutrality ($n_i \approx n_e$) and neglecting the gravitational effects in the ions (or $\rho / m_i n_i >> 1$) , the expression can be written as follows:

$$\frac{d\mathsf{v}_n}{dt} = -\frac{1}{\rho}\nabla P - 2\mathbf{\Omega}_E \times \mathsf{v}_n + \mathsf{g} + \frac{\mu}{\rho}\nabla^2 \mathsf{v}_n + \frac{1}{\rho}\mathbf{J} \times \mathbf{B} \quad (6.5)$$

were $P = p_n + p_i + p_e$, and $\mathbf{J} = qn(\mathsf{v}_i - \mathsf{v}_e)$. Since the electrons in the E-region are moving in a collisionsless medium ($k_e = \Omega_e / \nu_{en} >> 1$), $\mathsf{v}_e = \mathsf{v}_E = \mathbf{E} \times \mathbf{B}/B^2$. The term $\mathsf{v}_E \times \mathbf{B}$ is the force that balances the Coriolis force to generate the MRWs.

To understand the Lorentz force ($\frac{1}{\rho}\mathbf{J} \times \mathbf{B}$), a moving frame is considered to define the electric field using the transformation (*Jackson* [1975]):

$$\mathbf{E}' = \mathbf{E} + \mathsf{v}_n \times \mathbf{B} = \mathbf{E} + \mathbf{E}_d \tag{6.6}$$

The primed variables are measured in the neutral wind frame. The electric field $\mathbf{E}'$ is related to the dynamo field $\mathbf{E}_d$ and the electric field in the Earth's rotational frame $\mathbf{E}$. Since $\mathsf{v}_n << c$, where c is the speed of light, the magnetic field does not significantly change between the moving and Earth's frame. The electric current associated with the ion-electron motion can be written

$$\mathbf{J} = \sigma \cdot \mathbf{E}' = \sigma \cdot (\mathbf{E} + \mathsf{v}_n \times \mathbf{B}) \tag{6.7}$$

with the conductivity tensor (σ) given by

$$\sigma = \begin{bmatrix} \sigma_P & \sigma_H & 0 \\ -\sigma_H & \sigma_P & 0 \\ 0 & 0 & \sigma_o \end{bmatrix} \tag{6.8}$$

and where the specific (σ_o), the Pedersen (σ_P), and the Hall (σ_H) conductivities are

$$\sigma_o = \frac{nq}{B}(k_i - k_e) \tag{6.9}$$

$$\sigma_P = \frac{nq}{B}\left(\frac{k_i}{1+k_i^2} - \frac{k_e}{1+k_e^2}\right) \tag{6.10}$$

$$\sigma_H = \frac{nq}{B}\left(\frac{k_e^2}{1+k_e^2} - \frac{k_i^2}{1+k_i^2}\right) \tag{6.11}$$

and where k_j is the gyro to collision frequency of the species. To find an expression for the Lorentz force, the current in equation (6.7) is used with the fact $\mathbf{E}_\perp = -\mathsf{v}_e \times \mathbf{B}$ to obtain:

$$\begin{aligned} \frac{1}{\rho}\left(\mathbf{J}\times\mathbf{B}\right)_\perp &= -\frac{B^2}{\rho}\sigma\cdot\left(\mathsf{v}_n-\mathsf{v}_e\right)_\perp \\ &= \frac{B^2}{\rho}\begin{bmatrix} \sigma_P(\mathsf{v}_e-\mathsf{v}_n)_{\perp_N}+\sigma_H(\mathsf{v}_e-\mathsf{v}_n)_{\perp_E} \\ \sigma_P(\mathsf{v}_e-\mathsf{v}_n)_{\perp_E}-\sigma_H(\mathsf{v}_e-\mathsf{v}_n)_{\perp_N} \end{bmatrix} \end{aligned} \tag{6.12}$$

Where the magnetic field $\mathbf{B} = -(+)B\hat{z}$ is vertical and downward (upward) in the northern (southern) hemisphere. The directions perpendicular to the magnetic field northward and eastward are $(_{\perp_N}, _{\perp_E})$ (same notation as equation (2.8)).

6.2.1 Hall and Pedersen conductivity balance

Mikkelsen and Larsen [1983] defined the drag coefficients for the conductivities, derived from the *Lorentz equation* (equation (6.12)):

$$\begin{aligned} \alpha &= \frac{\sigma_P B^2}{f\rho} \\ \beta &= \frac{\sigma_H B^2}{f\rho} \end{aligned} \tag{6.13}$$

where f is the Coriolis force. Assuming steady-state solutions $d\mathsf{v}/dt = o$ and neglecting the gravitational and the viscous forces and the vertical neutral wind component in the equation (6.18), *Larsen and Walterscheid* [1996] obtained:

$$
\begin{aligned}
\mathsf{v}_{\perp E} &= \frac{(1-\beta)u_g + [\alpha^2 - \beta(1-\beta)]\mathsf{v}_{e\perp E} + \alpha(\mathsf{v}_{e\perp N} - v_g)}{\alpha^2 + (1-\beta)^2} \\
\mathsf{v}_{\perp N} &= \frac{(1-\beta)v_g + [\alpha^2 - \beta(1-\beta)]\mathsf{v}_{e\perp N} - \alpha(\mathsf{v}_{e\perp E} - u_g)}{\alpha^2 + (1-\beta)^2}
\end{aligned} \tag{6.14}
$$

Neglecting the vertical wind velocity, the eastward and northward components are $u = \mathsf{v}_E = \mathsf{v}_{\perp E} c\eta - \mathsf{v}_{\perp N} s\eta c\xi$ and $v = \mathsf{v}_N = -\mathsf{v}_{\perp E} s\eta + \mathsf{v}_{\perp N} c\eta c\xi$, respectively, where η and ξ are the zenith and azimuth angles of the magnetic field and "s" and "c" are shorthands for sin and cosine. For the Arecibo location the magnetic angles are $\eta = 346.5^o$ and $\xi = 134.2^o$. The geotropic winds are defined by the pressure gradient terms:

$$
\begin{aligned}
u_g &= -\frac{1}{\rho f}\frac{\partial P}{\partial y} \\
v_g &= -\frac{1}{\rho f}\frac{\partial P}{\partial x}
\end{aligned} \tag{6.15}
$$

For the lower *E*-region, the Hall drag term is dominant ($\beta > \alpha$), and assuming that the geotropic winds are smaller than the plasma winds, the following relations are valid for the *E*-region at mid-latitudes

$$
\begin{aligned}
u &= -\frac{\beta}{(1-\beta)}(\mathsf{v}_{e\perp E} c\eta - \mathsf{v}_{e\perp N} s\eta c\xi) \\
v &= -\frac{\beta}{(1-\beta)}(-\mathsf{v}_{e\perp E} s\eta + \mathsf{v}_{e\perp N} c\eta c\xi)
\end{aligned} \tag{6.16}
$$

The resulting zonal wind is antiparallel to the eastward plasma drift. The meridional wind is parallel to the northward plasma-drift. Small variations in

the eastward plasma-drift induce meridional winds. The northward plasma-drifts also induce zonal winds but on a smaller scale. Including the Coriolis force in the calculations enhances the neutral winds. *Larsen and Walterscheid* [1996] also showed that there is a change in the neutral wind's rotational direction when there is a change in the Hall and Pedersen drag-dominated altitudes.

6.2.2 Coriolis vs Lorentz force

Kaladze et al. [2004] studied the rotational effects of the MRWs. Starting from the definition of the current $\mathbf{J} = qn(\mathsf{v}_n - \mathsf{v}_e)$. The assumption of $\mathsf{v}_n = \mathsf{v}_i$ is used, limiting this analysis to the lower part of the *E*-region. The Lorentz force is:

$$\begin{aligned} \frac{1}{\rho}\left(\mathbf{J}\times\mathbf{B}\right)_{\perp} &= \frac{nq}{\rho}(\mathsf{v}_i\times\mathbf{B} - \mathsf{v}_e\times\mathbf{B}) \\ &= \frac{nq}{\rho}(\mathsf{v}_i\times\mathbf{B} + \mathbf{E}_{\perp}) \end{aligned} \tag{6.17}$$

Rewriting equation (6.18), the *equation of motion* reduces to

$$\begin{aligned} \frac{d\mathsf{v}_n}{dt} &= \mathsf{v}_n\times\left(2\boldsymbol{\Omega}_E + \frac{nq}{\rho}\mathbf{B}\right) + \frac{nq}{\rho}\mathbf{E}_{\perp} \\ &\quad -\frac{1}{\rho}\nabla P + \mathsf{g} + \frac{\mu}{\rho}\nabla^2\mathsf{v}_n \end{aligned} \tag{6.18}$$

Then, the planetary angular rotation vector is affected by the geomagnetic field, creating a magnetized effect that modifies the original Coriolis term as follows:

$$2\boldsymbol{\Omega}_E \;\rightarrow\; 2\boldsymbol{\Omega}_E + \frac{nq}{\rho}\mathbf{B} \tag{6.19}$$

The angular velocity of the Earth's rotation in geographic coordinate system is defined as $\mathbf{\Omega}_E = (0, \Omega_o \cos\lambda, \Omega_o \sin\lambda)$, which is latitude ($\lambda$) dependent.

Using the barotropic potential vorticity, *Holton* [2004] defines the Rossby potential vorticity as

$$\frac{D_h}{Dt} = \left(\frac{\zeta_z + f'}{H}\right) = 0 \tag{6.20}$$

where the horizontal component of the horizontal advective derivative is defined by $D_h/Dt = \partial/\partial t + u\partial/\partial x + v\partial/\partial y$, the vertical component of the vorticity is $\nabla \times \mathsf{v} \cdot z = \zeta_z = \partial v/\partial x - \partial u/\partial y$, the modified Coriolis force in the $\hat{z}$ direction is $f' = f + \gamma = 2\Omega_{oz} + \frac{nq}{\rho}B_z$, the horizontal neutral winds in the east and north direction are u, and v, and the effective height of the E layer is $H \equiv H_o(1+h)$, where H_o is the thickness in stationary state and $h = \Delta H/H_o$ is the perturbation.

Using β-plane approximations in the vicinity of latitude $\lambda = \lambda_o$, the Coriolis parameter is $f = f_o + f'_o y$. The values for f_o and f'_o are positive and defined by:$f_o = 2\Omega_{oz} = 2\Omega_o \sin\lambda_o$ and $f'_o = \partial f/\partial y = \frac{1}{R}\partial f/\partial\lambda = 2\Omega_o \cos\lambda_o/R$. Similarly, the approximation for the geomagnetic contribution is $\gamma = \frac{qn}{\rho}B_z = \gamma_o + \gamma'_o y$, with $\gamma_o = -2qnB\sin\lambda_o/\rho$ and $\gamma'_o = \partial\gamma/\partial y = en/\rho(\partial B_z/\partial y)$, where $\gamma_o < 0$.

Introducing f'_o and γ'_o in equation (6.20), we find:

$$\frac{d\zeta_z}{dt} + (f'_o + \gamma'_o)v - \frac{1}{1+h}[\zeta_z + f_o + \gamma_o + (f'_o + \gamma'_o)y]\frac{dh}{dt} = 0 \tag{6.21}$$

The generalized Rossby parameter corresponding to the Coriolis and Lorentz force contributions is $(f_o' + \gamma_o')$. For the *E*-region, these parameters are of the same order of magnitude but opposite in sign. The Rossby number is also small ($Ro < 1$) for most of the region, so *Kaladze et al.* [2004] assumes geotropic equilibrium to define the geotropic winds:

$$\begin{aligned} u &= -\frac{g}{f_o + \gamma_o}\frac{\partial \Delta H}{\partial y} \\ v &= \frac{g}{f_o + \gamma_o}\frac{\partial \Delta H}{\partial x} \end{aligned} \tag{6.22}$$

Consequently, the vorticity and the derivative are

$$\begin{aligned} \zeta_z &= \frac{g}{f_o + \gamma_o}\nabla^2(\Delta H) \\ \frac{d}{dt}\zeta_z &= \frac{gH_o}{f_o + \gamma_o}\frac{\partial}{\partial t}(\nabla^2 h) + \left(\frac{gH_o}{f_o + \gamma_o}\right)^2 J(h, \nabla^2 h) \end{aligned} \tag{6.23}$$

where J is the Jacobian. Using this expressions in equation (6.21) and neglecting high order terms, the generalized equation for magnetized Rossby waves is found:

$$\frac{\partial}{\partial t}\left(\nabla^2 h - \frac{1}{r_R^2}h\right) + (f_o' + \gamma_o')\frac{\partial h}{\partial x}(1+h) + \frac{gH_o}{f_o + \gamma_o}J(h, \nabla^2 h)(1+h) = 0 \tag{6.24}$$

where the barotropic Rossby-Obukhov radius is:

$$r_R(y) = \left[\frac{gH_o}{(f + \gamma)(f_o + \gamma_o)}\right]^2 \tag{6.25}$$

Assuming an oscillatory perturbation a dispersion equation can be obtained from equation (6.24):

$$\omega = -\frac{k_x(f_o' + \gamma_o')}{k_x^2 + k_y^2 + \frac{1}{r_R^2}} \tag{6.26}$$

The magnetized Rossby wave propagates with a wave frequency ω in the horizontal direction (k_x, k_y) with a velocity $v_R \equiv \omega/k_x$. The balance between the Coriolis and the Lorentz force or the generalized Rossby parameter $(f_o' + \gamma_o')$ controls the direction of the rotation. When the Rossby wave moves westward for $(f_o' + \gamma_o' > 0)$, the rotation is anti-cyclonic in the northern hemisphere. When the wave moves eastward, the rotation is cyclonic (Figure 6.1).

6.3 Observations

Neutral wind profiles are estimated from the data collected in Word Day campaigns with the Arecibo ISR, as described in previous chapters. These Arecibo ISR observations show that the winds are rotational at MLT region heights and have high shear between 100 and 115 km, in agreement with previous observations (*Hysell et al.* [2012]), rocket campaigns (see *Larsen et al.* [1998] and references therein) and meteor trail observations (*Drummond et al.* [2001]).

To study the rotational characteristics of the winds, a standard hodograph plot is used, where the horizontal axis corresponds to the zonal and the vertical to the meridional wind (See Figures 6.2 - 6.6). Every hodograph corresponds to a vertical profile over Arecibo for a particular time. When combining the profiles together, the variation of the neutral wind rotation pattern in the northern

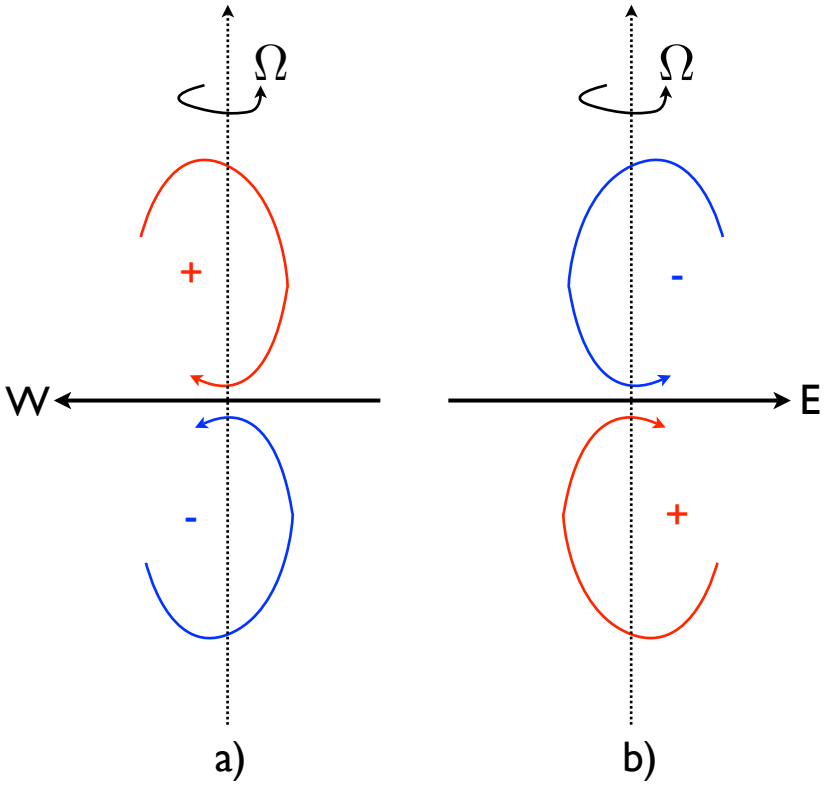

Figure 6.1: Rotation patterns when the magnetized Rossby wave is propagating a) westward, b) eastward. In the northern hemisphere, the rotation is a) anti-cyclonic (red and +) and b) cyclonic (blue and -). In the southern hemisphere, the rotation is the opposite a) cyclonic, b) anti-cyclonic. The rotation of the winds (ω) and direction of propagation (v_R) are controlled by the balance between the Coriolis and Lorentz force ($f'_o + \gamma'_o > 0$) (See equation (6.26)). See text for explanation.

hemisphere is observed since the supposed Rossby wave is propagating close to the zonal direction.

The general tendency for the observed neutral winds is to have a closed elliptical shape rotating anti-cyclonically. The profiles shown here have an anti-cyclonic rotational characteristic with a few exceptions (see Figure 6.2 at 42.7 h). This tendency for anti-cyclonic rotation is also reported by (*Hysell et al.* [2012]). The total change of rotational direction at all heights (or opposite to previous ob-

servations) can be interpreted as a change in the sign of the Rossby parameter ($\gamma_o' + f_o'$). Kaladze's theory correlates the sign changes in the Rossby parameter and the propagation direction of the Rossby waves when the geomagnetic field overcomes the Coriolis force.

The dimension of the observed neutral winds varies between $\pm 50 - \pm 150$ m/s. There was no profile with maximum velocity less than $|50|$ m/s in every horizontal direction. However, every profile is unique. Many of them are not closed loops and have small wiggles in the opposite direction (p.e. Figure 6.2 at 16.49 h). Others start rotating in one direction and reverse at higher altitudes (p.e. Figure 6.2 at 15.82 h). These changes could be an indication of the unstable equilibrium between the Coriolis and Lorentz forces.

A frequent feature (but not the general case) is the change in direction of rotation in small altitude segments (see Figure 6.2 at 32.69 h) or Figure 6.4 at 81.2 h). Here at lower altitudes, the winds rotate in one direction while at higher heights, winds rotate in the opposite direction. These changes could be related to the transition from Hall to Pedersen conductivity-dominated heights as indicated by Larsen's theory.

6.4 Discussion

Previous analysis of the neutral dynamics in the MLT region was done in a planar context, neglecting the Coriolis force. However, planetary waves are present in the atmosphere at all height ranges. At MLT-region altitudes, evidence of these waves is shown in observations of water vapor transport from the shuttle engines (*Stevens et al.* [2003]) and observations of waves with periods longer

than a few tens of hours. The Rossby number for the MLT region is $Ro < 1$, which, added to the presence of high Richardson numbers $R_i > 1$ (see Chapter 5), propitiates the conditions to generate cyclones-type irregularities due to Coriolis effects, and in a long-wavelength scale.

Neutral-wind observations at *E*-region heights are characterized by rotational behavior and large shears between 105 km - 115 km. Gravity waves and tidal effects are not able to generate such large winds and shears. Consequently, general circulation models, like the Horizontal Wind Model (HWM), underestimate the observations. It seems that large-wavelength waves are responsible for the differences between the local models and the observations (*Larsen and Fesen* [2009], *Liu* [2007]). *Larsen and Walterscheid* [1996] (and references therein) and *Kaladze et al.* [2004] (and references therein) included the Coriolis force in dynamics studies of the MLT region. Larsen studied the transition between areas governed by Hall and Pedersen conductivities to showed that changes in characteristics depending on height were related to gradually magnetized particles effect. He explained the wind enhancement due to a balance between the Coriolis parameter and the Hall drag coefficient, creating a zone with higher shears below. Kaladze studied the linear and non-linear Coriolis - Lorentz force interaction. He proposed a general dispersion relationship that we use here to study the rotational characteristics of the neutral winds.

Large shears and variations in rotation directions are explained by introducing the Coriolis force in the dynamic studies of the MLT region. The observed neutral winds show evidence of a transition between unmagnetized and magnetized species, as predicted by Larsen's theory. Change in the rotational direction in narrow altitude segments is frequently observed. Also, variations in the

rotation of the full profile are sparse but present. The balance between Coriolis and Lorentz forces ($f_o' + \gamma_o'$) is altered when the geomagnetic field substantially modifies the planetary angular rotation vector. For an unmagnetized medium ($\gamma_o' \sim 0$), the Rossby parameter is positive ($f_o' + \gamma_o' > 0$), and the Rossby wave moves westward with an anti-cyclonic rotation in the northern hemisphere, as is the case for most of the Arecibo observations. In the presence of a strong vertical magnetic gradient, the Rossby parameter is ($f_o' + \gamma_o' < 0$), the wave moves eastward, and the rotation is cyclonic. This could be the explanation for the rotational change in the complete wind profile.

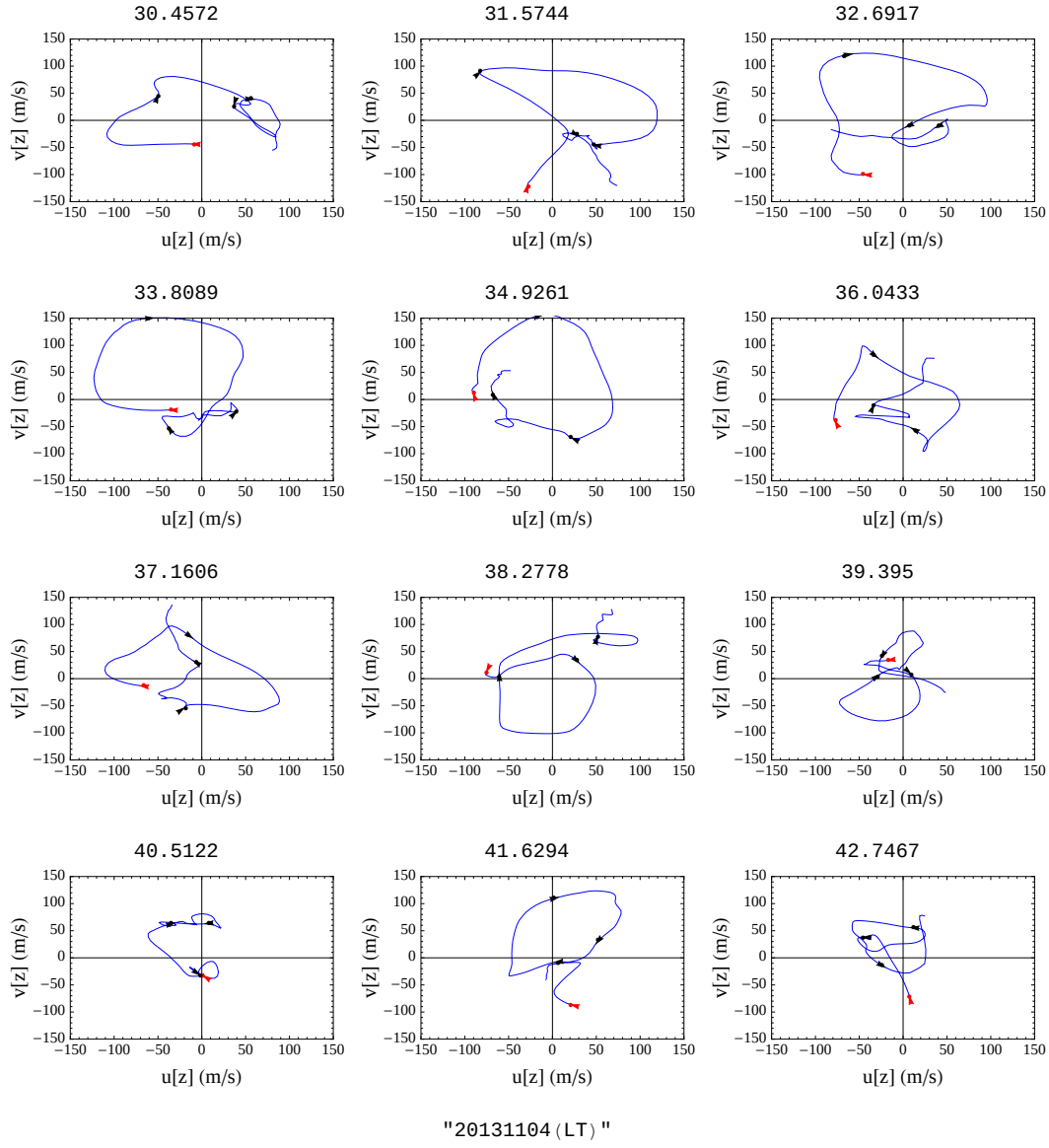

Figure 6.2: Hodographs (planar representations) of the vertical variation of the neutral winds for the observations of the first day in the campaign of November 4, 2013. The profiles were taken approximately every hour. The horizontal axis is the zonal and the vertical is the meridional wind. The red arrow indicates the lower height at 98 km. The black arrows depict the heights 105, 115 and 125 km. Twelve profiles are presented for each day, spaced uniformly. Every profile is unique. The profile's features reflect the balance between Coriolis and Lorentz force as well as transitions between areas governed by Hall and Pedersen conductivities. (See text).

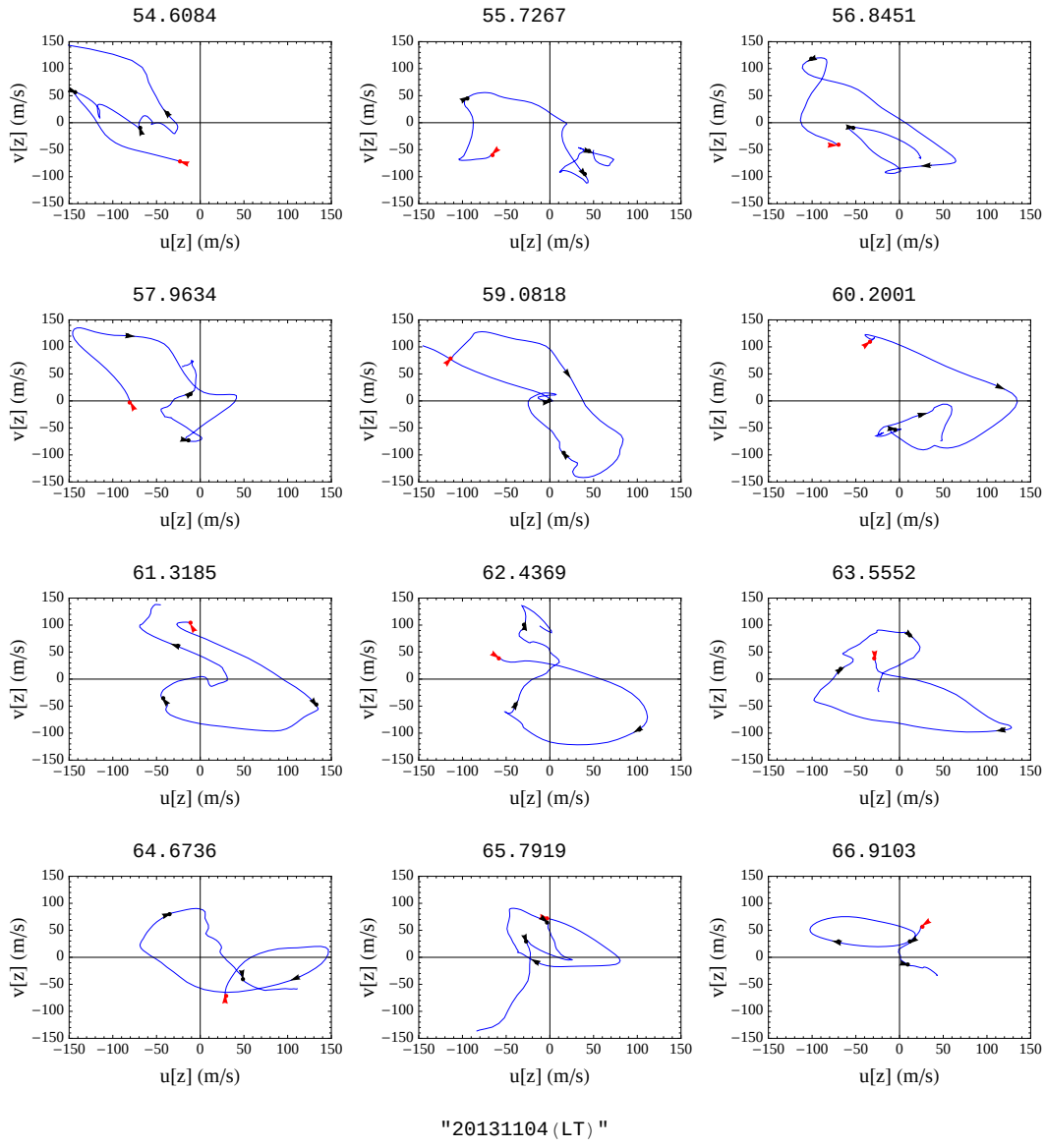

Figure 6.3: Hodographs for the observations of the second day in the campaign of November 4, 2013. The profiles were taken approximately every hour. See general description of the plots in Figure 6.2.

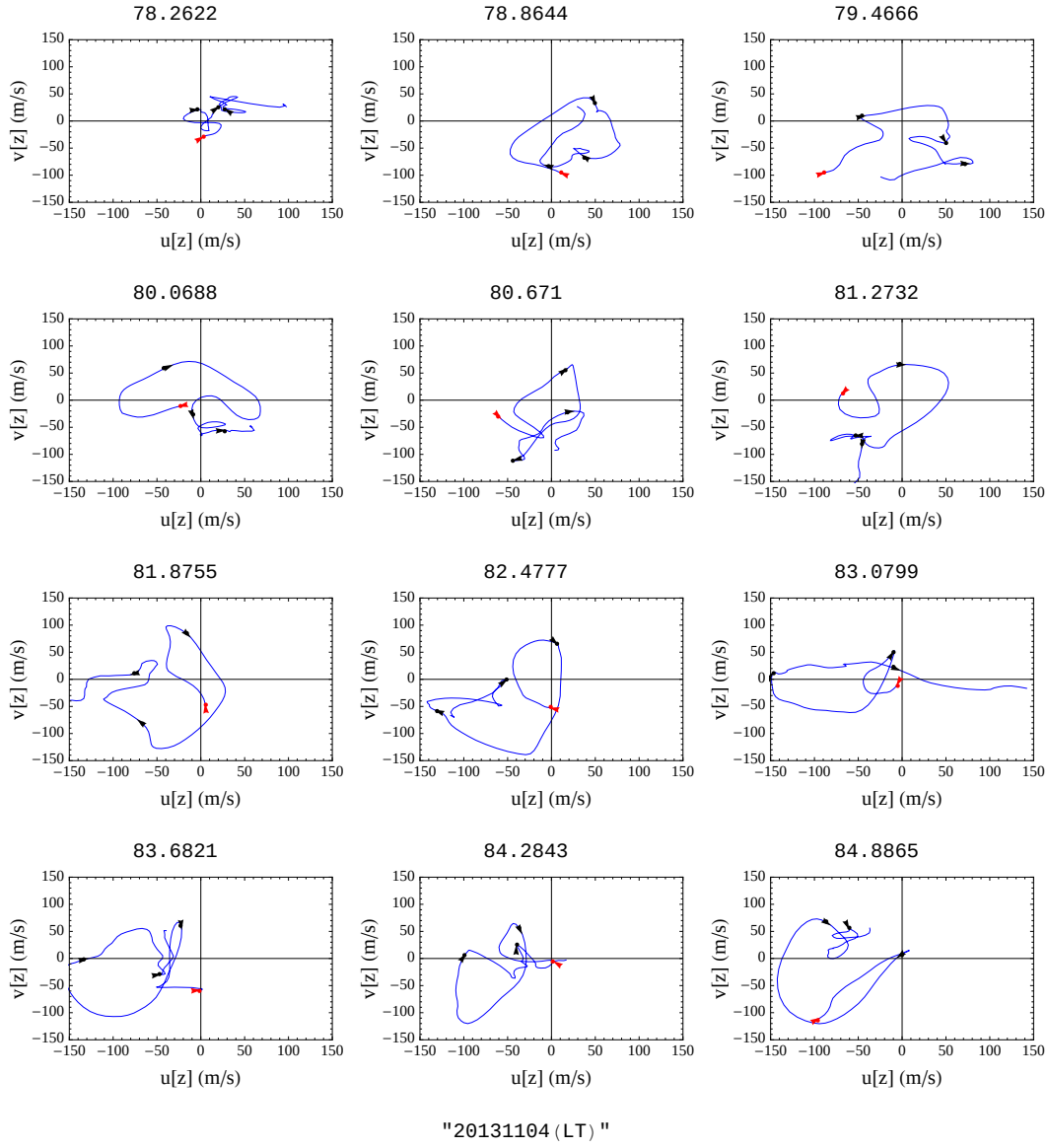

Figure 6.4: Hodographs for the observations of the third day in the campaign of November 4, 2013. The profiles were taken approximately every half hour. See general description of the plots in Figure 6.2.

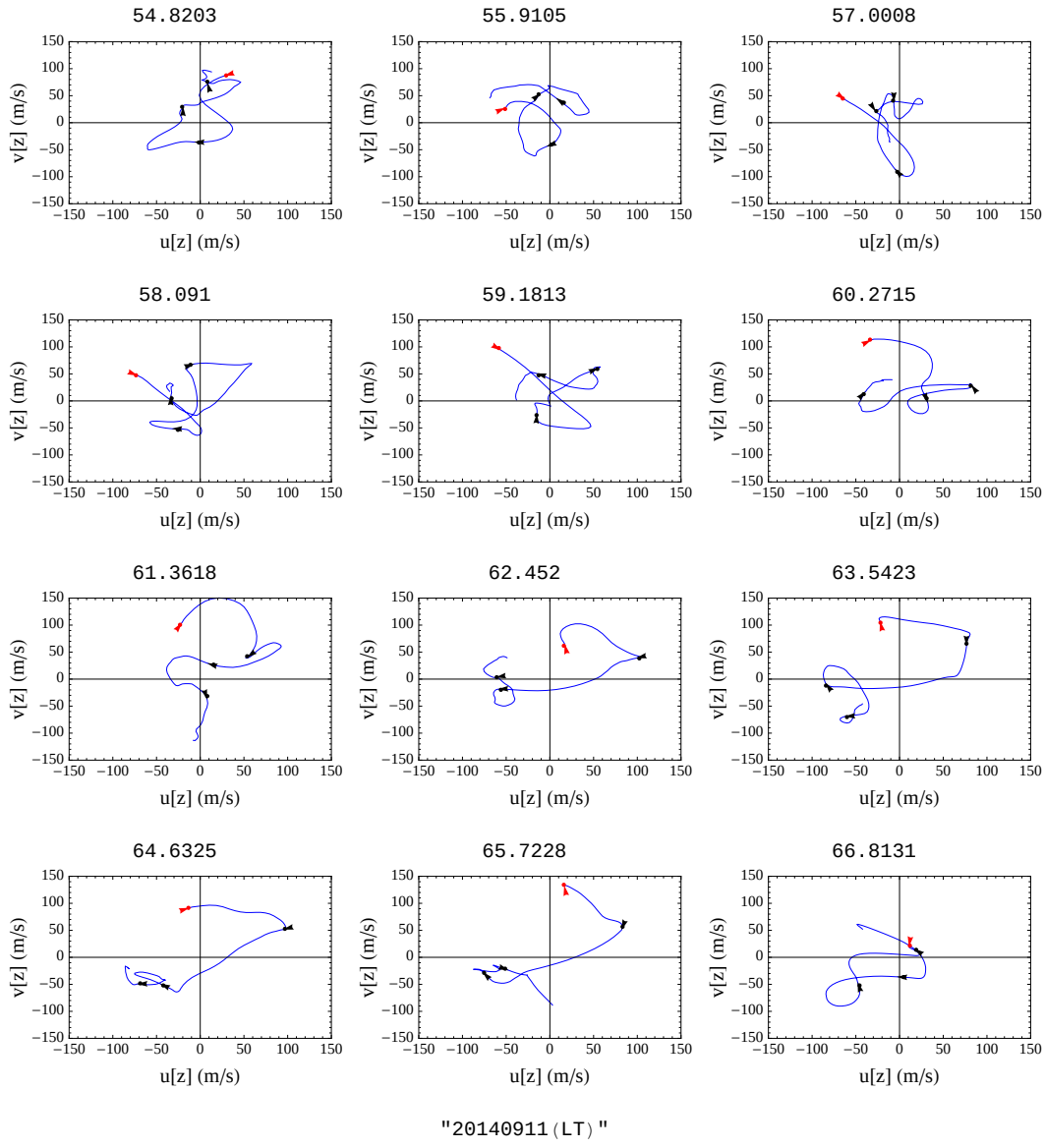

Figure 6.5: Hodographs for the observations of the second day in the campaign of September 11, 2014. The profiles were taken approximately every hour. See general description of the plots in Figure 6.2.

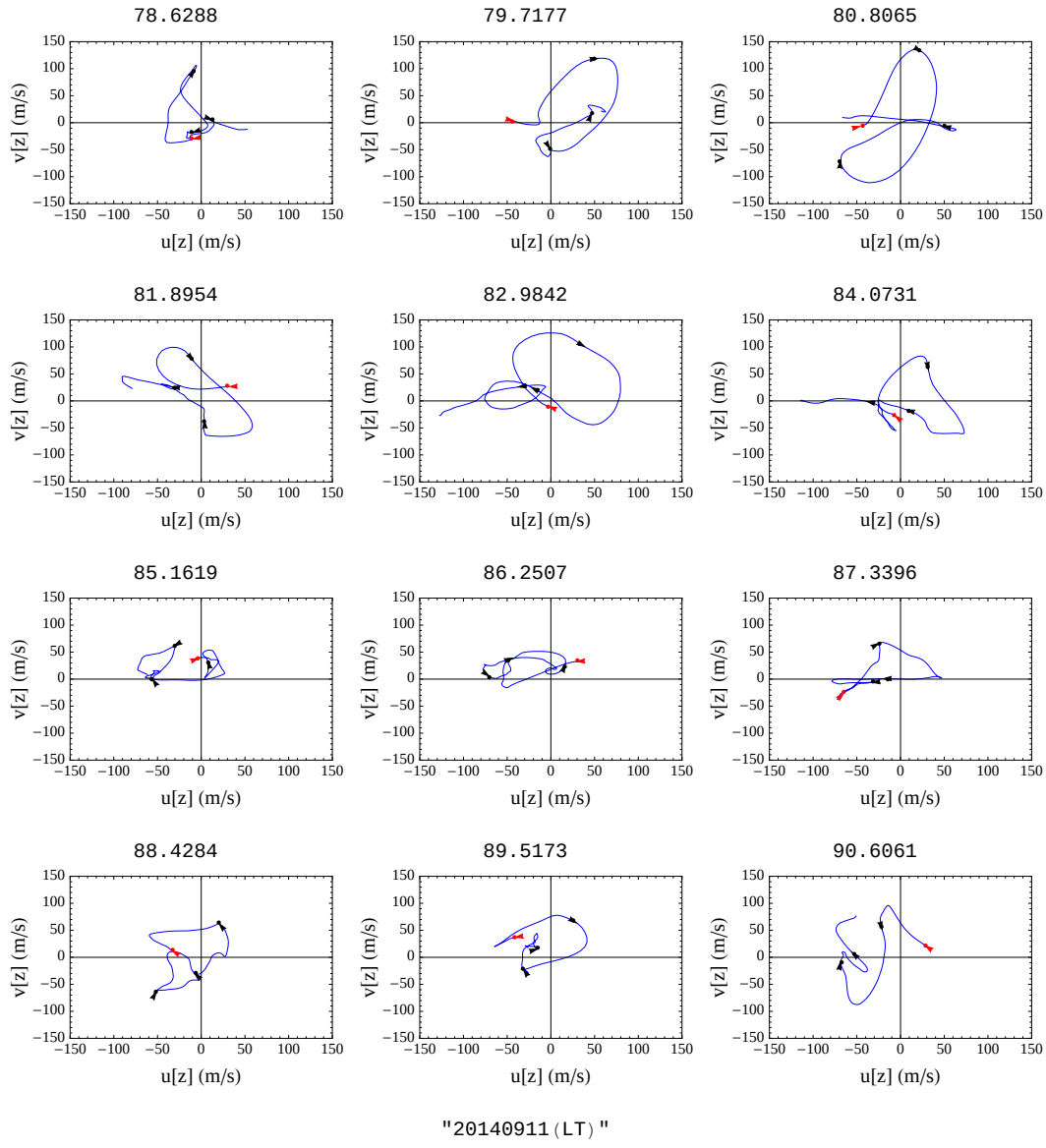

Figure 6.6: Hodographs for the observations of the third day in the campaign of September 11, 2014. The profiles were taken approximately every hour. See general description of the plots in Figure 6.2.

7

NIGHTTIME DYNAMIC INSTABILITIES AT MID-LATITUDE

"There was no moon. The sky above our heads was inky black. But the sky on the horizon was not dark at all. It was shot with crimson, like a splash of blood. And the ashes blew towards us with the salt wind from the sea."

– Daphne du Maurier, *Rebecca*

Nocturnal variations in sporadic E_s layers have been the central point of study for mid-latitude E layers. Patchy and broken ion layers originate disruptions in radio communications. The summary presented in this chapter shows an analysis of the nocturnal events characterized by strong neutral winds and large polarization electric fields. The results are published by *Hysell et al.* [2009], *Hysell et al.* [2011], and *Hysell et al.* [2012]. Billow events associated with QP echoes are unstable under the Richardson number criteria. An eigenvalue analysis of the neutral model of *Miles* [1961] and *Howard* [1961] show that two kinds of growing solutions can coexist in an observed E_s coherent scatter echoes. The solutions are slow and fast and are propagating in different directions. For some modes, bifurcation of the layer is possible. The characteristics found here match the observations and support the theory that QP echoes a produced by the shear velocity force of the neutral winds in the MLT region.

7.1 Quasi periodic coherent scatter echoes

The nocturnal E layer has been used for radio communications starting with Marconi in the early 1900's. Since then, the irregular nature of the layer has intrigued many scientists. Drastic changes in ion density, often of many orders of magnitude, are frequently observed. These layers are known as sporadic E_s and can be seen over large geographic areas of the order of thousands of kilometers.

During a dense E_s event, *Yamamoto et al.* [1992] detected coherent scatter radar echoes at frequencies corresponding to wavelengths of a few meters. Those echoes are called "quasi-periodic" (QP) because of their almost periodic structure in range-time-Doppler-intensity (RTDI) plots as seen in Figure 7.1. Rocket experiments (e.g. *Fukao et al.* [1998], *Larsen et al.* [1998], *Yamamoto et al.* [2005], *Bernhardt et al.* [2005] and references therein) always observed QP events with dense E_s and in the presence of strong polarization fields and sheared neutral winds.

To analyse QP echoes, a 30 MHz coherent scatter radar was deployed in St. Croix looking perpendicular to **B** over Arecibo at around 105 km. Observations were performed during September 2008 and reported by *Hysell et al.* [2009]. The event presented in Figure 7.1 is delineated by echoes organized along fronts with periods between 5-15 min. The event shown in Figure 7.2 and similar cases are characterized by echoes usually propagating towards the southwest or northeast with a speed of few tens of meters per second and wavelengths of a few tens of km. These events usually last for about one hour.

Researchers have explored many theories that could explain irregularities in

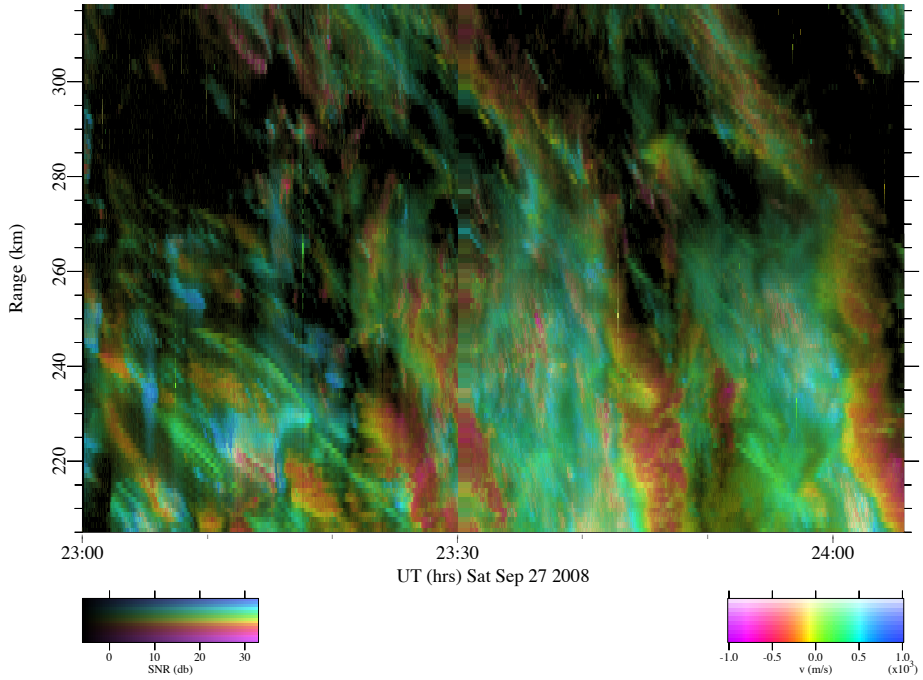

Figure 7.1: RTDI plot of coherent scatter observed by the St. Croix radar on September 27, 2008. UT = LT + 4h. The brightness, hue, and saturation of the pixels represent the signal-to-noise ratio, Doppler shift, and spectral width of the echoes.

the plasma that could generate the QP echoes. *Woodman et al.* [1991] proposed that gravity waves could modulate the E_s layer. *Tsunoda et al.* [1994] attributed the polarization induced by atmospheric gravity waves as an explanation of some of the irregularities in the E_s layers. However, rockets or radar experiments have not been able to observe such events. Later *Didebulidze and Lomidze* [2010] and *Chu et al.* [2011] proposed gravity waves as precursors of the echoes.

Cosgrove and Tsunoda [2001], *Tsunoda and Cosgrove* [2001] and references therein have attributed QP echoes to closed-current dynamo structures between the *E*- *F* layer. Apparent similarities between medium-scale traveling ionospheric disturbance (MSTIDs) in the *F* layer and the QP echoes are cited as

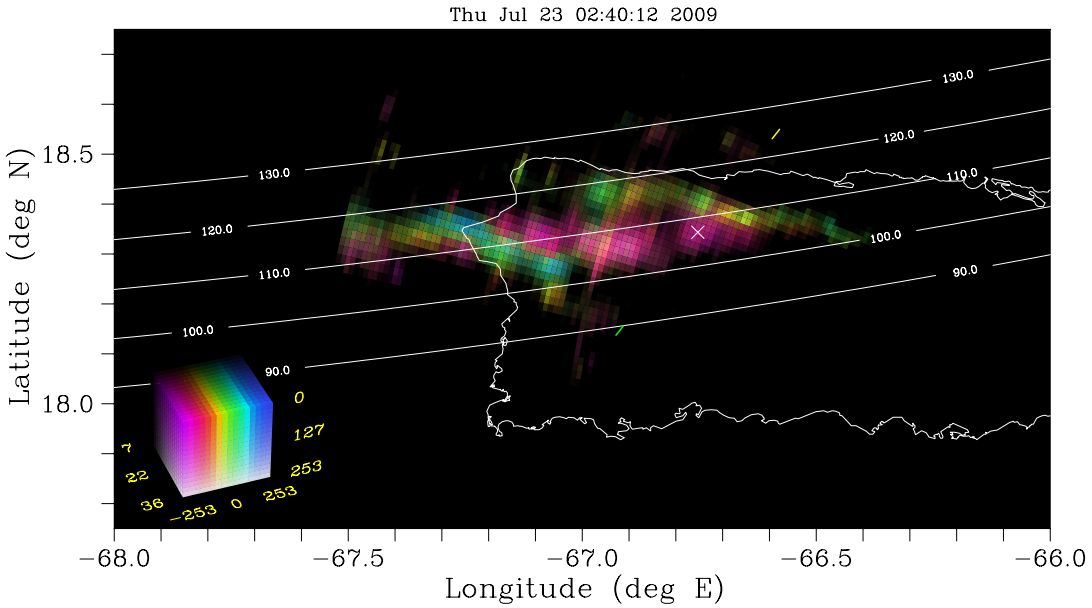

Figure 7.2: Coherent scatter echoes observed over the island of Puerto Rico by the St. Croix radar on July 23, 2009 at 2:40 UT. Similar echoes were observed for the same time as the previous figure (see *Hysell et al.* [2009]). The brightness, hue, and saturation of the pixels represent the signal-to-noise ratio, Doppler shift, and spectral width of the echoes. The white lines show the radar loci of perpendicularity at the specific height. The location of Arecibo Observatory is indicated with an "x".

support for this theory. However, the scale sizes and directions of propagation differ for the two phenomena (see Table 7.1 for comparison of simultaneous observations presented by *Hysell et al.* [2011]).

The most accepted theory that explains QP echoes is dynamic instabilities generated due to strong neutral winds that create the appropriate conditions to overcome the buoyancy force and disrupt the stratification. *Larsen* [2000b] suggested that the high shears present during the events could lead to Kevin-Helmholtz irregularities originating the meter scale instabilities that create QP echoes. ISR observations show power profile where it is easy to see billowy ion layers (see Figure 7.3, first panel) at the same time that QP echoes are registered

	QP	MSTIDs
Region	*E*	*F*
Period	5-15 min	about 1 h
Wavelength	tens of km	hundreds of km
Propagation speed	tens of m/s	hundreds of m/s
Propagation direction	SW or NE (northern hemisphere)	SW (northern hemisphere)
Time scale	about 1h	tens of h
Fronts alignment		NW-to-SE (northern hemisphere) SW-NE (southern hemisphere)

Table 7.1: QP and MSTID characteristics. Airglow images from Boston University all-sky imager show the apparent similitudes and differences between the two events. Airglow image of a MSTID event can be seen in *Hysell et al.* [2011], Figure 19.1. Airglow for QP echoes can be found in *Hysell et al.* [2012], Figure 6.

with the coherent radars. Observations and analysis of the wind shear theory will be explored in the following sections.

7.2 QP echoes and dynamically unstable regions

The Arecibo ISR detected billow activity (see the first panel of Figure 7.3) for the night that the echoes shown in Figure 7.1, indicating the possible presence of dynamic instability. *Miles* [1961] and *Howard* [1961] establish the Richardson number ($R_i < 1/4$) as the necessary condition to develop dynamic instabilities of the Kevin-Helmholtz kind (see Chapter 5). Temperatures and winds have to be estimated to calculate the R_i number (see equation (5.8)).

For the event, *Hysell et al.* [2009] estimate the horizontal components of the ion drifts using a regularization method and temperatures assuming a composition for the nocturnal *E*-layer of heavy and light metallic ions to fit the autocorrelation function (third to fifth panels of Figure 7.3). Strong meridional winds of more than 100 m/s were observed with high-velocity shears below 105 km altitude. The values of temperature are in the same range of values as those measured by the K lidar for the campaign (see Figure 7.4 for September 29, 2008), though weather conditions limited the lidar observations on the night of September 27.

The Brunt-Väisälä frequency and the R_i number were calculated by *Hysell et al.* [2009], assuming thermal equilibrium and neutral winds equal to ion drifts. Figure 7.3 shows the estimates for the event of September 27, 2008. Evidence of dynamic instability as a source of QP echoes was found. Values of $R_i < 1/4$ are frequently found for the lower *E* layer heights at the same time as observed billow activity in the E_s layer.

7.3 Eigenvalue analysis

Previous analysis shows Richardson numbers of the order required to fulfill the necessary condition to develop dynamic instability. The eigenvalue model by *Miles* [1961] and *Howard* [1961] (see equation (5.5)) was used by *Hysell et al.* [2012] to find the propagating modes for rotational winds inspired by an event where Kelvin-Helmholtz activity was suspected. This was the first time that calculations of eigenmodes for rotational winds in the MLT region was performed.

The characteristics of the variables used to perform the eigenvalue analy-

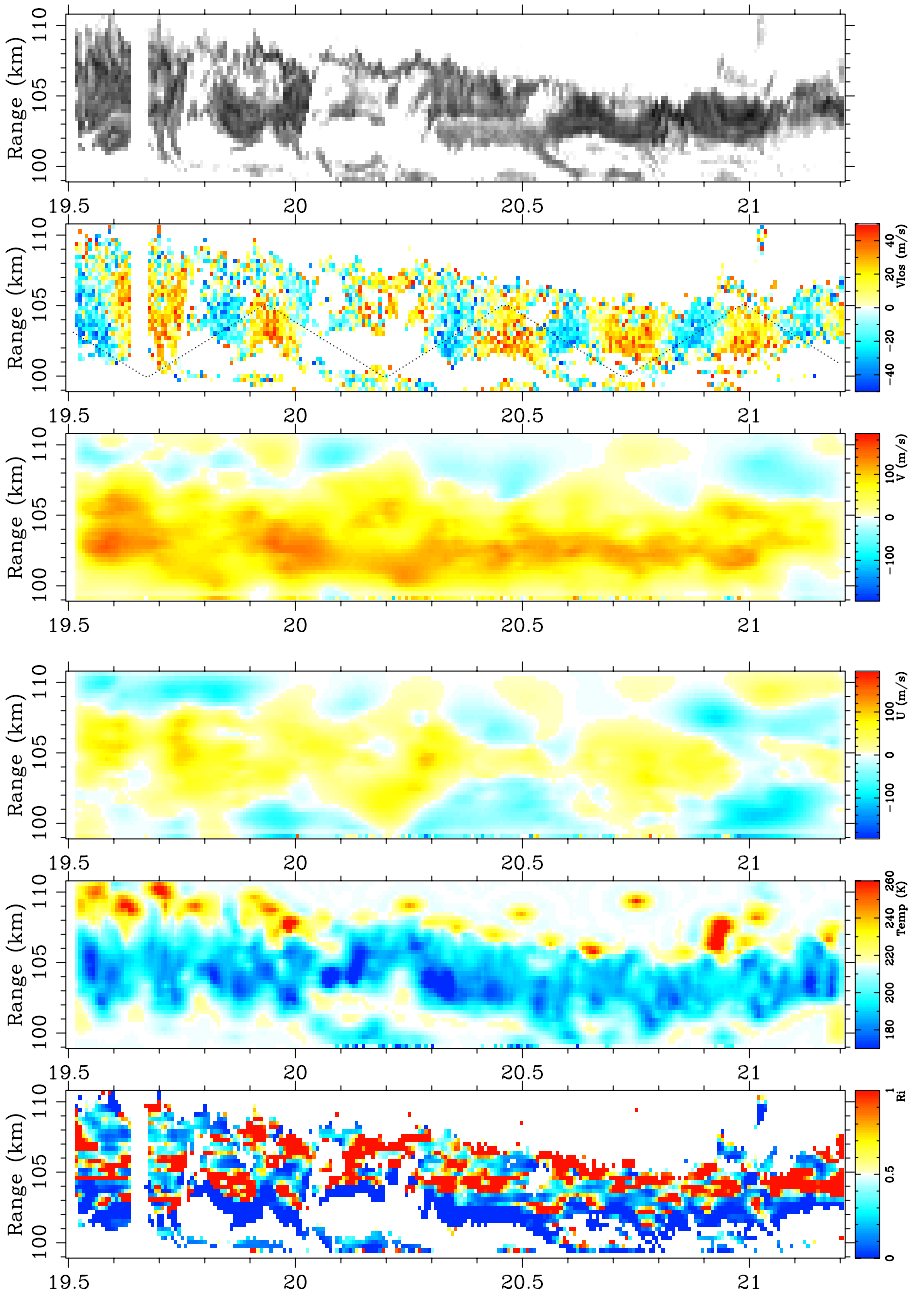

Figure 7.3: Arecibo ISR observations of power and ion drifts, and estimates for the horizontal neutral winds (U and V), temperature, and Richardson number for September 27, 2008 LT. Dynamic instability conditions ($R_i < 1/4$) are present at the bottom of the layer and depicted with dark blue color. After *Hysell et al.* [2009]

sis were obtained from Arecibo observations on the night of July 2, 2010. The buoyancy period was 5 min. The wind profile characteristics were rotational, anti-cyclonic, elongated in the meridional direction, translated 25 m/s toward the west in the zonal direction, and with the shear peak between 110 and 115 km altitude. The Richardson number associated with the neutral winds (top left of Figure 7.5) showed two unstable layers in the Richardson number sense. The lowest value of the Richardson number profile was caused by the meridional shear.

The Miles and Howard eigenvalue model was numerically solved for altitudes between 105 - 120 km altitude. The results are presented in the right panels of Figure 7.5. Slowly growing solutions were found for small k_x and $0.2 < |k_y| < 0.3$ equivalent to wavelengths between 20-30 km, moving southward at $\approx$ 50 m/s with a growth time of a few minutes. These characteristics seem to match Kelvin-Helmholtz events. The mode shape depicted in the left (of the top right panel) was associated with this kind of solution. The functions seemed to discriminate two different unstable stratifications.

Fast growing solutions were also found with growth times as short as about a minute for larger k_x and $|k_y|$ with equivalent wavelengths between 10-15 km and propagating southwest at $\approx$ 50 m/s. The mode shapes had two peaks (center and right), perhaps indicating a bifurcation of the layer like the event observed by Arecibo ISR on September 29, 2008, after 21.5 h (LT) (see Figure 7.4).

The results from the analysis explain the variability of the propagating directions of the QP echoes within the southward direction, which matches the observations from the coherent scatter radar deployed in St. Croix. For the

studied wind profile, two very distinctive growing solutions were detected. Waves with wavelengths between 20 - 30 km were slow growing and propagating southwards. Waves with wavelengths between 10-15 km were fast growing and propagating southwest.

7.4 Summary

During the night at *E*-region heights, the ionized region is confined to descendant-ion layers that are associated with high-velocity shear. For large values of shear, the Richardson number is less than 0.25, in the regime of the necessary conditions to develop dynamic instabilities.

Observations made with the ISR at Arecibo show billowy behavior and bifurcated layers associated with the coherent echoes registered with the radar located in St. Croix and looking the same *E*-region volume as Arecibo. Characteristics like rolls, bifurcated layers can be present in the context of dynamic instability when Kelvin-Helmholtz rolls are formed.

The QP echoes registered with the coherent radars have a wide spectrum of characteristics that are limited by the direction of propagation between south and southwest or northeast and north directions with periods between 5-15 min, growing in order of minutes with wavelengths between 10-50 km. The resemblance of the QP-echoes seems very similar to other phenomena like MSTID, present at *F*-layer heights. Closed currents between the *E* and *F* layer was supported in the assumption of this similarities. However, the characteristics of MSTIDs differ from QP echo events.

A more comprehensive explanation of the diverse range of QP-echoes characteristics is done by an analysis of the eigenvalue solutions for the dynamic instability problem equations. Results showed that many modes can be present at the *E*-layer heights. The rolls and the layer bifurcation are explained by a particular solution. The Kelvin-Helmholtz rolls are associated with an eigenfunction, with growing time $\sim$ 5 min, propagating southward with wavelengths between 20-30 km. Eigenfunctions associated with the layer bifurcation are fast growing in order of one minute, propagating southwest with 10-15 km wavelength.

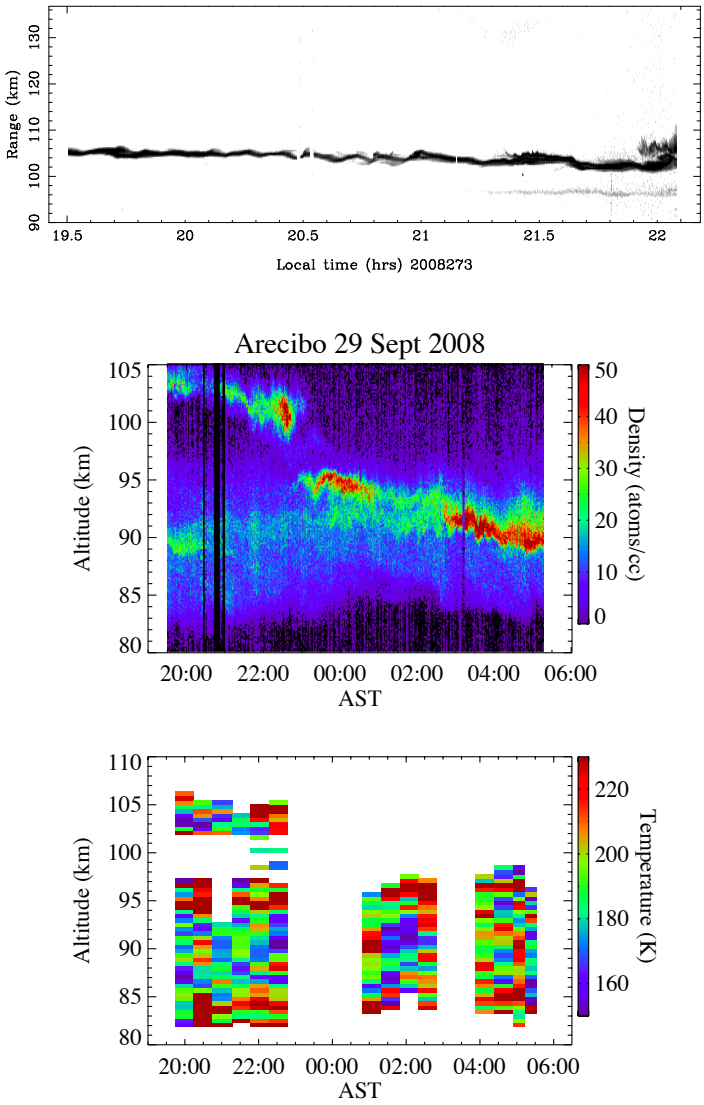

Figure 7.4: Lidar observations for K density and temperature profiles for September 29, 2008 (Local time) at Arecibo Observatory. Top panel: Arecibo ISR power profile. Ion layer activity (top panel) resemble the neutral layers observed by the K lidar (second panel). A bifurcation event is observed, perhaps related to dynamic instability. The third panel corresponds to the Temperature profile obtained with the K Lidar observations. Figure courtesy of Jonathan Friedman from Arecibo Observatory. The Arecibo Observatory is operated by a consortium, led by SRI International and including the Universities Space Research Association and Universidad Metropolitana, under a cooperative agreement with the National Science Foundation. The data presented here was obtained when Arecibo was managed by Cornell University.

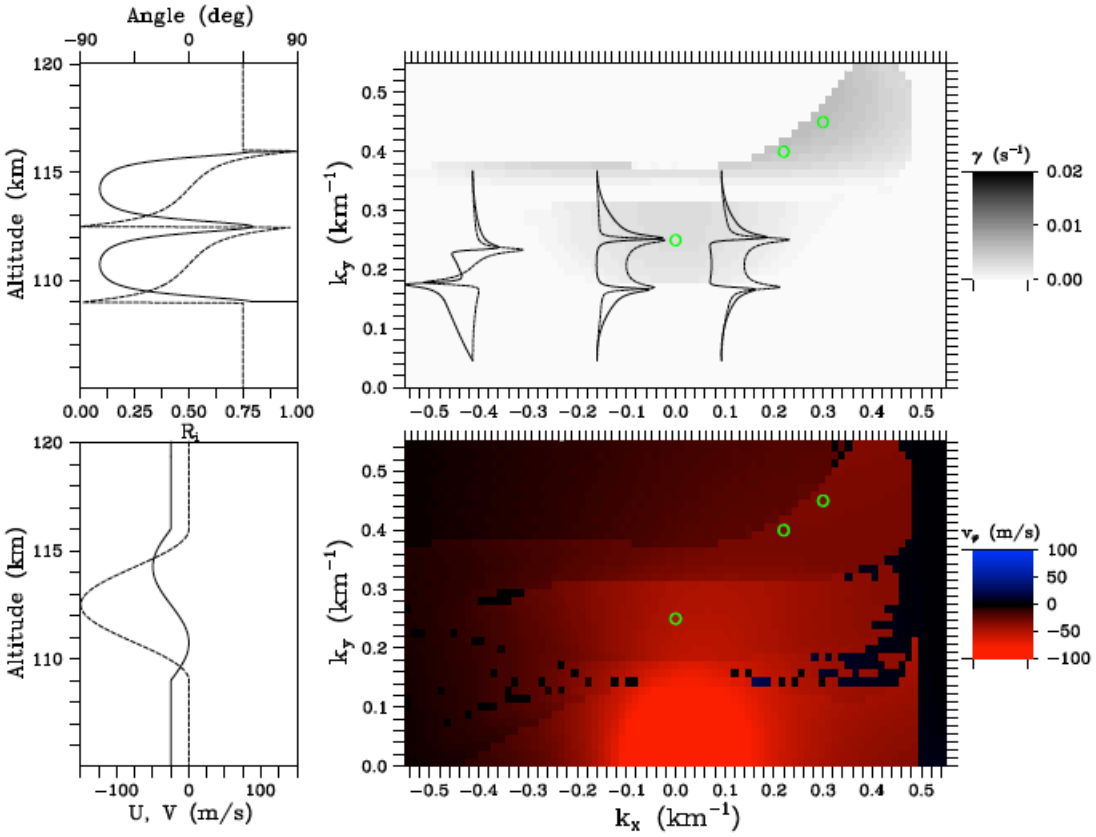

Figure 7.5: Eigenvalue analysis for winds inspired by Arecibo ISR observations, when Kelvin-Helmholtz was suspected. The wind profiles for the zonal (continuous) and meridional (discontinuous) components are found on the bottom left panel. The associated R_i number are depicted in the top left panel for both components. The resulting growth rate versus the horizontal wave vector is shown on the top right. The three functions corresponds to the modes of the green dots areas. The Phase speed versus horizontal wave vector is depicted in the bottom right panel. After *Hysell et al.* [2012]

8

BIBLIOGRAPHY

BIBLIOGRAPHY

Aster, R. C., B. Borchers, and C. H. Thurber, *Parameter Estimation and Inverse Problems*, Elsevier, New York, 2005.

Axford, W. I., The formation and vertical movement of dense ionized layers in the ionosphere due to neutral wind shears, *J. Geophys. Res.*, *68 No. 3*, 1963.

Baggaley, W., Seasonal characteristics of daytime es occurrence in the southern hemisphere, *Journal of Atmospheric and Terrestrial Physics*, *47*(6), 611 – 614, doi: http://dx.doi.org/10.1016/0021-9169(85)90044-3, 1985.

Balmforth, N. J., and P. J. Morrison, A necessary and sufficient instability condition for inviscid shear flow, *Studies in Applied Mathematics*, *102*(3), 309–344, doi:10.1111/1467-9590.00113, 1999.

Bernhardt, P., J. Werne, and M.F.Larsen, Modeling of sporadic-e structures from wind-driven kelvin-helmholtz turbulence, *In Characterising the Ionosphere., Meeting Proceedings RTO-MP-IST-056, Paper 34. Neuilly-sur-Seine, France: RTO*, (34–1 – 34–14), available from: http://www.rto.nato.int/abstracts.asp., 2006.

Bernhardt, P. A., The modulation of sporadic-e layers by kelvin-helmholtz billows in the neutral atmosphere, *Journal of Atmospheric and Solar-Terrestrial Physics*, *64*, 1487–1504, doi:10.1016/S1364-6826(02)00086-X, 2002.

Bernhardt, P. A., et al., Radio tomographic imaging of sporadic-e layers during seek-2, *Annales Geophysicae*, *23*(7), 2357–2368, doi:10.5194/angeo-23-2357-2005, 2005.

Briggs, B. H., The analysis of spaced sensor records by correlation techniques, *MAP Handb.*, *13, 166-184*, 1984.

Brown, L. B., A. J. Gerrard, J. W. Meriwether, and J. J. Makela, All-sky imaging observations of mesospheric fronts in oi 557.7 nm and broadband oh airglow emissions: Analysis of frontal structure, atmospheric background conditions, and potential sourcing mechanisms, *Journal of Geophysical Research: Atmospheres*, *109*(D19), doi:10.1029/2003JD004223, d19104, 2004.

Brunt, D., The period of simple vertical oscillations in the atmosphere, *Quarterly Journal of the Royal Meteorological Society*, *53*(221), 30–32, 1927.

Chandrasekhar, S., *Hydrodynamic and Hydromagnetic Stability*, Clarendon, Oxford, 1961.

Charney, J., The dynamics of long waves in a baroclinic westerly current, *J. Meteor.*, *4*, 135–163, 1947.

Chu, X., C. S. Gardner, and S. J. Franke, Nocturnal thermal structure of the mesosphere and lower thermosphere region at Maui, Hawaii (20.7N), and Starfire Optical Range, New Mexico (35N), *J. Geophys. Res.*, *110*, 2005.

Chu, Y.-H., P. S. Brahmanandam, C.-Y. Wang, C.-L. Su, and R.-M. Kuong, Coordinated sporadic E layer observations made with Chung-Li 30 MHz radar, ionosonde and FORMOSAT-3/COSMIC satellites, *Journal of Atmospheric and Solar-Terrestrial Physics*, *73*, 883–894, doi:10.1016/j.jastp.2010.10.004, 2011.

Cosgrove, R. B., and R. T. Tsunoda, Polarization electric fields sustained by closed-current dynamo structures in midlatitude sporadic e, *Geophysical Research Letters*, *28*(8), 1455–1458, doi:10.1029/2000GL012178, 2001.

Dickinson, R. E., Baroclinic instability of an unbounded zonal shear flow in a compressible atmosphere, *Journal of the Atmospheric Sciences*, *30*(8), 1520–1527, 1973.

Didebulidze, G. G., and L. N. Lomidze, Double atmospheric gravity wave frequency oscillations of sporadic E formed in a horizontal shear flow, *Physics Letters A*, *374*, 952–959, doi:10.1016/j.physleta.2009.12.026, 2010.

Drazin, P., and L. Howard, Hydrodynamic stability of parallel flow of inviscid fluid, *Advances in Applied Mechanics*, *9*, 1–85, 1966.

Drazin, P. G., *Introduction to Hydrodynamic Stability*, Cambridge University Press, 2002.

Drummond, J., B. Grime, C. Gardner, A. Liu, X. Chu, and T. Kane, Observations of persistent leonid meteor trails. advection of the "diamond ring", *J. Geophys. Res.*, *106 No.A10*, 21,517–21,524, 2001.

Dungey, J., Effect of a magnetic field on turbulence in an ionized gas, *J. Geophys. Res.*, *64, No.12*, 1959.

Eady, E. T., Long waves and cyclone waves, *Tellus*, *1*(3), 33–52, 1949.

Elford, W., A study of winds between 80 and 100 km in medium latitudes, *Planetary and Space Science*, *1*(2), 94 – 101, doi:http://dx.doi.org/10.1016/0032-0633(59)90003-0, 1959.

Englert, C., J. Harlander, C. Brown, J. Meriwether, J. Makela, M. Castelaz, J. Emmert, D. Drob, and K. Marr, Coincident thermospheric wind measurements using ground-based Doppler Asymmetric Spatial Heterodyne (DASH) and Fabry Perot Interferometer (FPI) instruments, *Journal of Atmospheric and Solar-Terrestrial Physics*, *86*, 92 – 98, 2012.

Eyken, A. P. v., P. J. S. Williams, S. C. Buchert, and M. Kunitake, First measurements of tidal modes in the lower thermosphere by the EISCAT Svalbard

radar, *Geophysical Research Letters*, *27*(7), 931–934, doi:10.1029/1999GL003687, 2000.

Farley, D., *Incoherent Scatter*, To be published, 2009.

Fjörtoft, R., Application of integral theorems in deriving criteria of stability of laminar flow and for the baroclinic circular vortex., *Geofys.Publ.*, *17*, 1–52, 1950.

Franke, S., C. X., and L. A. Z., Comparison of meteor radar and Na Doppler lidar measurements of winds in the mesopause region above Maui, Hawaii, *J. Geophys. Res.*, *110*(D09S02), doi:10.1029/2003JD004486, 2005.

Franke, S. J., and D. Thorsen, Mean winds and tides in the upper middle atmosphere at Urbana (40N, 88W) during 1991-1992, *Journal of Geophysical Research: Atmospheres*, *98*(D10), 18,607–18,615, doi:10.1029/93JD01840, 1993.

Friedman, J. S., and X. Chu, Nocturnal temperature structure in the mesopause region over the arecibo observatory (18.35ąn, 66.75ąw): Seasonal variations, *Journal of Geophysical Research: Atmospheres (1984Đ2012)*, *112*(D14), doi:10.1029/2006JD008220, 2007.

Fritts, D. C., and M. J. Alexander, Gravity wave dynamics and effects in the middle atmosphere, *Reviews of Geophysics*, *41*(1), doi:10.1029/2001RG000106, 1003, 2003.

Fritts, D. C., B. P. Williams, C. Y. She, J. D. Vance, M. Rapp, F.-J. Lübken, A. Mullemann, F. J. Schmidlin, and R. A. Goldberg, Observations of extreme temperature and wind gradients near the summer mesopause during the MaCWAVE/MIDAS rocket campaign, *Geophysical Research Letters*, *31*(24), doi:10.1029/2003GL019389, l24S06, 2004.

Fritts, D. C., et al., The deep propagating gravity wave experiment (deepwave): An airborne and ground-based exploration of gravity wave propagation and effects from their sources throughout the lower and middle atmosphere, *Bulletin of the American Meteorological Society*, 2015.

Fukao, S., M. Yamamoto, R. T. Tsunoda, H. Hayakawa, and T. Mukai, The SEEK (Sporadic-*E* Experiment over Kyushu) campaign, *Geophys. Res. Lett.*, *25*, 1761, 1998.

Gardner, C. S., Y. Zhao, and A. Z. Liu, Atmospheric stability and gravity wave dissipation in the mesopause region, *Journal of Atmospheric and Solar-Terrestrial Physics*, *64*(8–11), 923 – 929, {PSMOS} 2000 Workshop - Planetary Scale Mesopause Observing System, 2002.

Gill, A. E., *Atmosphere-ocean dynamics*, vol. 30, Academic press, 1982.

Green, J. S. A., A problem in baroclinic stability, *Quarterly Journal of the Royal Meteorological Society*, *86*(368), 237–251, doi:10.1002/qj.49708636813, 1960.

Haldoupis, C., *Aeronomy of the Earth's Atmosphere and Ionosphere*, chap. A Tutorial Review on Sporadic E Layers, pp. 381–394, Springer Netherlands, Dordrecht, 2011a.

Haldoupis, C., Midlatitude Sporadic E. A typical paradigm of atmosphere-ionosphere coupling, *Space Science Reviews*, *168*(1), 441–461, doi: 10.1007/s11214-011-9786-8, 2011b.

Haldoupis, C., and D. Pancheva, Terdiurnal tide like variability in sporadic E layers, *Journal of Geophysical Research: Space Physics*, *111*(A7), doi: 10.1029/2005JA011522, a07303, 2006.

Hansen, P., The l-curve and its use in the numerical treatment of inverse problems, in *Computational Inverse Problems in Electrocardiography*, *Advances in Computational Bioengineering*, vol. 5, edited by P.R. Johnston, pp. 119–142, WIT Press / Computational Mechanics, 2001.

Harding, B. J., J. J. Makela, and J. W. Meriwether, Estimation of mesoscale thermospheric wind structure using a network of interferometers, *Journal of Geophysical Research: Space Physics*, *120*(5), 3928–3940, doi:10.1002/2015JA021025, 2015JA021025, 2015.

Hecht, J. H., A. Z. Liu, R. L. Bishop, J. H. Clemmons, C. S. Gardner, M. F. Larsen, R. G. Roble, G. R. Swenson, and R. L. Walterscheid, An overview of observations of unstable layers during the turbulent oxygen mixing experiment (tomex), *Journal of Geophysical Research: Atmospheres*, *109*(D2), doi: 10.1029/2002JD003123, d02S01, 2004.

Hines, C., G. Adams, J. Brosnahan, F. Djuth, M. Sulzer, C. Tepley, and J. van Baelen, Multi-instrument observations of mesospheric motions over Arecibo - Comparisons and interpretations, *Journal of Atmospheric and Terrestrial Physics*, *55*, 241–287, 1993.

Hines, C. O., Internal gravity waves at ionospheric heights, *Can. J. Phys.*, *38*, 1441, 1960.

Holton, J., *An Introduction to Dynamic Meteorology* (4th ed.), Elsevier Inc., 2004.

Howard, L. N., Note on a paper of John W. Miles, *J. Fluid Mech.*, *10*, 509–512, 1961.

Hysell, D. L., M. F. Larsen, and Q. H. Zhou, Common volume coherent and

incoherent scatter radar observations of mid-latitude sporadic *E*-layers and QP echoes, *Ann. Geophys.*, *22*, 3277–3290, 2004.

Hysell, D. L., E. Nossa, M. F. Larsen, J. Munro, M. P. Sulzer, and S. A. González, Sporadic *E* layer observations over Arecibo using coherent and incoherent scatter radar: Assessing dynamic stability in the lower thermosphere, *J. Geophys. Res.*, *114*(A12), A12,303–, 2009.

Hysell, D. L., T. Yokoyama, E. Nossa, R. B. Hedden, M. F. Larsen, J. Munro, S. Smith, M. P. Sulzer, and S. A. González, *Radar and Optical Observations of Irregular Midlatitude Sporadic E Layers Beneath MSTIDs*, pp. 269–281, Springer Netherlands, Dordrecht, 2011.

Hysell, D. L., E. Nossa, M. F. Larsen, J. Munro, S. Smith, M. P. Sulzer, and S. A. González, Dynamic instability in the lower thermosphere inferred from irregular sporadic *E* layers, *Journal of Geophysical Research: Space Physics*, *117*(A8), doi:10.1029/2012JA017910, a08305, 2012.

Hysell, D. L., M. F. Larsen, and M. P. Sulzer, High time and height resolution neutral wind profile measurements across the mesosphere/lower thermosphere region using the Arecibo incoherent scatter radar, *Journal of Geophysical Research: Space Physics*, *119*(3), 2345–2358, doi:10.1002/2013JA019621, 2014.

Jackson, J. D., *Classical Electrodynamics*, John Wiley, 1975.

Kaladze, T., and L. Tsamalashvili, Solitary dipole vortices in the Earth's ionosphere, *Physics Letters A*, *232*(3), 269 – 274, 1997.

Kaladze, T., D. Wu, L. Tsamalashvili, and G. Jandieri, Localized magnetized Rossby structures under zonal shear flow in the ionospheric *E*-layer, *Physics Letters A*, *365*(1â A2), 140 – 143, 2007.

Kaladze, T. D., and W. Horton, Synoptic-scale nonlinear stationary magnetized Rossby waves in the ionospheric *E*-layer, *Plasma Physics Reports*, *32*(12), 996–1006, doi:10.1134/S1063780X06120038, 2006.

Kaladze, T. D., G. D. Aburjania, O. A. Kharshiladze, W. Horton, and Y.-H. Kim, Theory of magnetized Rossby waves in the ionospheric *E* layer, *Journal of Geophysical Research: Space Physics*, *109*(A5), doi:10.1029/2003JA010049, a05302, 2004.

Kaladze, T. D., L. V. Tsamakashvili, and L. Z. Kahlon, Rossby-Khantadze electromagnetic planetary vortical motions in the ionospheric *E*-layer, *Journal of Plasma Physics*, *77*, 813–828, doi:10.1017/S0022377811000237, 2011.

Kaladze, T. D., W. Horton, L. Z. Kahlon, O. Pokhotelov, and O. Onishchenko, Generation of zonal flow and magnetic field by coupled Rossby-Khantadze waves in the Earth's ionospheric *E*-layer, *Physica Scripta*, *88*(6), 065,501, 2013.

Kelley, M., *The Earth's Ionosphere: Plasma Physics and Electrodynamics*, Academic, 2009.

Killeen, T. L., Q. Wu, S. C. Solomon, D. A. Ortland, W. R. Skinner, R. J. Niciejewski, and D. A. Gell, Timed doppler interferometer: Overview and recent results, *Journal of Geophysical Research: Space Physics*, *111*(A10), doi:10.1029/2005JA011484, a10S01, 2006.

Kirkwood, S., and H. Nilsson, High-latitude sporadic-e and other thin layers – the role of magnetospheric electric fields, *Space Science Reviews*, *91*(3), 579–613, doi:10.1023/A:1005241931650, 2000.

Kudeki, E., P. K. Rastogi, and F. Sürücü, Systematic errors in radar wind es-

timation: Implications for comparative measurements, *Radio Science*, *28*(2), 169–179, doi:10.1029/92RS01931, 1993.

Kunze, E., A. J. Williams, and M. G. Briscoe, Observations of shear and vertical stability from a neutrally buoyant float, *Journal of Geophysical Research: Oceans*, *95*(C10), 18,127–18,142, doi:10.1029/JC095iC10p18127, 1990.

Larsen, M. F., A shear instability seeding mechanism for quasiperiodic radar echoes, *J. Geophys. Res.*, *105*(A11), 24,931–24,940, 2000a.

Larsen, M. F., A shear instability seeding mechanism for quasi-periodic radar echoes, *J. Geophys. Res.*, *105, 24, 931*, 2000b.

Larsen, M. F., Winds and shears in the mesosphere and lower thermosphere: Results from four decades of chemical release wind measurements, *J. Geophys. Res.*, *107*(A8), 1215–, 2002.

Larsen, M. F., and C. G. Fesen, Accuracy issues of the existing thermospheric wind models: can we rely on them in seeking solutions to wind-driven problems?, *Annales Geophysicae*, *27*(6), 2277–2284, doi:10.5194/angeo-27-2277-2009, 2009.

Larsen, M. F., and J. W. Meriwether, Vertical winds in the thermosphere, *Journal of Geophysical Research: Space Physics*, *117*(A9), n/a–n/a, doi:10.1029/2012JA017843, a09319, 2012.

Larsen, M. F., and R. L. Walterscheid, Modified geostrophy in the thermosphere, *J. Geophys. Res.*, *100*, 17,321, 1996.

Larsen, M. F., S. Fukao, M. Yamamoto, R. Tsunoda, K. Igarashi, and T. Ono, The SEEK chemical release experiment: Observed neutral wind profile in a region of sporadic-*E*, *Geophys. Res. Lett.*, *25*, 1789, 1998.

Larsen, M. F., A. Z. Liu, R. L. Bishop, and J. H. Hecht, Tomex: A comparison of lidar and sounding rocket chemical tracer wind measurements, *Geophysical Research Letters*, *30*(7), n/a–n/a, doi:10.1029/2002GL015678, 1375, 2003.

Larsen, M. F., A. Z. Liu, C. S. Gardner, M. C. Kelley, S. Collins, J. .Friedman, and J. H. Hecht, Observations of overturning in the upper mesosphere and lower thermosphere, *J. Geophys. Res.*, *109, D02S04*, 10.1029/2002JD003,067, 2004.

Larsen, M. F., M. Yamamoto, S. Fukao, R. T. Tsunoda, and A. Saito, Observations of neutral winds, wind shears, and wave structure during a sporadic-e/qp event, *Annales Geophysicae*, *23*(7), 2369–2375, doi:10.5194/angeo-23-2369-2005, 2005.

Larsen, M. F., D. L. Hysell, Q. H. Zhou, S. M. Smith, J. Friedman, and R. L. Bishop, Imaging coherent scatter radar, incoherent scatter radar, and optical observations of quasiperiodic structures associated with sporadic *E* layers, *J. Geophys. Res.*, *112*(A6), A06,321–, 2007.

Layzer, D., The turbulence criterion in stably stratified shear flow and the origin of sporadic e, in *Ionospheric Sporadic*, edited by E. K. Smith and S. Matsushita, International Series of Monographs on Electromagnetic Waves, pp. 258 – 275, Pergamon, doi:http://dx.doi.org/10.1016/B978-0-08-009744-2.50025-4, 1962.

Li, T., C.-Y. She, H.-L. Liu, J. Yue, T. Nakamura, D. A. Krueger, Q. Wu, X. Dou, and S. Wang, Observation of local tidal variability and instability, along with dissipation of diurnal tidal harmonics in the mesopause region over Fort Collins, Colorado (41N, 105W), *Journal of Geophysical Research: Atmospheres*, *114*(D6), n/a–n/a, doi:10.1029/2008JD011089, d06106, 2009.

Liu, A. Z., W. K. Hocking, S. J. Franke, and T. Thayaparan, Comparison of Na

lidar and meteor radar wind measurements at Starfire Optical Range, NM, USA, *J. Atmos. Terr. Phys.*, *64*(1), 31 – 40, doi:10.1016/S1364-6826(01)00095-5, 2002.

Liu, A. Z., R. G. Roble, J. H. Hecht, M. F. Larsen, and C. S. Gardner, Unstable layers in the mesopause region observed with Na lidar during the Turbulent Oxygen Mixing Experiment (TOMEX) campaign, *Journal of Geophysical Research: Atmospheres*, *109*(D2), doi:10.1029/2002JD003056, d02S02, 2004.

Liu, H.-L., On the large wind shear and fast meridional transport above the mesopause, *Geophysical Research Letters*, *34*(8), doi:10.1029/2006GL028789, l08815, 2007.

Lorenz, E. N., *The nature and theory of the general circulation of the atmosphere*, vol. 218, World Meteorological Organization Geneva, 1967.

Makela, J. J., J. W. Meriwether, Y. Huang, and P. J. Sherwood, Simulation and analysis of a multi-order imaging fabry–perot interferometer for the study of thermospheric winds and temperatures, *Appl. Opt.*, *50*(22), 4403–4416, doi:10.1364/AO.50.004403, 2011.

Manson, A. H., C. E. Meek, M. Massebeuf, J. L. Fellous, and W. G. Elford, Mean winds of the mesosphere and lower thermosphere (60-110 km) - A global distribution from radar systems (MF, meteor, VHF), *Advances in Space Research*, *5*, 135–144, doi:10.1016/0273-1177(85)90370-9, 1985.

Marshall, J., and F. Schott, Open-ocean convection: Observations, theory and models, *Rev. Geophys*, pp. 1–64, 1999.

Mathews, J., Sporadic *E* : current views and recent progress, *Journal of At-*

mospheric and Solar-Terrestrial Physics, *60*(4), 413 – 435, doi:10.1016/S1364-6826(97)00043-6, 1998.

Meriwether, J. W., and A. J. Gerrard, Mesosphere inversion layers and stratosphere temperature enhancements, *Reviews of Geophysics*, *42*(3), doi:10.1029/2003RG000133, rG3003, 2004.

Mikkelsen, I. S., and M. F. Larsen, An analytic solution for the response of the neutral atmosphere to the high-latitude convection pattern, *Journal of Geophysical Research: Space Physics*, *88*(A10), 8073–8080, doi:10.1029/JA088iA10p08073, 1983.

Mikkelsen, I. S., T. S. Jørgensen, M. C. Kelley, M. F. Larsen, and E. Pereira, Neutral winds and electric fields in the dusk auroral oval 2. theory and model, *Journal of Geophysical Research: Space Physics*, *86*(A3), 1525–1536, doi:10.1029/JA086iA03p01525, 1981a.

Mikkelsen, I. S., T. S. Jørgensen, M. C. Kelley, M. F. Larsen, E. Pereira, and J. Vickrey, Neutral winds and electric fields in the dusk auroral oval 1. measurements, *Journal of Geophysical Research: Space Physics*, *86*(A3), 1513–1524, doi:10.1029/JA086iA03p01513, 1981b.

Miles, On the stability of heterogeneous shear flows, *J. Fluid Mech.*, *10*, 496–508, 1961.

Miller, K. L., and L. G. Smith, Incoherent scatter radar observations of irregular structure in mid-latitude sporadic *E* layers, *J. Geophys. Res.*, *83*, 3761, 1978.

Mlynczak, M. G., F. Morgan, J.-H. Yee, P. Espy, D. Murtagh, B. Marshall, and F. Schmidlin, Simultaneous measurements of the $O_2(^1\Delta)$ and $O_2(^1\Sigma)$ airglows

and ozone in the daytime mesosphere, *Geophysical Research Letters*, *28*(6), 999–1002, doi:10.1029/2000GL012423, 2001.

Molemaker, M. J., J. C. Mcwilliams, and I. Yavneh, Baroclinic instability and loss of balance, *J. Phys. Oceanogr*, pp. 1505–1517, 2005.

Peixóto, J. P., and A. H. Oort, Physics of climate, *Rev. Mod. Phys.*, *56*, 365–429, doi:10.1103/RevModPhys.56.365, 1984.

Pfaff, R. F., et al., Comparison of observations of sporadic-*E* layers in the nighttime and daytime mid-latitude ionosphere, *NASA technical report*, 2012.

Pfrommer, T., P. Hickson, and C.-Y. She, A large-aperture sodium fluorescence lidar with very high resolution for mesopause dynamics and adaptive optics studies, *Geophysical Research Letters*, *36*(15), doi:10.1029/2009GL038802, l15831, 2009.

Rayleigh, L., On the stability, or instability, of certain fluid motions, *Proceedings of the London Mathematical Society*, *s1-11*(1), 57–72, doi:10.1112/plms/s1-11.1.57, 1879.

Richards, P. G., D. Bilitza, and D. Voglozin, Ion density calculator (idc): A new efficient model of ionospheric ion densities, *Radio Science*, *45*(5), doi:10.1029/2009RS004332, rS5007, 2010.

Riggin, D., W. E. Swartz, J. Providakes, and D. T. Farley, Radar studies of long-wavelength waves associated with mid-latitude sporadic *E* layers, *J. Geophys. Res.*, *91*, 8011, 1986.

Rosenbluth, M. N., and A. Simon, Necessary and sufficient condition for the stability of plane parallel inviscid flow, *Physics of Fluids*, *7*(4), 557–558, doi:10.1063/1.1711237, 1964.

Rydbeck, O. E. H., Chalmers ionospheric observatory, gÃűteborg, sweden, *Terrestrial Magnetism and Atmospheric Electricity*, *47*(3), 215–218, doi: 10.1029/TE047i003p00215, 1942.

Schunk, R., and A. Nagy, *Ionospheres: Physics, Plasma Physics, and Chemistry*, Cambridge Atmospheric and Space Science Series, Cambridge University Press, 2004.

She, C.-Y., D. A. Krueger, R. Akmaev, H. Schmidt, E. Talaat, and S. Yee, Long-term variability in mesopause region temperatures over Fort Collins, Colorado (41N, 105W) based on lidar observations from 1990 through 2007, *J. Appl. Spectr.*, *71*, 1558 – 1564, doi: http://dx.doi.org/10.1016/j.jastp.2009.05.007, long-Term Changes and Trends in the Atmosphere-Ionosphere System 5th IAGA/ICMA/CAWSES workshop "Long Term Changes and Trends in the Atmosphere, 2009.

She, C. Y., et al., Tidal perturbations and variability in the mesopause region over Fort Collins, CO (41N, 105W): Continuous multi-day temperature and wind lidar observations, *Geophysical Research Letters*, *31*(24), doi: 10.1029/2004GL021165, l24111, 2004.

Smith, L., and K. Miller, Sporadic-*E* layers and unstable wind shears, *J. Atmos. Terr. Phys.*, *42*(1), 45 – 50, doi:http://dx.doi.org/10.1016/0021-9169(80)90122-1, 1980.

Stevens, M. H., J. Gumbel, C. R. Englert, K. U. Grossmann, M. Rapp, and P. Hartogh, Polar mesospheric clouds formed from space shuttle exhaust, *Geophysical Research Letters*, *30*(10), doi:10.1029/2003GL017249, 1546, 2003.

Stober, G., and J. L. Chau, A multistatic and multifrequency novel approach for

specular meteor radars to improve wind measurements in the MLT region, *Radio Science*, *50*(5), 431–442, doi:10.1002/2014RS005591, 2014RS005591, 2015.

Sulzer, M. P., A phase modulation technique for a seven fold statistical improvement in incoherent scatter data-taking, *Radio Sci.*, *21*, 737, 1986a.

Sulzer, M. P., A radar technique for high range resolution incoherent scatter autocorrelation function measurements utilizing the full average power of klystron radars, *Radio Sci.*, *21*, 1033–1040, 1986b.

Tolstoy, I., Hydromagnetic gradient waves in the ionosphere, *Journal of Geophysical Research*, *72*(5), 1435–1442, doi:10.1029/JZ072i005p01435, 1967.

Tsunoda, R. T., and R. Cosgrove, Coupled electrodynamics in the night time midlatitude ionosphere, *Geophys. Res. Lett.*, *28*, 4171, 2001.

Tsunoda, R. T., S. Fukao, and M. Yamamoto, On the origin of quasi-periodic backscatter from sporadic *E*, *Radio Sci.*, *29*, 349, 1994.

Turner, J. S., *Buoyancy Effects in Fluids*, Cambridge University Press, cambridge Books Online, 1973.

Väisälä, V., Ęber die wirkung der windschwankungen auf die pilotbeobachtungen, *Helsingfors: Societas Scientiarum Fennica. Phys-Math*, *2*, 19–37, 1926.

Vincent, R. A., and D. Lesicar, Dynamics of the equatorial mesosphere: First results with a new generation partial reflection radar, *Geophysical Research Letters*, *18*(5), 825–828, doi:10.1029/91GL00768, 1991.

Whitehead, J. D., The formation of the sporadic-*E* layer in the temperate zones, *J. Atmos. Terr. Phys.*, *20*, 49–58, 1961.

Whitehead, J. D., The structure of sporadic *E* from a radio experiment, *Radio Sci.*, *7*, 355, 1972.

Whitehead, J. D., Recent work on mid-latitude and equatorial sporadic *E*, *J. Atmos. Terr. Phys.*, *51*, 401, 1989.

Woodman, R. F., M. Yamamoto, and S. Fukao, Gravity wave modulation of gradient drift instabilities in mid-latitude sporadic *E* irregularities, *Geophys. Res. Lett.*, *18*, 1197, 1991.

Yamamoto, M., S. Fukao, R. F. Woodman, T. Ogawa, T. Tsuda, and K. Kato, Mid-latitude *E* region field-aligned irregularities observed with the MU radar, *J. Geophys. Res.*, *96*, 15,943, 1991.

Yamamoto, M., S. Fukao, T. Ogawa, T. Tsuda, and S. Kato, A morphological study of mid-latitude *E*-region field-aligned irregularities observed with the MU radar, *J. Atmos. Terr. Phys.*, *54*, 769, 1992.

Yamamoto, M., S. Fukao, R. T. Tsunoda, R. Pfaff, and H. Hayakawa, SEEK-2 (Sporadic-E experiment over Kyushu 2) - project outline, and significance, *Annales Geophysicae*, *23*(7), 2295–2305, doi:10.5194/angeo-23-2295-2005, 2005.

Younger, P. T., D. Pancheva, H. R. Middleton, and N. J. Mitchell, The 8-hour tide in the arctic mesosphere and lower thermosphere, *Journal of Geophysical Research: Space Physics (1978-2012)*, *107*(A12), SIA 2–1–SIA 2–11, doi:10.1029/2001JA005086, 2002.

Yue, J., and H.-L. Liu, Fast meridional transport in the lower thermosphere by planetary-scale waves, *Journal of Atmospheric and Solar-Terrestrial Physics*, *72*(18), 1372 – 1378, doi:http://dx.doi.org/10.1016/j.jastp.2010.10.001, 2010.

Yue, J., C.-Y. She, and H.-L. Liu, Large wind shears and stabilities in the mesopause region observed by Na wind-temperature lidar at mid-latitude, *Journal of Geophysical Research: Space Physics*, *115*(A10), doi: 10.1029/2009JA014864, a10307, 2010.

Zhao, Y., A. Z. Liu, and C. S. Gardner, Measurements of atmospheric stability in the mesopause region at Starfire Optical Range, NM, *J. Atmos. Sol. Terr. Phys.*, *65*, 219, 2003.

Zhou, Q., and J. D. Mathews, Generation of sporadic sodium layers via turbulent heating of the atmosphere?, *Journal of Atmospheric and Terrestrial Physics*, *57*(11), 1309 – 1319, 1995.